

THE UNIVERSITY OF CHICAGO

AUTONOMOUS QUANTUM ERROR CORRECTION WITH SUPERCONDUCTING  
QUBITS

A DISSERTATION SUBMITTED TO  
THE FACULTY OF THE DIVISION OF THE PHYSICAL SCIENCES  
IN CANDIDACY FOR THE DEGREE OF  
DOCTOR OF PHILOSOPHY

DEPARTMENT OF PHYSICS

BY  
ZIQIAN LI

CHICAGO, ILLINOIS

DECEMBER 2024

Copyright © 2024 by Ziqian Li

All Rights Reserved

# TABLE OF CONTENTS

LIST OF FIGURES . . . . .	v
LIST OF TABLES . . . . .	xiv
ACKNOWLEDGMENTS . . . . .	xvi
ABSTRACT . . . . .	xviii
1 INTRODUCTION . . . . .	1
1.1 Quantum Error Correction . . . . .	1
1.2 Thesis Overview . . . . .	2
2 CIRCUIT QUANTUM ELECTRODYNAMICS . . . . .	4
2.1 Circuit Quantization . . . . .	4
2.2 Transmon Two-qubit Gate Implementation . . . . .	9
2.2.1 Cross-resonance gate . . . . .	10
2.2.2 Diabatic gate . . . . .	13
2.2.3 Parametric modulation gate . . . . .	16
2.2.4 Stray ZZ interactions . . . . .	18
2.3 Transmon state tomography . . . . .	20
3 THE STAR CODE THEORY . . . . .	24
3.1 The Very Small Logical Qubit . . . . .	24
3.2 Split into Virtual Raman Processes: The Star Code . . . . .	29
3.3 Star Code Simulation . . . . .	36
3.4 Coherence Limits from non-ideal Parameters . . . . .	42
3.5 Goals for Experimental Demonstration . . . . .	44
4 TOWARDS AUTONOMOUS QUANTUM ERROR CORRECTION . . . . .	45
4.1 Two inductively coupled transmons . . . . .	45
4.2 Two-Qutrit Quantum Algorithms on a Programmable Superconducting Processor . . . . .	56
4.2.1 Single-qutrit Gate operation . . . . .	57
4.2.2 Two-qutrit Gate operation . . . . .	60
4.2.3 Deutsch-Jozsa algorithm . . . . .	67
4.2.4 Bernstein-Vazirani algorithm . . . . .	71
4.2.5 Grover’s Search . . . . .	71
4.2.6 Error Analysis . . . . .	74
4.3 Programmable Autonomous stabilization . . . . .	76
4.3.1 Stabilization theory . . . . .	77
4.3.2 Stabilization Experiments . . . . .	83
4.3.3 Stabilization Robustness . . . . .	87

4.3.4	Other stabilization combinations . . . . .	89
4.3.5	Error Analysis . . . . .	97
5	AUTONOMOUS QUANTUM ERROR CORRECTION . . . . .	99
5.1	Device implementation and sideband calibration . . . . .	99
5.2	Error correction performance . . . . .	104
5.3	Chip design: Flux line optimization . . . . .	108
5.4	Full Star Code calibration process . . . . .	112
5.5	ZZ cancellation . . . . .	117
5.6	State transfer rate . . . . .	120
5.7	Two-qutrit tomography . . . . .	122
5.8	Error analysis . . . . .	125
6	OUTLOOK AND CONCLUSIONS . . . . .	132
7	WIRINGS AND FAB RECIPE . . . . .	133
7.1	Wiring Diagrams . . . . .	133
7.2	Fab Recipe . . . . .	134
	REFERENCES . . . . .	138

## LIST OF FIGURES

2.1	Circuit diagram for a SQUID coupling to an LC resonator. . . . .	5
2.2	Different two-qubit gate implementations. (a) Cross-resonance gate. (b) Diabatic gate. (c) Coupler mediated diabatic gate. (d) Parametric gate. . . . .	10
2.3	Circuit diagram for realizing the cross-resonance gate. A controlled qubit is charge-driven at the target qubit frequency to activate an effective ZX interaction.	11
2.4	Circuit diagram for the realizing diabatic gate. A flux tunable qubit is capacitively coupled to a fixed frequency qubit. Single photon swap happens at rate $g$ when both qubits have the same frequency. . . . .	14
2.5	Circuit diagram for realizing the high fidelity diabatic gate with ZZ cancellation. The coupler frequency $\omega_c$ is biased to a ZZ-free point for idling and biased to an “on” point for a fast two-qubit gate. . . . .	15
2.6	Circuit diagram for realizing the parametric gate. . . . .	16
2.7	ZZ compensated tomography scheme and its application on a two-qubit system. (a) Tomography steps flow chart. The central idea is to use the system Hamiltonian to update the ideal tomography counts and perform MLE accordingly. (b) Comparison of simulated fidelities for a two-qubit system with ZZ coupling. Dashed lines: Standard MLE tomography. Solid lines: ZZ compensated tomography scheme. Three representative states (see text for description) — a product (blue), an entangled (brown), and a mixed (magenta) are chosen to show the effectiveness of ZZ compensated tomography. . . . .	22
3.1	VSLQ energy diagram. For simplicity, the two QQ interactions $ gf\rangle \leftrightarrow  fg\rangle$ and $ gg\rangle \leftrightarrow  ff\rangle$ are assumed to be both $W$ . And the QR interactions are assumed to be both $\Omega$ . . . . .	26
3.2	VSLQ device. (a) Device optical false-colored picture. The red and green elements are the transmons and readout resonators. The inset shows a scanning electron micrograph of the coupler loop (purple) and the two Josephson junctions for the qubits forming the main loop (red). The magnetic fluxes threading the main and coupler loop are denoted by $\Phi_1$ and $\Phi_2$ , respectively. (b) Equivalent circuit diagram. . . . .	27
3.3	Star code protocol. (a) An example of hardware layout. Two transmons are individually coupled to two resonators dispersively. The dashed box between the two transmons represents any tunable coupling element that can provide sufficiently strong QQ red and blue sideband interactions. (b) Four QQ sideband mixing configurations in the logical static frame. All sidebands are applied with an equal rate $W$ and specific detuning choices ( $\pm\nu_{0/1}$ ) to construct the logical manifold. . . . .	30

3.4	Star Code energy diagram in the rotating frame. The green dashed box covers the logical states and error states involved in the AQEC protocol, and the grey dashed box includes the other stray eigenstates that have suppressed population transfer by the energy gap. Error states from single-photon loss are restored to the parent logical states through individual correction paths. The QR sidebands (rate $\Omega/2$ ), the resonators' photon decay (rate $\kappa$ ), and the transmon $T_1$ decay (rate $\gamma$ ) are shown in the blue, brown, and black arrows respectively. . . . .	34
3.5	Error correction cycle for $ L_0\rangle$ . The effective $ L_0\rangle$ refilling rate $\Gamma_R$ is shown in the purple arrow. A second photon loss can happen at rate $\gamma$ before the completion of the refilling cycle. Population transfer to the grey dashed box is marked with blue dashed arrows, and the population transfer is suppressed by the energy difference $O(\nu)$ . . . . .	37
3.6	Simulated logical states' lifetime and physical qubit lifetime. Parameter used in the simulation: $\{\alpha_1, \alpha_2, W, \nu_0, \nu_1, \Omega, \kappa\} = \{-160, -260, 10, 5.77, -5.77, 0.71, 0.5\}$ MHz, $T_1 = 60 \mu\text{s}$ . . . . .	39
3.7	Logical lifetime ( $T_L$ ) as a function of detunings and sideband rates. Simulations are performed up to $200 \mu\text{s}$ with $T_1 = 20 \mu\text{s}$ for both transmons. The logical $T_L$ are extracted by fitting the last $180 \mu\text{s}$ to an exponential decay profile. (a) 2D scan of QQ sideband detunings $\nu_0$ and $\nu_1$ . Other parameters used in the simulation: $\{\alpha_1, \alpha_2, W, \Omega, \kappa\} = \{-160, -260, 5, 1, 0.5\}$ MHz. Optimal performance is obtained around $\nu_0 = -\nu_1 = \pm W/\sqrt{3}$ . (b) 2D scan of QQ and QR sideband rates $W$ and $\Omega$ . Parameters are set to be $\nu_0 = -\nu_1 = W/\sqrt{3}$ , and $\Omega = \kappa$ for best AQEC performance. Simulations show significantly improved performance around $\Omega = W/10$ . . . . .	40
3.8	Logical lifetime improvement as a function of transmon $T_1$ (considered identical for both transmons). Quadratic lifetime improvement (roughly linear improvement in the lifetime ratio) under AQEC is clearly seen in the plot. Logical $T_L$ are extracted by fitting traces to the exponential decay curve $A \exp(-t/T_L) + C$ (with $A$ and $C$ being free parameters), and the improvement ratio is $T_L/T_1$ . Error bars (one standard deviation) for $T_L$ are smaller than the marker size. Each simulation is run up to $800 \mu\text{s}$ , and the short period is not included in the fitting. Other parameters used in the simulation are $\{\alpha_1, \alpha_2, W, \nu_0, \nu_1, \Omega, \kappa\} = \{-160, -260, 10, 5.77, -5.77, 0.71, 0.5\}$ MHz. The analytic expression (solid lines) matches the simulation result. The depolarization lifetime of $ L_1\rangle$ is almost the same as $ L_0\rangle$ in simulation. All simulated logical lifetimes here are above the break-even point. . . . .	41
3.9	Simulated logical states' lifetime with qubit-resonator dispersive coupling $\chi$ . Simulation parameters: $\{\alpha_1, \alpha_2, W, \nu_0, \nu_1, \Omega, \kappa\} = \{-160, -260, 10, 5.77, -5.77, 0.71, 0.5\}$ MHz, $T_1 = 60 \mu\text{s}$ . . . . .	43

4.1	The device. (a) False-colored optical image. Two transmons (red) are inductively connected through a SQUID loop (purple, inset shows zoomed-in image). An on-chip flux line is coupled to the SQUID to activate QQ sidebands through parametric RF flux modulation at the proper DC flux position. Each transmon is capacitively coupled to the readout resonator (blue). Single transmon pulses are sent through the resonator input lines. QR sidebands are applied through corresponding charge lines. (b) Circuit schematic diagram. . . . .	46
4.2	Circuit quantization results of $H_Q$ . Comparison of (a) ‘Algorithm chip’ and (b) ‘AQEC chip’ transmon frequencies and (c) ‘Algorithm chip’ and (d) ‘AQEC chip’ cross-Kerr couplings between simulation and experiment. $Q_1$ (red) and $Q_2$ ’s (blue) $ g\rangle \leftrightarrow  e\rangle$ and $ e\rangle \leftrightarrow  f\rangle$ frequencies from numerical calculation and experiment are plotted as a function of $\Phi_{\text{ext}}$ . Four inter-qutrit cross-Kerr coupling strengths, $J_{11}$ , $J_{21}$ , $J_{12}$ and $J_{22}$ are calculated, and experiment data are marked out on the Star code operating point (dashed line). . . . .	49
4.3	Experimentally realized QQ and QR sidebands. From top to bottom are separately (a) QQ red sideband $ ge\rangle \leftrightarrow  eg\rangle$ , (b) QQ blue sideband $ gg\rangle \leftrightarrow  ee\rangle$ , (c) QR blue sideband between QR1 and QR2 $ g0\rangle \leftrightarrow  e1\rangle$ , and (d) QR1 red sideband $ e0\rangle \leftrightarrow  g1\rangle$ . Readout on $Q_1$ (red) and $Q_2$ (blue) are scaled between 0 ( $ g\rangle$ ) and 1 ( $ e\rangle$ ). Data points are connected for visual guidance. . . . .	55
4.4	Process tomography for Hadamard gates. The top and bottom panels show real and imaginary components of the process matrix ( $\chi$ ) for (a) an ideal case, (b) $Q_1$ , and (c) $Q_2$ . . . . .	58
4.5	Chevron plots for the six two-qutrit red sidebands. All sidebands are parametrically activated by modulating the coupler at the corresponding transition frequencies. Pulses used for flux modulations have a rectangular shape with 5 ns long rising and falling Gaussian-shaped edges. The x-axis represents the length of the flat-top section. Both qutrits are simultaneously read out, and each data point is an average of 1000 experiments. * $Q_1$ ’s readout are not shown in the $ 21\rangle \leftrightarrow  30\rangle$ and $ 22\rangle \leftrightarrow  31\rangle$ cases, as the readout on $ 3\rangle$ is not optimized. . . . .	61
4.6	Chevron plots for the four two-qutrit blue sidebands. Sidebands are all parametrically activated through flux modulation of the coupler at relevant frequencies. Pulses used for flux modulations have a rectangular shape with 5 ns long rising and falling Gaussian-shaped edges, and the x-axis represents the length of the flat-top section. Each experimental data is an average of 1000 measurements. . . . .	62
4.7	Coherent oscillations for all two-qutrit sidebands. On-resonance features from the Chevron plots are selected and fitted to extract the sideband rates and $\pi$ rotation lengths (shown in Table. 4.5). Rectangular pulses with 5 ns long Gaussian edges are used for flux modulations, and the x-axis represents the length of the flat-top section. Each data point is an average of 1000 experiments. . . . .	63

4.8	CPhase gate construction. (a) Partitioned energy level diagram. Flipping the phase of a specific target state in the region (0) is performed through a $2\pi$ side-band rotation (shown in red arrow). Flipping the other target states requires a decomposition. The application of a $C_\theta(\pi,  mn\rangle)$ follows the path marked with brown arrows starting from $ mn\rangle$ . Here the numbers inside the yellow circle indicate the total number of single-qutrit $\pi$ pulses required. (b) An example of circuit decomposition for the $C_\theta(\pi,  00\rangle)$ gate. (c) Single-qutrit phase compensation calibration for a $C_\theta(\pi,  jk\rangle)$ gate. . . . .	65
4.9	Two-qutrit tomography of the state $\frac{1}{3}( 0\rangle +  1\rangle +  2\rangle)^{\otimes 2}$ after applying the CPhase gate $C_\theta\left(\frac{8\pi}{9},  22\rangle\right)$ . The top and bottom rows are experimental and ideal density matrices, with the real and imaginary parts shown in the left and right columns. . . . .	66
4.10	Deutsch-Jozsa and Bernstein-Vazirani algorithms. (a) Quantum circuit for the algorithms. In DJ algorithm, gates $W_1, W_2 \in \{I, X, X^2, Z, Z^2\}$ are applied to implement a constant or a balanced oracle. The final output state being in $ 00\rangle$ or non $ 00\rangle$ distinguishes the two cases. (b) Experimental results for DJ algorithm. The rows and columns represent gates applied to $Q_1$ and $Q_2$ respectively. The average SPs are 75.5(3)% and 98.5(1)% for the constant (hatched boxes) and balanced (plain boxes) oracles respectively beating the classical rate of 50%. (c) Experimental results for BV algorithm. Each row corresponds to a specific oracle with the mapping $\{I, Z, Z^2\} \rightarrow \{0, 1, 2\}$ . The diagonal terms show the SPs for all nine strings mapped to the basis states with an average of 78.3(3)%, which is much larger than the classical SP of 33.3%. . . . .	68
4.11	Heatmap of the confusion matrix. $3^2$ basis states are prepared and measured for 20,000 times. The numbers represent average assignment probabilities. . . . .	70
4.12	Grover's search algorithm for two-qutrits. (a) Quantum circuit. The oracles are implemented by CPhase gates $C_\theta(\pi,  jk\rangle)$ . The diffusion operator amplifies the detection probability of the marked state. (b) Experimental results. Detection probabilities (corrected for measurement error) after one (top panel) and two (bottom panel) rounds of amplitude amplification are obtained with 20,000 averages. All individual success rates are far beyond the corresponding classical SPs of 11.1% and 22.2%. . . . .	72
4.13	Master equation simulation of two-qutrit Grover's search with one and two stages of amplitude amplification using experimentally measured parameters. These results are in good agreement with the experimental outcomes shown in Fig. 4.12(b) in the main text. . . . .	75

- 4.14 **Programmable stabilization protocol.** **a** General stabilization scheme. Two qubits' eigenstates  $\{|A\rangle, |B\rangle, |C\rangle, |D\rangle\}$  are plotted in the energy level diagram. When the energy relation  $E_D + E_A = E_B + E_C$  is satisfied,  $|A\rangle$  is stabilized. Qubit-resonator interactions and resonator photon decay rate  $\kappa$  are shown in blue and orange arrows. Qubit decay rate  $\gamma$  is assumed slowest and not plotted. **b** Stabilization of entangled states  $|\Psi_\theta\rangle = \sin(\theta/2)|gg\rangle - \cos(\theta/2)|ee\rangle$  or  $|\Phi_\theta\rangle = \sin(\theta/2)|ge\rangle - \cos(\theta/2)|eg\rangle$ . **c** A special case of **b** that stabilizes the odd and even parity bell states  $|\Phi_-\rangle$  and  $|\Psi_-\rangle$ . Circulating arrows are color-coded to represent red (exchange-like) and blue (two-photon-pumping) sidebands respectively. The QQ and QR sideband rates are separate  $\Omega$  and  $W_j$ , and the QR sideband is detuned in frequency by  $\Omega/2$ . . . . . 78
- 4.15 **Experimental stabilization of different Bell states.** Experimental demonstration of  $|\Psi_-\rangle$  (**a, b**) and  $|\Phi_-\rangle$  (**c, d**) stabilization with the initial state  $|gg\rangle$ . Two-qubit state tomography is performed at each time point, and the reconstructed density matrix is used to calculate the target state fidelity. The density matrices reconstructed with 5000 single shot measurements at  $49\ \mu\text{s}$  are plotted. Lab frame simulation results are shown in dash lines, matching well in short and long time scales. Parameters used in simulation:  $\{\Omega, W_1, W_2, \Gamma_1, \Gamma_2\}/2\pi = \{2.0, 0.47, 0.47, 0.33, 0.43\}$  MHz for  $|\Psi_-\rangle$  and  $\{3.0, 0.36, 0.36, 0.33, 0.43\}$  MHz for  $|\Phi_-\rangle$ . Qubit coherence time is chosen as  $\{T_1^{q1}, T_1^{q2}, T_\phi^{q1}, T_\phi^{q2}\} = \{25, 12, 25, 25\}$   $\mu\text{s}$ . Error bars (one standard deviation) are smaller than the marker size [24]. . . . . 84
- 4.16 **Spectroscopy of universal Bell-state stabilization.**  $|\Psi_\theta\rangle$  (**a**) and  $|\Phi_\theta\rangle$  (**b**) are separately stabilized with a measured fidelity above 78% among different blending angle  $\theta$ . The fidelities are measured after  $40\ \mu\text{s}$  of stabilization. No external drives are applied for stabilizing  $|gg\rangle$ . For  $|\Phi_\theta\rangle$  case, the fidelity dropped to 0 near  $\theta = \pi$ . The dotted lines indicate simulated fidelities for the odd and even parity Bell state stabilization. All parameters used in the simulation are the same as in Fig. 4.15. Error bars (one standard deviation) are smaller than the marker size [24]. . . . . 85
- 4.17 **Dissipative switching of Bell state parity.** The initial state is  $|gg\rangle$ , and the switch status is set to even parity between  $[0\ \mu\text{s}, 20\ \mu\text{s}]$  and  $[40\ \mu\text{s}, 60\ \mu\text{s}]$ , and to odd parity between  $[20\ \mu\text{s}, 40\ \mu\text{s}]$  and  $[60\ \mu\text{s}, 85\ \mu\text{s}]$ . Each experimental point is measured with the two-qubit state tomography. Stabilization time is calculated by fitting the parity signature to exponential decay after each switching event. . . . . 86
- 4.18 Rotating frame simulation of even and odd parity bell states' stabilization fidelity: (a) Sweeping qubit dephasing time. The other simulation parameters are the same as the experiments. (b) Sweeping the ratio between resonator decay rate  $\kappa$  and QR sideband strength  $W$  without qubit dephasing. (c) 2D sweep of  $\kappa$  and QQ sideband strength  $\Omega$  without qubit dephasing, setting  $W = \kappa$ . Infidelities are shown on the contours. . . . . 87
- 4.19 Steady state stabilization fidelity under various stray ZZ interactions between qubits. For  $|\Psi_-\rangle$  ( $|\Phi_-\rangle$ ), we choose the QQ sideband detunings as  $\delta = -ZZ(0)$  for maximum stabilization fidelity. . . . . 89

4.20	Stabilizing a one-dimensional set of entangled states. Blue and red lines represent separately using the QQ blue and QQ red sideband in the rotating frame simulation. Parameter used in the simulation: $\{\Omega, W_1, W_2, \kappa_1, \kappa_2\}/2\pi = \{5.0, 0.5, 0.5, 0.3, 0.33\}$ MHz. Qubit coherence time are $\{T_1, T_\phi\} = \{30, 30\}\mu\text{s}$ . . . . .	91
4.21	Stabilizing a 2D set of entangled states. Steady states' fidelity (a) and purity (b) are simulated in the rotating frame and plotted. $\frac{A_1}{\Omega}$ and $\frac{\delta}{\Omega}$ are separately two free variables that are swept to stabilize different states. Parameter used in the simulation: $\{\Omega, W_1, W_2, \kappa_1, \kappa_2\}/2\pi = \{5.0, 0.5, 0.5, 0.3, 0.33\}$ MHz. Qubit coherence time are $\{T_1, T_\phi\} = \{30, 30\}\mu\text{s}$ . . . . .	93
4.22	(a) Use both QR red sidebands to stabilize $ \Psi_\theta\rangle$ . (b) Use opposite QR blue sideband detunings to stabilize $ \Psi_{\theta-\pi}\rangle$ . The QQ sideband rates and detunings are separate $\Omega$ and $\delta$ , and the QR sideband is detuned in frequency by $\frac{\Delta+\delta}{2}$ , $\frac{\Delta-\delta}{2}$ in (a) and $-\frac{\Delta+\delta}{2}$ , $-\frac{\Delta-\delta}{2}$ in (b). Here $\Delta = \sqrt{\Omega^2 + \delta^2}$ . . . . .	95
5.1	<b>Illustration of the autonomous error-correction scheme.</b> The protocol requires simultaneous application of two QQ blue sidebands ( $ ee\rangle \leftrightarrow  gg\rangle$ and $ ee\rangle \leftrightarrow  ff\rangle$ ), two QQ red sidebands ( $ ee\rangle \leftrightarrow  fg\rangle$ and $ ee\rangle \leftrightarrow  gf\rangle$ ), and two QR error correcting sidebands ( $ e0\rangle \leftrightarrow  f1\rangle$ ). All six drives are always-on. <b>a</b> Star code logical word formation. All QQ sidebands have nominally equal rates $W$ . The two drives within a pair have opposite detunings from the on-resonance values. This opens up the energy gaps of $O(W)$ between logical states and other states $\{ S_\pm\rangle,  T\rangle\}$ (see Sec. 3.2 for full expression). With only QQ sidebands on, this forms the ‘‘QQ echoed’’ qubit sharing the same logical states as the star code. <b>b</b> The AQEC cycle for $ L_0\rangle$ (left) and $ L_1\rangle$ (right) when a single-photon-loss event occurs. Logical state $ L_000\rangle$ ( $ L_100\rangle$ ) loses a photon from transmon $Q_1$ at a rate $2\gamma_1$ and becomes the error state $ eg00\rangle$ ( $ ef00\rangle$ ). QR error correcting sidebands (applied on-resonance) bring the state at rate $\Omega_1$ to $ L_010\rangle$ ( $ L_110\rangle$ ) with one photon populating $R_1$ . $R_1$ 's photon decays quickly (at a rate $\kappa_1$ ) and recovers the original logical state. AQEC cycle for $Q_2$ 's photon loss event is similar. . . .	100
5.2	The device. (a) False-colored optical image. Two transmons (red) are inductively connected through a SQUID loop (purple, inset shows zoomed-in image). An on-chip flux line is coupled to the SQUID for activating QQ sidebands through parametric RF flux modulation at the proper DC flux position. Each transmon is capacitively coupled to the readout resonator (blue). Single transmon pulses are sent through the resonator input lines. QR sidebands are applied through corresponding charge lines. (b) Circuit schematic diagram. . . . .	101

5.3	<b>Different parametric oscillations.</b> Photon numbers in individual transmons are measured as a function of time. <b>a</b> Error correcting QR sidebands $ e0\rangle \leftrightarrow  f1\rangle$ applied separately at rates $\Omega_1 = 0.49$ MHz and $\Omega_2 = 0.59$ MHz to the transmon-resonator pairs with $ e\rangle$ as initial states. Effective transitions <b>b</b> $ gf\rangle \leftrightarrow  fg\rangle$ and <b>c</b> $ gg\rangle \leftrightarrow  ff\rangle$ are measured when all QQ and QR sidebands are simultaneously turned on. Extracted sideband rates and detunings from simulation are $W_r = 1.45$ MHz, $W_b = 1.25$ MHz, $\nu_r = 0.8$ MHz, $\nu_b = -0.9$ MHz, $\Omega_1 = \Omega_2 = 0.39$ MHz. Other parameters are based on experimentally measured data shown in Table. 4.3. Oscillation distortions qualitatively match the lab frame simulations (dashed lines). Measurement errors are smaller than the marker size. . . . .	103
5.4	<b>Error population under different conditions.</b> Black, blue, and green points represent tomographic measurement results under free decay, 4 QQ echo, and full AQEC. The y-axes represent the combined population of error states for initial states <b>a</b> $ L_0\rangle$ , <b>b</b> $ L_1\rangle$ , and <b>c</b> $ L_x\rangle$ . Population accumulates at the error states in the free decay case, enhanced in the 4 QQ echo case, and corrected with AQEC drive on. The experimental data is explained with master equation simulations shown in solid lines. Error bars (one standard deviation) are smaller than the marker size [24]. Detailed fitting parameters used for the solid lines are shown in Sec. 5.8. . . . .	105
5.5	<b>Coherence improvement.</b> Black, blue, and green circles are experimentally measured state fidelities at a given time. The fidelities are extracted from the tomographic reconstruction of states with 5000 repeated measurements. Error bars (one standard deviation) are smaller than the marker size [24]. The improvement with AQEC turned on is explained by the master equation simulation. <b>a</b> $ L_0\rangle$ and <b>b</b> $ L_1\rangle$ traces are fitted to the exponential decay curve $A \exp(-t/\tau) + C$ , and <b>c</b> $ L_x\rangle$ traces are fitted to $A \exp(-t/\tau)$ . The offset $C$ is necessary since fidelity will achieve steady-state values. The error (one standard deviation) for $\tau$ are obtained from the fitting. The large uncertainty comes from treating $C$ as a free variable in the fitting. The fast transition period (first $1.5 \mu\text{s} \sim \Omega_j^{-1}$ in the AQEC case is not included in the fitting* for a better representation of logical coherence. *First $10.5 \mu\text{s}$ data are used in $ L_1\rangle$ 's free decay case for better fitting. . . . .	107
5.6	Chevron plots for fast QQ sidebands. The state of both transmons are simultaneously read out and shown as photon numbers. Top two figures show 9 MHz $ gg\rangle \leftrightarrow  ee\rangle$ , and bottom two demonstrate 21 MHz $ ee\rangle \leftrightarrow  gf\rangle$ oscillations. . . .	109
5.7	Readout saturation feature for fast (rate 9 MHz) QQ blue sideband $ gg\rangle \leftrightarrow  ee\rangle$ in the long time scale. Top and bottom panel show readout signals from the first and second resonators. . . . .	110
5.8	Distribution of electrical field's amplitude (in log scale) when RF flux drive is modulated at (a) 700 MHz and (b) 7 GHz obtained from HFSS simulation. . . .	111
5.9	SQUID design. (a) Old design without optimization. (b) Current design by maximizing the mutual inductance between the flux line and SQUID. The Ta and Al areas are colored as grey and blue separately, and the bare sapphire is colored white. . . . .	112

5.10	The stepped impedance Purcell filter (SIPF). (a) Optical image of our SIPF chip made using Ta on sapphire. (b) Calculated SIPF insertion loss. Transmon transitions, QQ red and blue sideband frequencies are marked in the plot. . . . .	113
5.11	Gate circuits for the Star code calibration. (a) Pulse sequence for calibration of $ZZ_{ff1}$ . Ramsey-like protocol is used for the partner transmon being in $ g\rangle$ or $ f\rangle$ . The other $ZZ$ s are calibrated similarly. (b) QQ blue and (c) QQ red sideband frequency calibration sequence. QQ sideband pair frequencies are iteratively swept and updated based on the time-domain pattern. (d) $ L_1\rangle$ preparation phase calibration sequence. The phase point that has minimum $ e\rangle$ population in the sweep is chosen as the calibrated $\phi_{L1}$ . The preparation phase for $ L_0\rangle$ is calibrated similarly. (e) $ L_x\rangle$ preparation phase calibration protocol. All $\sqrt{X}$ operators represent $\pi/2$ rotations. . . . .	114
5.12	Simultaneous QQ sideband calibration. All six tones used in the Star code are simultaneously turned on during the frequency-time sweep. The red (top two panels) and blue (bottom two panels) QQ sideband pair frequencies are swept individually for calibration in the presence of the other pair. Red dash lines in the plots represent the pairs' center frequency choices. (a) and (b) are $Q_1$ and $Q_2$ 's average photon number when sweeping the red pair with the initial state $ fg\rangle$ . (c) and (d) are $Q_1$ and $Q_2$ 's average photon number when sweeping the blue pair with the initial state $ gg\rangle$ . . . . .	115
5.13	Preparation phase calibration of $ L_0\rangle$ (left) and $ L_1\rangle$ (right) in the error correction experiment. The population of $ e\rangle$ on $Q_1$ are measured after turning on all sidebands for up to $8\mu\text{s}$ , and the red dash line marks the calibrated phase position. We choose $Q_1$ due to higher readout fidelity. . . . .	116
5.14	Phase calibration for $ L_x\rangle$ preparation. Population of $ g\rangle$ (top) and $ f\rangle$ (bottom) on $Q_1$ (left) and $Q_2$ (right) are measured after $8\mu\text{s}$ , and the red star marks the calibrated phase position. . . . .	116
5.15	$ZZ$ cancellation. Total $ZZ_{ff1}$ (a) and $ZZ_{ff2}$ (b) (in MHz) are shown in the contour while sweeping amplitudes of two extra detuned external drives ( $ ef\rangle \leftrightarrow  gh\rangle$ and $ fe\rangle \leftrightarrow  hg\rangle$ ). Individual $ZZ$ cancellation contour line (with value 0) is marked. One of the four simultaneous cancellation points is highlighted in red circle. . . . .	119
5.16	Single shot confusion matrix. Two-qutrit basis states are prepared and measured 5000 times. . . . .	123
5.17	Evolution of the logical states under different conditions. Panels from top to bottom correspond to the logical state $ L_0\rangle$ , $ L_1\rangle$ and $ L_x\rangle$ . The real part of the density matrices are plotted as the imaginary components are small after phase rotation. The left column shows the initial states. Improvements in the coherence can be seen for the echo case when compared to free decay. With the full Star code protocol, further improvements are observed. . . . .	124

5.18	Theoretical logical lifetime in the rotating frame. The logical lifetime increases as a function of physical $T_1$ . A larger QQ sideband rate also provides higher logical qubit coherence. Parameter used for simulation are $\{W = 10, 5 \text{ MHz}, \Omega_j = 1.0 \text{ MHz}, \nu_r = -\nu_b = \frac{W}{2}\}$ , $\{W = 1.5 \text{ MHz}, \Omega_j = 0.4 \text{ MHz}, \nu_r = -\nu_b = 0.85 \text{ MHz}\}$ and $\kappa = 0.5 \text{ MHz}$ . . . . .	125
5.19	Simulation of the Star code performance in the static frame with the experimental data using fidelity metric. Error bars (one standard deviation) are smaller than the marker size. . . . .	128
7.1	Detailed cryogenic and room temperature measurement setup. . . . .	134

## LIST OF TABLES

4.1	Capacitances and Josephson energies used in the quantization. Capacitances are extracted through finite-element simulations in ANSYS Q3D, and Josephson energies are calculated from the room-temperature resistances of nominally identical test junctions on the same chip. . . . .	47
4.2	Device coherence parameters at different DC flux points. $Q_2$ has lower coherence at the zero flux point because of the presence of a two-level system (TLS). . . .	50
4.3	Device frequencies in the absence of external drives. $J_{jk}$ are inferred from the 7 $ZZ$ values measured in the experiment. . . . .	51
4.4	Total gate lengths for different single-qutrit operations. The $Z$ gates are implemented virtually. . . . .	56
4.5	Sideband rates and gate lengths for various interactions achieved with the device. The $\pi$ -pulse lengths include both the flat-top part and 5 ns rising and falling Gaussian tail of the pulse. The distortion observed for the $ 01\rangle \leftrightarrow  12\rangle$ Chevron is most likely due to the stray charge coupling of the flux line to the SQUID loop (see text for details). . . . .	64
4.6	Equivalent classical functions (ternary valued) for the 16 balanced functions implemented in the Deutsch-Jozsa algorithm. . . . .	69
4.7	Error budget for the two-qutrit Grover's search algorithm. Drops in SSOs after one and two rounds of amplitude amplification are shown due to different error channels. . . . .	74
4.8	<b>Infidelity channels for odd and even parity Bell states stabilization.</b> * The transmon excitation rate is approximately 0.9 ms, as inferred from the residual infidelities observed in the experiments. <sup>†</sup> Frequency mismatch are assumed to be at most 20kHz. . . . .	98
5.1	Calculated refilling process rate in our experiment. Logical refilling rate $\{\Gamma_{R1}, \Gamma_{R2}\}$ dominants over other logical error rate. . . . .	122
5.2	Parameters used in the master equation simulation. $\{W_{r/b}, \Omega_j, \nu_{r/b}\}$ are extracted through Fig. 5.12 in simulation; $ZZ_{ff1}$ and $ZZ_{ff2}$ are experimentally measured through $ e0\rangle \leftrightarrow  f1\rangle$ on-resonance frequency difference when all sidebands on. All coherence numbers $\{T_1, T_\phi\}$ , $n_{res}$ , and $\chi_j$ are free parameters chosen in the simulation to match the experimental data. The other parameters listed are all obtained from measurements. Irrelevant parameters in each case are not shown in the table and are not included in the simulation. <sup>†</sup> Dephasing in the 4 QQ echo and AQEC cases are higher because of the QQ sideband spin-echo improvement. * $Q_2$ 's $T_1^{ge}$ is lower than $Q_1$ 's because of the TLSs around the transition frequency. Effects to the codewords performance are minimal as the population on $ e\rangle$ is corrected. . . . .	130

5.3 Various decoherence channels for the logical qubit. Ideal implementation represents logical states' lifetime with QR coupling and only  $T_1$  error. Each limit is extracted using the simulation through lifetime difference after adding relevant error channels. The average photon number in the resonator ( $n_{\text{res}}$ ) increases during external drives and dephases transmons through photon shot noise. Other dephasing noise include  $1/f$  noise, white noise, correlated dephasing noise, and any other noise source. The total effect is represented with  $T_\phi^j$  in the simulation.  $ZZ$  between transmons introduces a large mismatch in QR frequency for  $|L_1\rangle$  and  $|L_x\rangle$ , and the effect is combined with  $ZZ$  dephasing for  $|L_x\rangle$  case. The drifts in sideband amplitudes frequencies are less than 5% and 20 kHz, and those limits are in the order of ms. \* Ideal implementation includes QR couplings  $\chi_j$  but no QQ  $ZZ$  couplings. †  $n_{\text{res}}$  and  $T_\phi^j$  are determined through simulation-experiment matching. ‡  $|L_y\rangle$ 's lifetime is estimated through simulation, based on  $|L_x\rangle$ 's experimental error channels. . . . . 131

## ACKNOWLEDGMENTS

First, I would like to thank my advisor, David Schuster, for his constant mentorship and fostering a collaborative lab environment. Whenever I encounter technical or physics—related challenges, Dave is always there to provide insightful, creative, and thorough suggestions. His open-mindedness and enthusiasm have inspired me with countless exciting ideas to explore, making my experience at the Schuster Lab truly enjoyable.

I want to thank Tanay Roy for patiently guiding me through everything when I was new to the lab—covering fabrication, measurements, packaging, simulations, and fridge maintenance. I am also grateful to Fang Zhao for her outstanding fabrication support for the Multimode project during the lab’s transition period and for her kind invitations to hang out on weekends. Many thanks to Andrei Vrajitoarea, Andrew Oriani, Riju Banerjee, Srivatsan Chakram, and Yao Lu for collaborating to discuss and resolve experimental challenges in the Multimode projects. Thanks to Gabrielle Roberts, Chunyang Ding, and Connie Miao for organizing lab events and fostering a strong group bond. I also appreciate Wendy Wan and Yueheng Shi working alongside me to develop the fabrication recipe at Stanford after the lab move. Special thanks to Eesh Gupta for joining the Multimode team and finally working together to tune up the sample. I would also like to acknowledge Shannon Harvey and Sebastien Leger for their tremendous help setting up and maintaining the fridges at SLAC. Finally, I want to extend my gratitude to all the Schuster Lab members not mentioned above. I am truly grateful to be part of this lab.

I would also like to acknowledge Eliot Kapit and his student, David Rodríguez Pérez, for their tremendous theoretical support. This thesis would not have been possible without Eliot’s innovative theoretical contributions, which greatly simplified the experimental requirements. I am also grateful to Fred Chong and his student, Maximilian Seifer, for the countless discussions that ultimately led to the successful experimental realization.

Finally, I would like to express my deepest gratitude to my family. To my mom and dad,

thank you for your unwavering support, even when I have been away for so long.

And to the most important person, my best friend and partner, Luxin Zhang—your encouragement and support have made this journey possible. Whenever I faced challenges or felt overwhelmed, your belief in me was a constant source of strength. You’ve supported me through the most challenging and rewarding moments, and I am deeply grateful for your love and unwavering presence. Beyond my research and work, you have made my life whole.

## ABSTRACT

Large-scale quantum computers will inevitably need quantum error correction to protect information against decoherence. Traditional error correction typically requires many qubits, along with high-efficiency error syndrome measurement and real-time feedback. Autonomous quantum error correction instead uses steady-state bath engineering to perform the correction in a hardware-efficient manner. In this thesis, we develop a new autonomous quantum error correction scheme, the Star Code, that actively corrects single-photon loss and passively suppresses low-frequency dephasing, and we demonstrate an important experimental step towards its full implementation with transmons. Compared to uncorrected encoding, improvements are experimentally witnessed for the logical zero, one, and superposition states. Our results show the potential of implementing hardware-efficient autonomous quantum error correction to enhance the reliability of a transmon-based quantum information processor.

# CHAPTER 1

## INTRODUCTION

Building a useful quantum computer has been one of the most exciting and fruitful challenges since the first proposal as an analog Hamiltonian simulator in the 1980s [25]. Shortly afterward, digital quantum computers are proposed with various quantum algorithms compiled into sequences of quantum gates implemented on qubits. Many successful qubit platforms are realized. Superconducting qubits are promising candidates for future scalable quantum computers: Straightforward fabrication, fast and high fidelity gate and readout, and scalable connection. Motivated by those advantages, this thesis focuses on experiments using superconducting qubits.

### 1.1 Quantum Error Correction

Quantum error correction (QEC) is essential for performing long computations involving many qubits, such as those required for Shor's algorithm [82] or quantum chemistry algorithms [4]. A fault-tolerant universal quantum computer requires both arbitrarily low infidelities and universal control. QEC is a key approach to achieving fault tolerance. The demonstration of QEC's existence represents a major breakthrough in the development of large-scale quantum computers [81]. Single-qubit error can be characterized by two types of errors:  $X$  (bit-flip) and  $Z$  (phase-flip). Remarkably, error correction codes, such as Shor's code—the first of its kind—can correct these errors, even in the presence of quantum no-go theorems like the no-cloning theorem. The threshold theorem [2] later established that arbitrarily low logical error rates are possible with QEC, provided the physical error rate is below a certain threshold.

Universal quantum computing requires only single- and two-qubit gates. A logical gate that does not propagate errors is compatible with QEC and is referred to as "error-transparent."

However, realizing a universal set of error-transparent gates is very challenging: According to the Eastin-Knill no-go theorem [21], error-transparent universality cannot be achieved using only simple transversal operations. Fortunately, magic state distillation [44] provides a fault-tolerant method for implementing two-logical-qubit gates on another famous QEC code, the surface code [43]. With the theoretical foundation for all key components of fault-tolerant quantum computers established, the challenge now lies with experimental realization.

Errors accumulating in a quantum system can be thought of as entropy or heat entering the system. Experimentally, two main approaches to QEC are measurement-based feedback error correction and reservoir-engineered autonomous error correction. Feedback-based QEC can be viewed as creating a "Maxwell Demon" in the lab to keep the system cool. These methods typically require many qubits and complex control hardware and have been demonstrated to approach the fault-tolerance threshold [46, 1, 10, 22, 77, 23, 18, 42, 87, 78].

On the other hand, laser cooling effectively integrates measurement and feedback into the internal level structure through carefully chosen laser drives. This concept has inspired autonomous quantum error correction (AQEC), where, instead of using measurements and gates, the system is "cooled" through an appropriate set of drives and couplings to engineered thermal reservoirs [86]. Similar to laser cooling, AQEC can greatly simplify the required quantum and classical hardware and control systems. Both autonomous and feedback-based QEC are more challenging than simple cooling because they must ensure that the cooling process preserves the logical manifold of the system.

## 1.2 Thesis Overview

In the remainder of this thesis, we will explore the journey of realizing Autonomous Quantum Error Correction (AQEC) using transmons. Chapter 2 introduces the fundamental procedure for designing and experimentally characterizing a quantum processor based on transmons. Chapter 3 proposes a new AQEC codeword, the Star Code, with its performance predicted

through analytical calculations and simulations. Chapter 4 discusses our inductively coupled two-transmon processor. We characterize the device parameters and implement two experiments toward AQEC: executing several qutrit algorithms that demonstrate universal control of two qutrit subspaces with decent fidelity and programmable stabilization, showing robust experimental control of engineered dissipation. Chapter 5 details our experimental realization of the Star Code, the central goal of this thesis. We describe the system calibration procedure and measure the logical encoding lifetimes with AQEC.

## CHAPTER 2

### CIRCUIT QUANTUM ELECTRODYNAMICS

This chapter will begin by discussing circuit QED [32, 79, 8, 9], which describes the system Hamiltonian parameters. Next, we will discuss some transmon couplers necessary for realizing the multi-photon process in our experiments and, more importantly, for universal quantum computing. Finally, we will present our experimental characterization steps, including a compensated tomography method that reconstructs the density matrix of a transmon system with ZZ couplings.

#### 2.1 Circuit Quantization

Fig. 2.1 shows a typical superconducting circuit that consists of three basic elements: capacitor, inductor, and the Josephson junction. The red part is the superconducting LC resonator, and the resonator's Lagrangian is:

$$L_{res} = \frac{1}{2}(C_r \dot{\Phi}_r^2 - \frac{\Phi_r^2}{L_r}) \quad (2.1)$$

Here  $\Phi_r$  is the node flux for the resonator. Applying the Legendre transformation, the Hamiltonian is:

$$H_{res} = \frac{1}{2}\left(\frac{Q_r^2}{C_r} + \frac{\Phi_r^2}{L_r}\right) \quad (2.2)$$

$$Q_r = \frac{\partial L_{res}}{\partial \dot{\Phi}_r} \quad (2.3)$$

$$[\Phi_r, Q_r] = i\hbar \quad (2.4)$$

Through second quantization, we get the resonator Hamiltonian (setting  $\hbar = 1$ ):

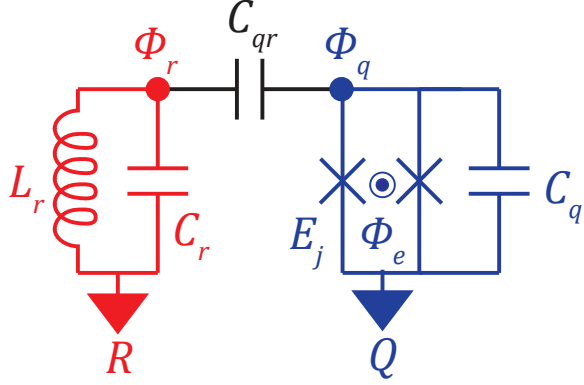


Figure 2.1: Circuit diagram for a SQUID coupling to an LC resonator.

$$H_{res} = \omega_r a_r^\dagger a_r \quad (2.5)$$

$$\omega_r = \sqrt{\frac{1}{L_r C_r}} \quad (2.6)$$

$$a_r = \frac{1}{\sqrt{2Z}} \Phi_r + i\sqrt{\frac{Z}{2}} Q_r \quad (2.7)$$

$$Z = \sqrt{\frac{L_r}{C_r}} \quad (2.8)$$

To introduce nonlinearity in the system, the resonator is capacitively coupled to the blue part, a flux-tunable transmon qubit made of a superconducting quantum interference device [34] (SQUID) shunted by a capacitor. The SQUID consists of two junctions forming a loop threaded by external flux  $\Phi_e$ . The Josephson junction is a dissipationless nonlinear element made of two superconducting islands gapped by a tunnel barrier [36]. Defining the phase difference between two superconducting islands as  $\theta$ , the  $I - V$  response of a single junction can be described as [3]:

$$I(t) = I_0 \sin(\theta(t)) \quad (2.9)$$

$$V(t) = \frac{\Phi_0}{2\pi} \frac{\partial \theta(t)}{\partial t} \quad (2.10)$$

The inductive energy across a single junction is:

$$\int I(t)V(t)dt = \frac{I_0\Phi_0}{2\pi} \int \sin(\theta(t)) \frac{\partial \theta(t)}{\partial t} dt = -E_J \cos \theta(t) \quad (2.11)$$

Here,  $E_J = \frac{I_0\Phi_0}{2\pi}$  is the Josephson energy.

Back to Fig. 2.1, we assume both junctions have the same  $E_J$  and the superconducting phase across each barrier are  $\theta_1$  and  $\theta_2$ . The external flux  $\Phi_e$  threaded the loop creates a difference between  $\theta_1$  and  $\theta_2$ :

$$\theta_2 - \theta_1 = \frac{2\pi\Phi_e}{\Phi_0} + 2\pi n, \quad n \in \mathbb{N} \quad (2.12)$$

Relabeling the variables with node flux  $\Phi_q$ , the Josephson energy for the SQUID (blue part) is [45]:

$$-E_J \left( \cos\left(\frac{2\pi\Phi_q}{\Phi_0} - \frac{\pi\Phi_e}{\Phi_0}\right) + \cos\left(\frac{2\pi\Phi_q}{\Phi_0} + \frac{\pi\Phi_e}{\Phi_0}\right) \right) = -2E_J \cos\left(\frac{\pi\Phi_e}{\Phi_0}\right) \cos\frac{2\pi\Phi_q}{\Phi_0} \quad (2.13)$$

The SQUID's charging energy is the same as the resonator cases, and the full SQUID Hamiltonian is:

$$H_{\text{SQUID}} = \frac{Q_q^2}{2C_q} - 2E_J \cos\left(\frac{\pi\Phi_e}{\Phi_0}\right) \cos\frac{2\pi\Phi_q}{\Phi_0} \quad (2.14)$$

$$[\Phi_q, Q_q] = i\hbar \quad (2.15)$$

In Fig. 2.1, the SQUID is capacitively coupled to the resonator, and the system's La-

grangian is:

$$L_0 = \frac{1}{2}(C_r \dot{\Phi}_r^2 + C_q \dot{\Phi}_q^2 + C_{qr}(\dot{\Phi}_r - \dot{\Phi}_q)^2) - \frac{\Phi_r^2}{2L_r} + 2E_J \cos\left(\frac{\pi\Phi_e}{\Phi_0}\right) \cos\frac{2\pi\Phi_q}{\Phi_0} \quad (2.16)$$

Performing the Legendre transformation:

$$Q_r = \frac{\partial L_0}{\partial \dot{\Phi}_r} \quad (2.17)$$

$$Q_q = \frac{\partial L_0}{\partial \dot{\Phi}_q} \quad (2.18)$$

$$\begin{aligned} H_0 &= \dot{\Phi}_r Q_r + \dot{\Phi}_q Q_q - L_0 \\ &= \frac{\Phi_r^2}{2L_r} - 2E_J \cos\left(\frac{\pi\Phi_e}{\Phi_0}\right) \cos\frac{2\pi\Phi_q}{\Phi_0} \\ &\quad + \frac{1}{2} \frac{(C_q + C_{qr})Q_r^2 + (C_r + C_{qr})Q_q^2 + C_{qr}Q_r Q_q}{(C_r + C_{qr})(C_q + C_{qr}) - C_{qr}^2} \end{aligned} \quad (2.19)$$

At this point, we can use the dimensionless number operator  $\hat{n} = -\frac{Q}{2e}$  ( $e$  is the elementary charge) and phase operator  $\hat{\phi} = \frac{\pi\Phi}{\Phi_0}$ . Charge basis can be used to solve the spectrum of  $H_0$  analytically in a truncated version (truncated up to  $N$ ):

$$\hat{n} = \sum_{i=1}^N |i\rangle \langle i| \quad (2.20)$$

$$\cos \hat{\phi} = \sum_{i=1}^N (|i+1\rangle \langle i| + |i\rangle \langle i+1|) \quad (2.21)$$

The spectrum is calculated through matrix diagonalization by plugging in the matrix representation of all operators.

Assuming the coupling capacitance  $C_{qr}$  and the SQUID anharmonicity are small, we can also perform perturbation calculations of the energy spectrum. The Hamiltonian is first

separated into three parts: the capacitive term  $H_c$ , the linear inductive term  $H_l$ , and the pure nonlinear term  $H_{nl}$ :

$$H_c = \frac{1}{2} \frac{(C_q + C_{qr})Q_r^2 + (C_r + C_{qr})Q_q^2 + C_{qr}Q_rQ_q}{(C_r + C_{qr})(C_q + C_{qr}) - C_{qr}^2} \quad (2.22)$$

$$H_l = \frac{\Phi_r^2}{2L_r} + E_J \cos\left(\frac{\pi\Phi_e}{\Phi_0}\right) \left(\frac{2\pi\Phi_q}{\Phi_0}\right)^2 \quad (2.23)$$

$$H_{nl} = -2E_J \cos\left(\frac{\pi\Phi_e}{\Phi_0}\right) \left(\cos\left(\frac{2\pi\Phi_q}{\Phi_0}\right) + \frac{1}{2}\left(\frac{2\pi\Phi_q}{\Phi_0}\right)^2 - 1\right) \quad (2.24)$$

We first diagonalize  $H_c + H_l$ . For expression simplicity, we define

$$\vec{\Phi}^T = (\Phi_r, \Phi_q) \quad (2.25)$$

$$\vec{Q}^T = (Q_r, Q_q) \quad (2.26)$$

$$C = \begin{bmatrix} C_r + C_{qr} & -C_{qr} \\ -C_{qr} & C_q + C_{qr} \end{bmatrix} \quad (2.27)$$

$$L_l = \begin{bmatrix} L_r & 0 \\ 0 & \frac{\Phi_0^2}{4\pi^2 E_j \cos\left(\frac{\pi\Phi_e}{\Phi_0}\right)} \end{bmatrix} \quad (2.28)$$

$$(2.29)$$

Then we have:

$$H_c + H_l = \frac{1}{2} (\vec{Q}^T C^{-1} \vec{Q} + \vec{\Phi}^T L_l^{-1} \vec{\Phi}) \quad (2.30)$$

Using linear algebra, we can find a nonsingular matrix  $U$  such that  $U^{-1}C^{-1}U$  and  $U^{-1}L_l^{-1}U$  are both diagonal matrices. In the new basis  $\tilde{\vec{Q}} = U^{-1}\vec{Q}$ ,  $\tilde{\vec{\Phi}} = U^{-1}\vec{\Phi}$ , the linear part is fully diagonalized, and second quantization is straightforward in the decoupled linear oscillator system. we reintroduce  $H_{nl}$  and replace the  $\Phi_q$  with the annihilation operator. Taylor expansion of the cosine function in  $H_{nl}$  can be kept to arbitrary order to

perform the perturbation calculation.

Assuming the resonator and SQUID are dispersively coupled [79], we can relabel the energy spectrum from bottom to top after matrix diagonalization. The first eigenstate primarily associated with the SQUID or resonator corresponds to  $|0e\rangle$  or  $|1g\rangle$ , respectively. Here,  $|nm\rangle$  means the resonator-like mode is at state  $|n\rangle$ , and the SQUID-like mode is at state  $|m\rangle$ . All higher eigenstates can be classified similarly.

## 2.2 Transmon Two-qubit Gate Implementation

Universal quantum computing requires access to a universal quantum gate set [67], which includes both single-qubit and two-qubit gates. Specifically, combinations of single-qubit rotations and CNOT gates are sufficient to achieve universal quantum computing. High-fidelity ( $> 99.99\%$ ) and fast ( $< 20ns$ ) single-qubit control [47] has been realized in the transmon system [45] through advancement in transmon coherence and optimal-pulse control [64]. However, the two-qubit gate is still the bottleneck for the transmon system to scale up. There are many directions toward two-qubit gate implementations, but the basic idea is to engineer strong two-qubit interactions with the large on-off ratio in the system Hamiltonian while maintaining transmon coherence. Here, the on-off ratio refers to the ratio of gate strength and the maximum stray interaction strength when the system is idle. Putting two transmons close to each other (introducing a “stray” capacitive coupling) naturally provides an always-on ZZ interaction. While the ZZ interactions can be easily converted to a Cphase gate (therefore a CNOT gate) by waiting an appropriate time, such implementation has the lowest on-off ratio. For the transmon system, one concern when designing a new two-qubit gate is to suppress/cancel the stray ZZ interactions between qubits. The ratio of gate speed over ZZ interactions quantifies the on-off ratio in this context.

Different two-qubit gate implementations are reviewed below. For convenience, Fig. 2.2 summarizes some popular two-qubit gate schemes.

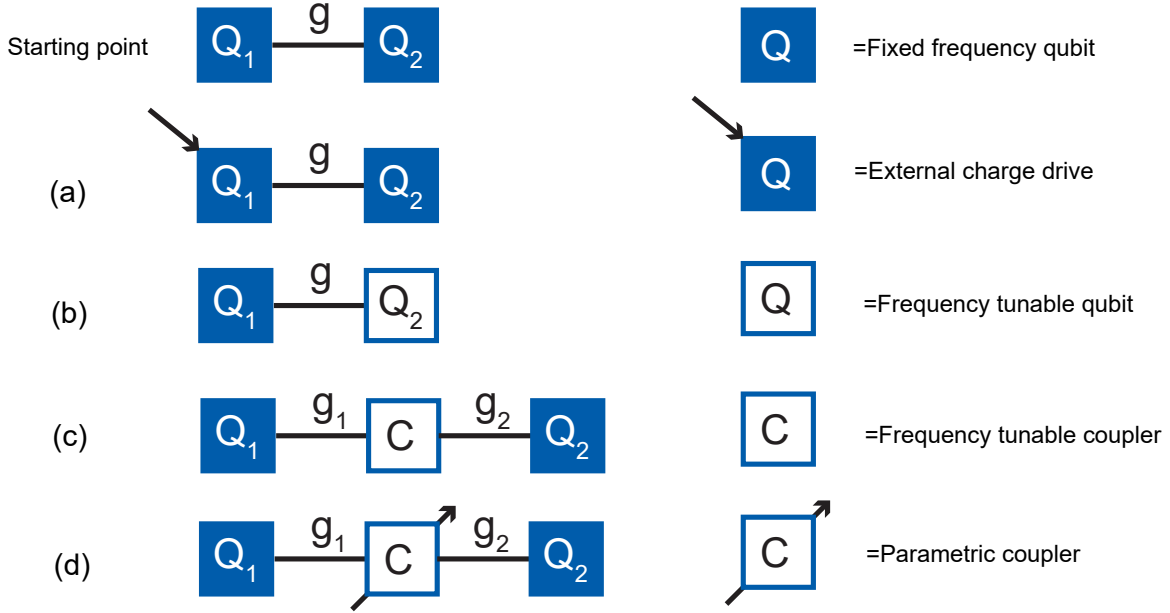


Figure 2.2: Different two-qubit gate implementations. (a) Cross-resonance gate. (b) Diabatic gate. (c) Coupler mediated diabatic gate. (d) Parametric gate.

### 2.2.1 Cross-resonance gate

Cross-resonance gate (CR gate) [68, 15, 85, 58, 59] is a scalable, all-microwave two-qubit gate scheme on two capacitively coupled qubits. The requirements of fixed-frequency only qubits ensure great qubit coherence and robustness. We label the frequency and anharmonicity of the two qubits (controlled qubit  $Q_c$ , target qubit  $Q_t$ ) as  $\{\omega_c, \omega_t\}$  and  $\{\alpha_c, \alpha_t\}$ . The capacitive coupling strength between the two qubits is  $g \ll |\omega_c - \omega_t|$ . The cross-resonance gate is realized through the cross-resonance effect: driving  $Q_c$  at  $\omega_t$  will effectively drive  $Q_t$  with strength  $\epsilon$ . When  $Q_c$  is nonlinear,  $\epsilon$  is dependent on the state of  $Q_c$ , thus entangling two qubits.

The system Hamiltonian is (See Fig. 2.3 with an external drive on  $Q_t$  at frequency  $\omega_d$ , strength  $\Omega$ , phase  $\phi$ ):

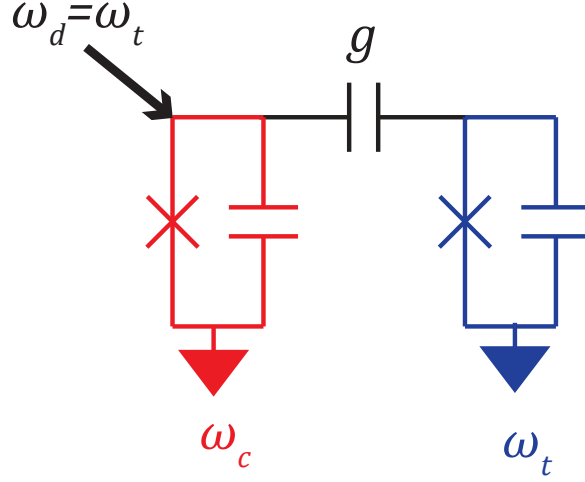


Figure 2.3: Circuit diagram for realizing the cross-resonance gate. A controlled qubit is charge-driven at the target qubit frequency to activate an effective ZX interaction.

$$H_{cr} = \omega_c a_c^\dagger a_c + \omega_t a_t^\dagger a_t + \frac{\alpha_c}{2} a_c^\dagger a_c^\dagger a_c a_c + \frac{\alpha_t}{2} a_t^\dagger a_t^\dagger a_t a_t - g(a_c^\dagger - a_c)(a_t^\dagger - a_t) + H_d \quad (2.31)$$

$$H_d = \Omega \cos(\omega_d t + \phi)(a_c^\dagger + a_c) \quad (2.32)$$

For simplicity, we follow Reference [85] to derive the first-order approximation of an ideal CR gate rate: we label the dressed basis eigenstates of  $H_{cr}$  when  $\Omega = 0$  as  $|n, m\rangle_d$ . Here  $\{n, m\}$  indicates the excitation number in  $Q_c$  and  $Q_t$  separately. Compared with eigenstate  $|n, m\rangle$  in the uncoupled case ( $g = 0$ ), the eigenenergy ( $E_{|n, m\rangle_d}$  for dressed basis case,  $E_{|n, m\rangle}$  for uncoupled case) is slightly different. With the first-order approximation, we ignore the difference and approximate as  $\omega_d = \omega_t = E_{|0, 1\rangle_d} - E_{|0, 0\rangle_d}$ .

In the dressed basis, we use Rotating wave approximation (RWA) to keep the slow term in  $H_d$ :

$$H_d \simeq \sum_i \Omega_i |i, 1\rangle_d \langle i, 0|_d + h.c. \quad (2.33)$$

Here  $\Omega_i$  is the state-dependent drive strength on  $Q_t$ . When both qubits have no nonlinearity,  $\Omega_i = \Omega$  ends up with no entanglement. In the dispersive coupling regime, we have the following first-order approximation for the dressed basis [15]:

$$|0, 0\rangle_d = |0, 0\rangle \quad (2.34)$$

$$|0, 1\rangle_d = |0, 1\rangle - \frac{g}{\omega_c - \omega_t} |1, 0\rangle \quad (2.35)$$

$$|1, 0\rangle_d = |1, 0\rangle + \frac{g}{\omega_c - \omega_t} |0, 1\rangle \quad (2.36)$$

$$|1, 1\rangle_d = |1, 1\rangle - \frac{\sqrt{2}g}{\omega_c - \omega_t + \alpha_c} |2, 0\rangle + \frac{\sqrt{2}g}{\omega_c - \omega_t - \alpha_t} |0, 2\rangle \quad (2.37)$$

We can perturbatively calculate the first two  $\Omega_i$ :

$$\Omega_0 = \langle 0, 1|_d H_d |0, 0\rangle_d = \langle 0, 1|_d \Omega (a_c^\dagger + a_c) |0, 0\rangle_d = -\frac{g\Omega}{\omega_c - \omega_t} \quad (2.38)$$

$$\Omega_1 = \langle 1, 1|_d H_d |1, 0\rangle_d = \frac{g\Omega}{\omega_c - \omega_t} - \frac{2g\Omega}{\omega_c - \omega_t + \alpha_c} \quad (2.39)$$

Restricted to the first two-level of both qubits,  $H'_d$  can be expressed as [15, 85]:

$$H'_d = \frac{\Omega_0 - \Omega_1}{2} ZX + \frac{\Omega_0 + \Omega_1}{2} IX \quad (2.40)$$

The IX interactions can be canceled through extra single qubit rotations on  $Q_t$ . The coefficient in front of the ZX term is the CR gate rate, which is:

$$\frac{\Omega_0 - \Omega_1}{2} = -\frac{g\Omega}{\omega_c - \omega_t} + \frac{g\Omega}{\omega_c - \omega_t + \alpha_c} = \frac{-g\Omega\alpha_c}{(\omega_c - \omega_t)(\omega_c - \omega_t + \alpha_c)} \quad (2.41)$$

Notice that this is just a first-order approximation, and the actual CR gate rate deviates from Eq. 2.41 needs higher-order corrections when the microwave drive strength  $\Omega$  becomes comparable to  $\omega_c - \omega_t$ . The linear approximation gives us a basic understanding of the rate: For qubits with large anharmonicity, such as fluxonium [20], the cross-resonance effect might be more significant and easy to achieve fast CR gate. For transmon, the anharmonicity is relatively small, and the cross-resonance effect is most significant when  $|\alpha_c| \sim |\omega_c - \omega_t|$ . However, as we will discuss in Sec. 2.2.4, the static ZZ coupling between two transmons is  $\frac{-2g^2(\alpha_c + \alpha_t)}{(\omega_t - \omega_c + \alpha_t)(\omega_c - \omega_t + \alpha_c)}$ . Therefore, the on-off ratio completely relies on increasing  $\Omega$  and is hard to improve by tuning the frequency spectrum.

### 2.2.2 Diabatic gate

More circuit complexity is considered to improve the on-off ratio and speed up the two-qubit gate for better fidelity. One direction is to introduce a tunable qubit in the system. Suppose a flux-tunable qubit is capacitively coupled to a fixed-frequency qubit (See Fig. 2.4)

We treat both transmons ( $Q_1, Q_2$ ) as a two-level system of frequencies ( $\omega_1, \omega_2$ ) for simplicity. The system Hamiltonian is:

$$H_{db} = \frac{1}{2}(\omega_1(\Phi_e)\sigma_1^z + \omega_2\sigma_2^z) + g(\sigma_1^+\sigma_2^- + h.c.) \quad (2.42)$$

Here,  $\omega_1(\Phi_e)$  is DC flux tunable and capacitively coupled to  $Q_2$  with coupling strength

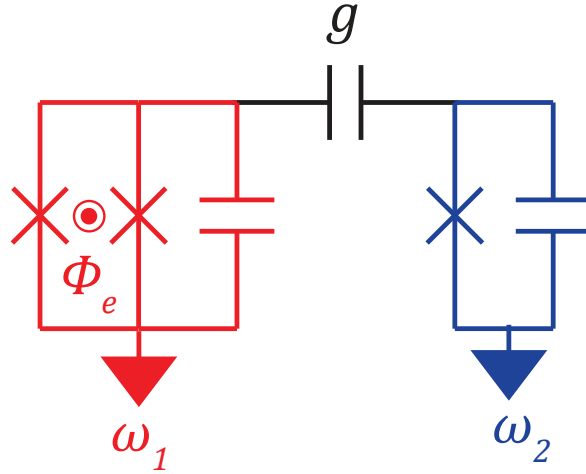


Figure 2.4: Circuit diagram for the realizing diabatic gate. A flux tunable qubit is capacitively coupled to a fixed frequency qubit. Single photon swap happens at rate  $g$  when both qubits have the same frequency.

$g$ . By tuning  $\omega_1(\Phi_e) = \omega_2$ , the rotating frame Hamiltonian becomes:

$$H_{db} = \frac{1}{2}g(\sigma_1^+ \sigma_2^- + \sigma_1^- \sigma_2^+) \quad (2.43)$$

which describes a photon swap between  $Q_1$  and  $Q_2$  at rate  $g$ . After leaving both qubits on-resonance for  $\frac{\pi}{g}$  and biasing  $Q_1$  frequency away from  $Q_2$ , an ISWAP gate is realized in the two-qubit system. Typical circuit design can easily realize  $g > 50$  MHz, which provides a fast two-qubit gate. The on-off ratio for this scheme is around  $\frac{\omega_1 - \omega_2}{g}$ , typically better than the transmon cross-resonance gate case.

A third element, the tunable coupler, is added to the circuit to improve the gate fidelity [90, 83] through canceling the static ZZ interactions.

The system Hamiltonian is:

$$H_{dbc} = \sum_{i=1,2,c} (\omega_i a_i^\dagger a_i + \alpha_i a_i^\dagger a_i^\dagger a_i a_i) - g_1(a_1^\dagger - a_1)(a_c^\dagger - a_c) - g_2(a_2^\dagger - a_2)(a_c^\dagger - a_c) - g_{12}(a_1^\dagger - a_1)(a_2^\dagger - a_2) \quad (2.44)$$

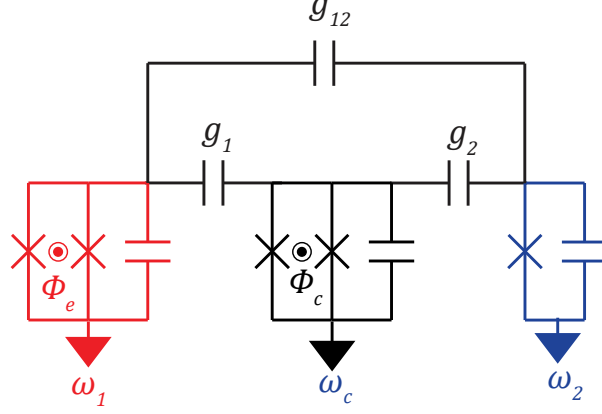


Figure 2.5: Circuit diagram for realizing the high fidelity diabatic gate with ZZ cancellation. The coupler frequency  $\omega_c$  is biased to a ZZ-free point for idling and biased to an “on” point for a fast two-qubit gate.

Using the SW transformation with  $U = \exp(A_1 + A_2)$  [90] to remove the coupler mode (assuming coupler mode remains in its ground state):

$$A_1 = \frac{g_1}{\omega_1 - \omega_c} (a_1^\dagger a_c - a_1 a_c^\dagger) - \frac{g_1}{\omega_1 + \omega_c} (a_1^\dagger a_c^\dagger - a_1 a_c) \quad (2.45)$$

$$A_2 = \frac{g_2}{\omega_2 - \omega_c} (a_2^\dagger a_c - a_2 a_c^\dagger) - \frac{g_2}{\omega_2 + \omega_c} (a_2^\dagger a_c^\dagger - a_2 a_c) \quad (2.46)$$

and assuming  $g_i \ll \omega_j - \omega_c$ , we have (up to second order in the total photon excitation)

$$H'_{dbc} = U H_{dbc} U^\dagger = \sum_{i=1,2} (\tilde{\omega}_i a_i^\dagger a_i + \alpha_i a_i^\dagger a_i^\dagger a_i a_i) + \tilde{g} (a_1^\dagger a_2 + a_1 a_2^\dagger) \quad (2.47)$$

$$\tilde{\omega}_i = \omega_i + g_i^2 \left( \frac{1}{\omega_i - \omega_c} - \frac{1}{\omega_i + \omega_c} \right) \quad (2.48)$$

$$\tilde{g} = g_{12} + \frac{g_1 g_2}{2} \sum_{j=1,2} \left( \frac{1}{\omega_j - \omega_c} - \frac{1}{\omega_j + \omega_c} \right) \quad (2.49)$$

The effective ZZ coupling between two qubits is  $\frac{-2\tilde{g}^2(\alpha_1 + \alpha_2)}{(\omega_1 - \omega_2 + \alpha_2)(\omega_1 - \omega_2 - \alpha_1)} \propto \tilde{g}^2$ . When the coupler mode frequency is biased between two qubits, it is possible to find out a DC flux point (Idling point) for the coupler such that  $\tilde{g} = 0$ . The gate scheme starts with the coupler

at the (Idling point).  $\omega_1$  and  $\omega_c$  are DC simultaneously DC biased to the operating points, waiting for a full photon swap between  $Q_1$  and  $Q_2$ , then bias back to the Idling point again. This scheme allows a high-fidelity, fast, and scalable two-qubit gate approaching 99.9% [83] after careful pulse control to suppress leakage error. One challenge is to achieve a decent coherence for  $Q_2$ , which usually has low  $T_2$ .

### 2.2.3 Parametric modulation gate

The parametric modulation scheme aims to realize a fast two-qubit gate between fixed-frequency qubits for better coherence [70, 13].

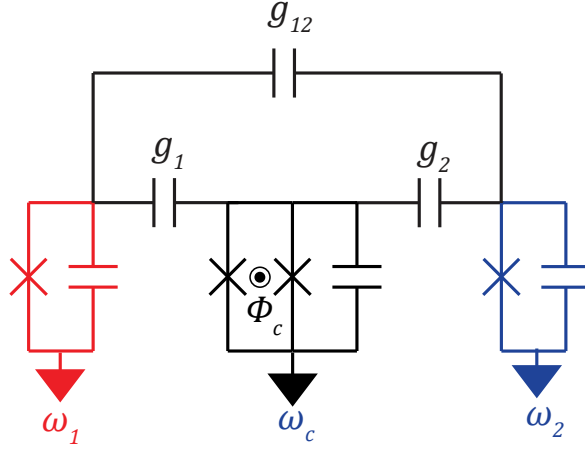


Figure 2.6: Circuit diagram for realizing the parametric gate.

The system Hamiltonian is:

$$\begin{aligned}
 H_{para} = & \sum_{i=1,2} (\omega_i a_i^\dagger a_i + \alpha_i a_i^\dagger a_i^\dagger a_i a_i) + \omega_c (\Phi_c) a_c^\dagger a_c \\
 & - g_1 (a_1^\dagger - a_1)(a_c^\dagger - a_c) - g_2 (a_2^\dagger - a_2)(a_c^\dagger - a_c) - g_{12} (a_1^\dagger - a_1)(a_2^\dagger - a_2) \quad (2.50)
 \end{aligned}$$

We modulate  $\Phi_c$  with amplitude  $\epsilon$ , modulation frequency  $\omega_d$ , around the DC flux point

$\Phi_{c0}$ :

$$\Phi_c = \Phi_{c0} + \epsilon \cos(\omega_d t) \quad (2.51)$$

The coupler SQUID frequency-DC flux response ( $\omega_c \simeq \omega_0 \sqrt{|\cos(\frac{\pi\Phi_c}{\Phi_0})|}$ ) allows us to expand  $\omega_c$  when  $\epsilon$  is small [70]:

$$\omega_c \simeq \omega_{c0} + \epsilon \frac{\partial \omega_c(\Phi)}{\partial \Phi} \Big|_{\Phi=\Phi_{c0}} \cos(\omega_d t) + \frac{\epsilon^2}{2} \frac{\partial^2 \omega_c(\Phi)}{\partial \Phi^2} \Big|_{\Phi=\Phi_{c0}} \cos^2(\omega_d t) \quad (2.52)$$

Assuming  $\epsilon$  is small, we perform the time-dependent SW transformation to do perturbation expansion. For expression simplicity, we set  $g_{12} = 0$  and discuss its contribution in the next section. Suppose  $H_{para} = H_0 + V$ , here  $H_0$  is a diagonal matrix, and

$$V = -g_1(a_1^\dagger - a_1)(a_c^\dagger - a_c) - g_2(a_2^\dagger - a_2)(a_c^\dagger - a_c) \quad (2.53)$$

contains only off-diagonal terms. The goal is to find a unitary  $U = \exp(S(t))$ , with  $S(t) = -S^\dagger(t)$ , such that to the first order  $H'_{para} = UH_0U^\dagger - iU(\frac{\partial U}{\partial t})^\dagger$  is diagonal:

$$H'_{para} \simeq H_0 + V + i \frac{\partial S}{\partial t} + [S, H_0] + [S, V] + i[S, \frac{\partial S}{\partial t}] + \frac{1}{2}[S, [S, H_0]] \quad (2.54)$$

$$0 = V + i \frac{\partial S}{\partial t} + [S, H_0] \quad (2.55)$$

We choose the anti-hermitian operator  $S$  as [70] and approximate all transmons as two-level systems:

$$S = \sum_{i=1,2} (\gamma_i^-(t) \sigma_i^+ \sigma_c^- + \gamma_i^+(t) \sigma_i^- \sigma_c^+ - h.c.) \quad (2.56)$$

Here,  $\sigma_j^\pm, j = 1, 2, c$  are Pauli operators for different qubits. Eq. 2.54 is further simplified as:

$$H'_{para} = \sum_{i=1,2,c} \omega_i \tilde{\omega}_i \sigma_i^z + \Omega_r(t)(\sigma_1^- \sigma_2^+ + h.c.) + \Omega_b(t)(\sigma_1^- \sigma_2^- + h.c.) \quad (2.57)$$

When  $\omega_d \simeq \omega_1 - \omega_2$ ,  $\Omega_r(t)$  becomes time independent [70]:

$$\Omega_r = \epsilon \frac{g_1 g_2}{4} \frac{\partial \omega_c(\Phi_{c0})}{\partial \Phi} \left( \frac{1}{(\omega_1 - \omega_c)(\omega_2 - \omega_c)} + \frac{1}{(\omega_1 + \omega_c)(\omega_2 + \omega_c)} \right) \quad (2.58)$$

And the QQ red sideband (beam-splitter-like) interactions are turned on between  $Q_1$  and  $Q_2$ .

When  $\omega_d \simeq \omega_1 + \omega_2$ ,  $\Omega_b(t)$  becomes time independent [70]:

$$\Omega_b = \epsilon \frac{g_1 g_2}{4} \frac{\partial \omega_c(\Phi_{c0})}{\partial \Phi} \left( \frac{1}{(\omega_c - \omega_1)(\omega_2 + \omega_c)} + \frac{1}{(\omega_1 + \omega_c)(\omega_c - \omega_2)} \right) \quad (2.59)$$

And the QQ blue sideband (squeezing-like) interactions are turned on between  $Q_1$  and  $Q_2$ .

The parametric gate sideband rate is determined by the product of the following elements: modulation amplitude, coupling strength, coupler frequency sensitivity, and frequency configuration. The effective ZZ coupling  $\frac{-2\tilde{g}^2(\alpha_1 + \alpha_2)}{(\omega_1 - \omega_2 + \alpha_2)(\omega_1 - \omega_2 - \alpha_1)}$  is the same as the Diabatic gate case. Canceling the start ZZ interactions in the parametric modulation case is more complicated: when the parametric drive is off, zero ZZ means  $\tilde{g} = 0$ . When the parametric drive is on, the AC-stark shift effect introduces “dynamical ZZ” between two qubits. Depending on the two-qubit gate type, the dynamical ZZ can speed up the gate (CZ gate) or reduce gate fidelity (iSWAP, bSWAP) and requires additional cancellation steps [29].

#### 2.2.4 Stray ZZ interactions

Stray ZZ interactions are among the dominant coherent errors limiting the fidelity of two-qubit gates. Achieving zero ZZ interactions is crucial for any high-fidelity two-qubit gate

scheme. We begin by considering the scenario depicted in Fig. 2.2: two transmon qubits capacitively coupled with an interaction strength  $g$ . The static ZZ coupling strength (up to second-order perturbation theory) is given by

$$J_{zz} = \frac{-2g^2(\alpha_1 + \alpha_2)}{(\omega_2 - \omega_1 + \alpha_2)(\omega_1 - \omega_2 + \alpha_1)}, \quad (2.60)$$

where  $\omega_2 > \omega_1$  and  $\omega_1$  is tunable. Notice that as  $\omega_1$  is tuned across  $\omega_2 + \alpha_2$ , the sign of  $J_{zz}$  rapidly changes from negative to positive. Therefore, it is possible to achieve  $J_{zz} = 0$  near the transmon straddling regime.

An alternative approach involves replacing one transmon with an element with positive anharmonicity, such as a flux qubit (capacitively-shunted) or fluxonium. In this case, achieving a zero ZZ point does not require the system to be in the straddling regime, which can help avoid frequency crowding.

Introducing a third element, either a qubit functioning as a coupler or a linear element such as a shared resonator, often simplifies the process of canceling ZZ interactions. For a system comprising two transmons and one coupler, the conditions for zero ZZ interactions are outlined in Ref. [65]:

1. By tuning the coupler frequency, the only zero ZZ point occurs when the coupler frequency lies between the frequencies of the two transmons, provided the transmons are not in the straddling regime.
2. When the two transmons are in the straddling regime, it is possible to find a configuration of frequencies and coupling strengths such that the only zero ZZ point occurs when the coupler frequency is beyond both transmon frequencies.

To further increase the number of zero ZZ points, Ref. [65] also introduces a fourth mode. In this configuration, the entire region between two zero ZZ points exhibits suppressed stray ZZ interactions, thereby tolerating calibration errors more effectively.

Instead of increasing circuit complexity, additional drives can also be used to cancel stray ZZ interactions through the AC Stark shift [62, 35]. Ref. [35] illustrates this approach clearly: achieving zero ZZ can be realized by independently addressing the energy of the  $|ee\rangle$  state. Sideband interactions such as  $|ee\rangle \leftrightarrow |gf\rangle$  or  $|ee\rangle \leftrightarrow |fg\rangle$  couple  $|ee\rangle$  to a state outside of the logical basis, providing a mechanism to tune  $|ee\rangle$  independently. By adjusting the coupling strength through external drive controls, it is possible to fully cancel ZZ interactions.

### 2.3 Transmon state tomography

In this section, we discuss the implementation of qubit state tomography, a useful experimental characterization used in all the following experiments discussed in this thesis. We generalize the tomography technique to compensate for the static ZZ interactions [75].

We consider a two-transmon device for simplicity. The system density matrix  $\rho$  can be represented as:

$$\rho = \frac{1}{2^2} \sum_{i_1, i_2=0}^3 n_{i_1, i_2} \sigma_{i_1} \otimes \sigma_{i_2} \quad (2.61)$$

Here, the real coefficient  $n_{i_1, i_2}$  represents the expectation value of the multi-qubit Pauli operator  $\sigma_{i_1} \otimes \sigma_{i_2}$ . Here,  $\sigma_i, i = 0, 1, 2, 3$  represents the identity and Pauli matrices. Once all  $n_{i_1, i_2}$  values are known,  $\rho$  can be directly written out. To measure  $n_{i_1, i_2}$ , after preparing  $\rho$ , people typically apply single qubit rotations  $\{\sigma_i\}$  to both qubits before measurement. With enough single-shot numbers, each  $n_{i_1, i_2}$  can be experimentally approximated as  $\tilde{n}_i$  using measurement statistics. The reconstructed density matrix  $\rho_m$  can be calculated in different methods:

Direct-inversion: The tomography reconstructed density matrix is written as:  $\rho_m = \frac{1}{2^2} \sum_{i_1, i_2=0}^3 \tilde{n}_{i_1, i_2} \sigma_{i_1} \otimes \sigma_{i_2}$ . However, measurement errors in experiments almost always lead to an unphysical  $\rho_m$  in this case.

Maximum-Likelihood Estimation: A physical density matrix can be represented as  $\rho_{mle} = \Lambda^T \Lambda / \text{tr}(\Lambda^T \Lambda)$ , where  $\Lambda$  is a complex upper triangular matrix, and  $\text{tr}(\cdot)$  is the matrix trace operator. We define the following cost function:

$$L \sum_{i=1}^{4^2} \frac{(\langle \psi_i | \rho_{mle} | \psi_i \rangle - \tilde{n}_i)^2}{\langle \psi_i | \rho_{mle} | \psi_i \rangle} \quad (2.62)$$

Here,  $|\psi_i\rangle \langle \psi_i|$  forms the  $4^2$  tomography measurement basis. In the experiments, one might choose more projectors ( $6^2$  in our case) that form an over-complete basis. The MLE reconstructed density matrix is calculated by minimizing the cost function  $L$ .

However, in certain experiments, the stray interactions between transmons, such as the residual ZZ coupling, are too strong to be fully canceled. This makes it more challenging to calibrate independent qubit rotations [52]. The inability to perform independent single-qubit rotations appears to hinder the standard MLE tomography. Here, instead of engineering the universal single qubit rotation set for tomography, we can compensate for the stray ZZ directly in the tomography operation [75].

For expression simplicity, we assume that the system Hamiltonian is expressed as:

$$H = H_0 + H_c + H_d \quad (2.63)$$

$$H_0 = \sum_i \omega_i \sigma_z^i \quad (2.64)$$

$$H_c = \sum_{n,m} J_{nm} |nm\rangle \langle nm| \quad (2.65)$$

Here  $\sigma_z^i$  is the  $i$ th qubit pauli operator,  $|nm\rangle$  represents the two-qubit state being at  $|n\rangle \otimes |m\rangle$ , and  $J_{nm}$  is the coupling strength. When only considering the static ZZ interactions with strength  $J$ ,  $H_c = J_{11} |11\rangle \langle 11|$ .  $H_d$  contains all driving terms that represent the tomography rotations.

Fig. 2.7(a) shows our compensated tomography steps: We still apply the tomography

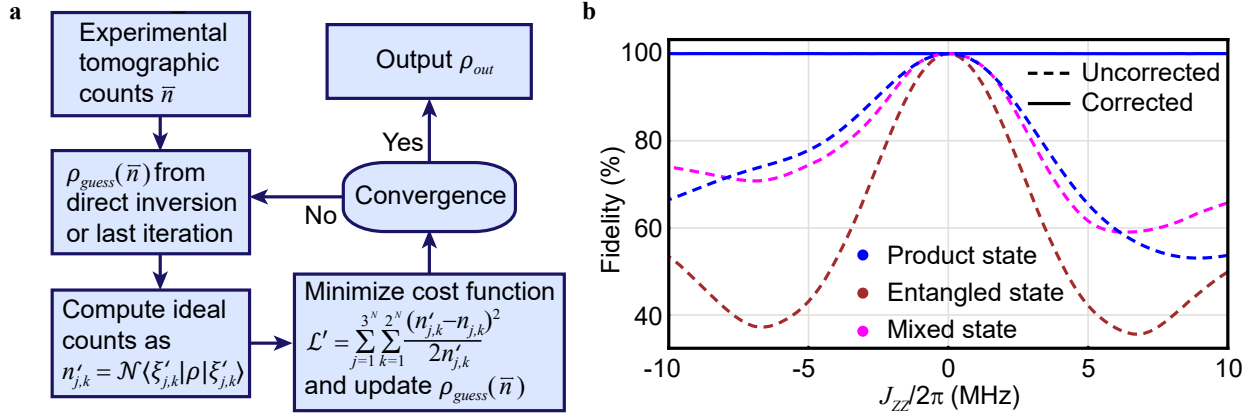


Figure 2.7: ZZ compensated tomography scheme and its application on a two-qubit system. (a) Tomography steps flow chart. The central idea is to use the system Hamiltonian to update the ideal tomography counts and perform MLE accordingly. (b) Comparison of simulated fidelities for a two-qubit system with ZZ coupling. Dashed lines: Standard MLE tomography. Solid lines: ZZ compensated tomography scheme. Three representative states (see text for description) — a product (blue), an entangled (brown), and a mixed (magenta) are chosen to show the effectiveness of ZZ compensated tomography.

rotations in the standard MLE:

$$H_d = \sum_{i=1}^2 B_i(t) \sin(\omega_i t - \phi_i) \sigma_x^i \quad (2.66)$$

$B_i(t)$  and  $\phi_i$  are separately the drive amplitude and phases on  $i$ th qubit, and a set of  $3^2$  rotations are chosen to cover the Bloch sphere cardinal points in the absence of  $H_c$ . We still follow the same experimental pulses and collect the tomography counts  $\vec{n}$  (with  $6^2$  elements) in the presence of  $H_c$ . The evolution operators for the  $3^2$  pre-rotations  $U_j(t_0, t)$  are calculated as:

$$U_j(t_0, t) = \mathcal{T} e^{-i \int_{t_0}^t (H_0 + H_c + H_d(t')) dt'} \quad (2.67)$$

where  $t_0$  is the beginning of the pulse being applied and  $\mathcal{T}$  represents the *time-ordering*

operator. We modify the  $6^2$  projectors  $|\psi_i\rangle\langle\psi_i|$  by calculating:

$$|\tilde{\xi}_i\rangle = U_j(t_0, t) |nm\rangle, n, m = 0, 1 \quad (2.68)$$

The modified MLE cost function is:

$$L = \sum_{i=1}^{6^2} \frac{\left(\langle\tilde{\xi}_i|\rho_{mle}|\tilde{\xi}_i\rangle - \tilde{n}_i\right)^2}{\langle\tilde{\xi}_i|\rho_{mle}|\tilde{\xi}_i\rangle} \quad (2.69)$$

The initial guess  $\rho_{guess}(\vec{n})$  can be obtained from standard MLE and then updated iteratively using the modified basis. Fig. 2.7(b) plots the simulated fidelity of the tomographic reconstruction for three randomly chosen initial states — (1) a product state (purple lines):  $|\psi_p\rangle = (|g\rangle + |e\rangle)^{\otimes 2}/2$ , (2) an entangled state (brown lines):  $|\psi_e\rangle = (|gg\rangle + |ee\rangle)/\sqrt{2}$ , and (3) a mixed state (magenta lines):  $0.8|\psi_p\rangle\langle\psi_p| + 0.2|\psi_e\rangle\langle\psi_e|$  as a function of cross-Kerr coupling strength  $J_{zz}$ . The dashed lines show that the states are not correctly reproduced for non-zero  $J_{zz}$  when regular tomography is used, whereas solid lines show that compensated tomography completely recovers the correct state.

# CHAPTER 3

## THE STAR CODE THEORY

The random interactions with the environment limit the performance of quantum computers. Random errors can be viewed as the entropy entering the system from an external heat source. Quantum error correction is necessary to remove the entropy continuously and cool the system without knowing the logical states. For large-scale quantum computers, topological codes such as surface code [27, 84] are promising candidates to achieve fault tolerance. However, the precision feedback control, large physical qubit number overhead, quantum processor’s clock time[5], and decoding with classical computers are challenging for experimental implementation. Autonomous Quantum Error Correction offers a compelling complementary solution for near-term algorithms and as a building block for future topological codes.

This chapter discusses our theoretical proposal for realizing Autonomous Quantum Error Correction in a pure transmon system. We begin with the original proposal, the Very Small Logical Qubit (VSLQ) [37], and discuss its theoretical performance and experimental challenges. Then, we propose a new error correction code, the Star Code, that avoids the higher-order interaction requirements. We discuss the Star code performance, including the logical state coherence and single logical gate implementation. We further list the necessary experimental requirements to realize this code that inspires our experimental demonstrations.

### 3.1 The Very Small Logical Qubit

Consider a system of two transmon-two resonators ( $Q_1Q_2R_1R_2$ ). The VSLQ encodes a single logical qubit out of two transmons using the first three levels  $\{|g\rangle, |e\rangle, |f\rangle\}$  of each transmon. The logical “zero” and “one” are defined as  $|L_0\rangle = (|g\rangle - |f\rangle)(|g\rangle - |f\rangle)/2$  and

---

Parts of this chapter have been published in Ref. [49]

$|L_1\rangle = (|g\rangle + |f\rangle)(|g\rangle + |f\rangle)/2$  respectively. VSLQ aims to correct single-photon loss errors (Transmon decay rate  $\gamma$ ) and suppresses low-frequency dephasing errors, the two dominant error sources in the transmon system. To suppress low-frequency dephasing noise, we use Floquet engineering to create an energy gap  $W$  between the logical and error states. This energy gap echoes all the noise with an energy spectrum lower than  $W$ . To correct single-photon loss, we engineer an active decay channel  $|e\rangle \rightarrow |f\rangle$  for both transmons with the help of coupled lossy resonators (decay rate  $\kappa$ ). Restricting the system's Hilbert space to  $3 \times 3 \times 2 \times 2$  ( $Q_1 Q_2 R_1 R_2$ ) for simplicity, the rotating frame VSLQ Hamiltonian  $H_{\text{vslq}}$  is [37]:

$$H_{\text{vslq}} = H_P + H_R + H_{PR} \quad (3.1)$$

$$H_P = -W\tilde{X}_1\tilde{X}_2 + \frac{\alpha}{2}(|e\rangle\langle e| \otimes I_2 + I_2 \otimes |e\rangle\langle e|) \otimes I_9 \quad (3.2)$$

$$H_R = \Omega(a_{q1}a_{r1} + a_{q2}a_{r2} + h.c.) + \frac{\alpha}{2}(a_{r1}^\dagger a_{r1} + a_{r2}^\dagger a_{r2}) \quad (3.3)$$

$$H_{PR} = W(a_{r1}^\dagger a_{r1} + a_{r2}^\dagger a_{r2}) \quad (3.4)$$

Here,  $a_{qi}$  and  $a_{ri}$  are separately the  $i$ -th transmon and resonator's annihilation operator.  $\tilde{X}_i = (a_{qi}a_{qi} + h.c.)/2$ ,  $W$  is the transmon sideband rate,  $\Omega$  is the transmon-resonator sideband rate,  $\alpha$  is the transmon anharmonicity (assumed to be the same for both transmons) and  $I_n$  is the identity matrix of dimension  $n \times n$ .  $H_{\text{vslq}}$  is separated into three parts:  $H_P$  contains all the two transmon sidebands to create the logical space. When projected to the lowest three levels for each transmon,  $-W\tilde{X}_1\tilde{X}_2$  describes simultaneously applied two sideband interactions  $|gf\rangle \leftrightarrow |fg\rangle$  and  $|gg\rangle \leftrightarrow |ff\rangle$  of the same rate  $W$ . The other term in  $H_P$  comes from the rotating frame transformation with the transformation unitary  $U_{\text{vslq}} = \exp\left[i\sum_{j=1,2}(\omega_{qj} + \frac{\alpha}{2})a_{qj}^\dagger a_{qj}t\right]$ , and  $\omega_{qj}$  is  $Q_j$ 's frequency.  $H_R$  describes the two-photon pumping process  $|e0\rangle \leftrightarrow |f1\rangle$  between each QR pair at rate  $\Omega$ .  $H_{PR}$  describes the frequency detunings  $W$  for  $|e0\rangle \leftrightarrow |f1\rangle$  to maximize the transfer rate from error state to

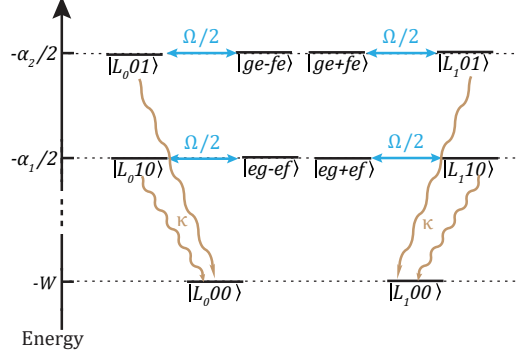


Figure 3.1: VSLQ energy diagram. For simplicity, the two QQ interactions  $|gf\rangle \leftrightarrow |fg\rangle$  and  $|gg\rangle \leftrightarrow |ff\rangle$  are assumed to be both  $W$ . And the QR interactions are assumed to be both  $\Omega$ .

logical state.

Assuming  $W \gg \Omega$ , the QR sideband interactions can be treated as perturbations.  $|L_0\rangle$  and  $|L_1\rangle$  are the eigenstates of  $H_P$  with energy  $-W$ , and the other states are at least  $O(W)$  away from the logical manifold, and specifically the single-photon loss error states  $\{|E_{00}\rangle, |E_{10}\rangle, |E_{01}\rangle, |E_{11}\rangle\} = \left\{ \frac{|e\rangle(|g\rangle \pm |f\rangle)}{\sqrt{2}}, \frac{(|g\rangle \pm |f\rangle)|e\rangle}{\sqrt{2}} \right\}$  have 0 energy.

The error correction cycle works as follows (take  $|L_0\rangle$  as an example): Suppose  $Q_1$  lost one photon and the system becomes the error state  $|E_{00}\rangle = \frac{|e\rangle(|g\rangle - |f\rangle)}{\sqrt{2}}$ . Under the QR1 interactions, the oscillation  $|E_{00}00\rangle \leftrightarrow |L_010\rangle$  will be activated. Since  $R_1$  is very lossy, the photon excitation in the resonator will decay quickly, leading to the final steady state  $|L_000\rangle$ , which is exactly the original logical state. A similar process also applies for  $|L_1\rangle$ :  $|E_{10}00\rangle \leftrightarrow |L_110\rangle \rightarrow |L_100\rangle$  and for correcting single-photon loss error happened at  $Q_2$ . In total, the operation of VSLQ requires four always-on drives:  $|gf\rangle \leftrightarrow |fg\rangle$ ,  $|gg\rangle \leftrightarrow |ff\rangle$ , and two  $|e0\rangle \leftrightarrow |f1\rangle$  between each QR pairs. The VSLQ energy diagram in the rotating frame is shown in Fig. 3.1.

One important thing to notice in Fig. 3.1 is that the photon decayed from  $R_i$  is energy-independent of the logical state. This is extremely important to protect the logical superposition states, and any small energy deference will lead to a direct logical dephasing channel.

Fig. 3.2 shows one possible device and its circuit diagram to realize the two 4-photon

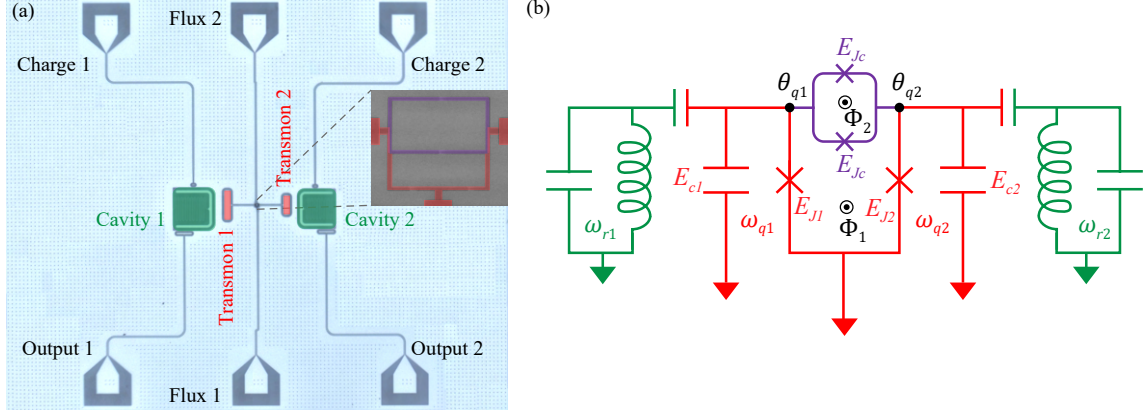


Figure 3.2: VSLQ device. (a) Device optical false-colored picture. The red and green elements are the transmons and readout resonators. The inset shows a scanning electron micrograph of the coupler loop (purple) and the two Josephson junctions for the qubits forming the main loop (red). The magnetic fluxes threading the main and coupler loop are denoted by  $\Phi_1$  and  $\Phi_2$ , respectively. (b) Equivalent circuit diagram.

processes between transmons. Two transmons (Shown in red) share the same ground and are inductively coupled through a bridged-SQUID loop. This forms two flux loops with threaded external flux  $\Phi_1$  (red, the main loop) and  $\Phi_2$  (purple, the coupler loop). Each transmon is capacitively coupled to a lossy resonator (Shown in green), which is also used as the readout. The two transmons share the same ground and are inductively coupled through a SQUID loop. The circuit Hamiltonian for the transmon and coupler part is [53]:

$$\begin{aligned}
 H_1 = & \sum_{i=1,2} \left( \omega_{qi} a_{qi}^\dagger a_{qi} + \frac{\alpha_i}{2} a_{qi}^\dagger a_{qi}^\dagger a_{qi} a_{qi} \right) \\
 & - E_{Jc} \cos(\theta_{q1} - \theta_{q2} + 2\pi \frac{\Phi_1}{\Phi_0}) + E_{Jc} \cos(\theta_{q1} - \theta_{q2} + 2\pi \frac{\Phi_1 + \Phi_2}{\Phi_0}) \quad (3.5)
 \end{aligned}$$

Here, we label the external flux threading the main loop (red) and coupler loop (purple) as  $\Phi_1$  and  $\Phi_2$ . The coupler junctions are assumed to be identical, and the Josephson energy is labeled  $E_{Jc}$ . To realize a pure 4-photon process, the VSLQ codewords operate at:

$$\begin{cases} \Phi_1 = \frac{\Phi_0}{4} - \varepsilon \sin(\omega_d t) \\ \Phi_2 = -\frac{\Phi_0}{2} + 2\varepsilon \sin(\omega_d t) \end{cases} \quad (3.6)$$

Plug Eq. 3.6 into Eq. 3.5, we have:

$$H_1 = \sum_{i=1,2} \left( \omega_{qi} a_{qi}^\dagger a_{qi} + \frac{\alpha_i}{2} a_{qi}^\dagger a_{qi}^\dagger a_{qi} a_{qi} \right) - 4\varepsilon E_{Jc} \sin(\omega_d t) \cos(\theta_{q1} - \theta_{q2}) \quad (3.7)$$

Under the leading order of the S-W transformation, the phase difference  $\theta_{q1} - \theta_{q2}$  between two transmon nodes can be approximated as:

$$\theta_{q1} - \theta_{q2} = \frac{1}{2} \left( \sqrt[4]{\frac{2E_{c1}}{E_{J1}}} a_{q1}^\dagger e^{i(\omega_{q1} + \alpha_1/2)t} - \sqrt[4]{\frac{2E_{c2}}{E_{J2}}} a_{q2}^\dagger e^{i(\omega_{q2} + \alpha_2/2)t} \right) \quad (3.8)$$

Plug Eq. 3.8 into Eq. 3.7, keep the fourth-order term in the cos interactions, we can activate the 4-photon process by choosing different flux modulation frequencies  $\omega_d$  and keep the time-independent terms:

$$\begin{cases} \omega_d = 2\omega_{q1} + 2\omega_{q2} + \alpha_1 + \alpha_2 & : -\frac{\varepsilon E_{Jc} \sqrt{E_{c1} E_{c2}}}{E_{J1} E_{J2}} (a_{q1}^\dagger a_{q1}^\dagger a_{q2}^\dagger a_{q2}^\dagger + h.c.) \\ \omega_d = 2\omega_{q1} - 2\omega_{q2} + \alpha_1 - \alpha_2 & : -\frac{\varepsilon E_{Jc} \sqrt{E_{c1} E_{c2}}}{E_{J1} E_{J2}} (a_{q1}^\dagger a_{q1}^\dagger a_{q2} a_{q2} + h.c.) \end{cases} \quad (3.9)$$

Eq. 3.9 indicates that one can realize the two sidebands  $|gf\rangle \leftrightarrow |fg\rangle$  and  $|gg\rangle \leftrightarrow |ff\rangle$  directly with this special ‘‘VSLQ’’ coupler. More importantly, the sideband rates for both processes are linearly proportional to the modulation amplitude  $\varepsilon$ , which will theoretically provide very fast 4-photon interactions.

However, the following three problems prevented the device from experimentally realizing the VSLQ code:

First, there is a strong stray  $ZZ$  coupling between two transmons.  $Q_1$ 's frequency depends on the  $Q_2$ 's state, and a minimum  $ZZ$  of 8.5 MHz (dependent on the actual design parameters) is measured in our experiments. The VSLQ logical state will have  $T_2 \sim 1/ZZ$  after AQEC, which is much worse than the bare transmon coherence. In Fig. 3.2(b), we neglect the stray capacitance between two transmon capacitive pads. The stray capacitance dominantly comes from the SQUID coupler junctions, which means additional circuit elements are necessary to suppress/mitigate the  $ZZ$ .

Second, the flux line design must be optimized to avoid stray capacitive coupling to the coupler [50, 56] and achieve pure flux modulation at high frequency. In our system, the RF flux modulation frequency for the  $|gg\rangle \leftrightarrow |ff\rangle$  transition is around 15 GHz when  $\omega_{qi} \sim 4$  GHz. The strength of the flux line's stray capacitive coupling to the coupler generally increases quadratically as  $\omega_d$  increases. Therefore, optimizing the flux line geometry is challenging and fab-sensitive, making the current device less ideal for experimental implementation.

Finally, the "VSLQ" point is parked at the coupler SQUID's anti-sweet spot where both transmons have the lowest  $T_2$ . Although the dominant dephasing channel is low-frequency and can be mitigated with echo techniques, characterizing a system with short  $T_2$  remains experimentally challenging. It is crucial that the QQ sideband rate  $W$  is sufficiently large to surpass the logical coherence overhead.

### 3.2 Split into Virtual Raman Processes: The Star Code

In Section. 3.1, we discuss the VSLQ codewords and its experimental challenges. Our AQEC demonstration aims to generate a Floquet system such that the logical state manifold has an energy gap with the error state manifold. Engineering the direct 4-photon QQ sidebands is a mathematically simple solution, but there are more possible solutions: Each 4-photon process can be split into two two-photon processes for simple experimental demonstration.

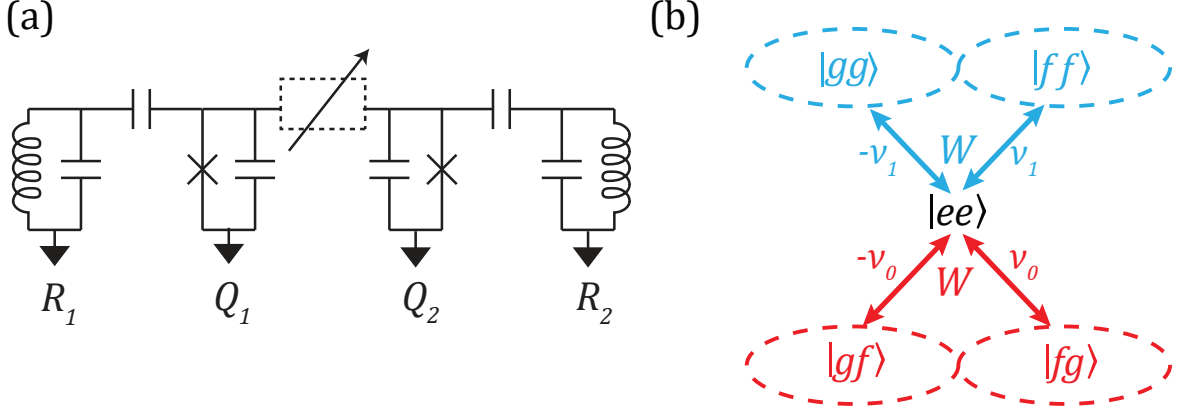


Figure 3.3: Star code protocol. (a) An example of hardware layout. Two transmons are individually coupled to two resonators dispersively. The dashed box between the two transmons represents any tunable coupling element that can provide sufficiently strong QQ red and blue sideband interactions. (b) Four QQ sideband mixing configurations in the logical static frame. All sidebands are applied with an equal rate  $W$  and specific detuning choices ( $\pm\nu_{0/1}$ ) to construct the logical manifold.

This leads to our new AQEC code, the Star code [49].

Similar to the VSLQ code, the Star code encodes a single logical qubit using the first three levels of two transmons. The logical manifold  $\{|L_0\rangle, |L_1\rangle\}$  in the Star code is defined as:  $|L_0\rangle = (|gf\rangle - |fg\rangle)/\sqrt{2}$  and  $|L_1\rangle = (|gg\rangle - |ff\rangle)/\sqrt{2}$ . The Star code aims to correct single-photon loss and suppress low-frequency dephasing. Up to an irrelevant relative phase difference, these are the same codewords in VSLQ.

Following the labeling scheme in Section. 3.1, we consider a two-transmon-two-resonator system shown in Fig. 3.3(a). The two transmon  $Q_1$  and  $Q_2$  have frequencies  $\omega_{qj}$  and anharmonicities  $\alpha_j$ , which interact with each other through a tunable coupling element [50]. Two lossy resonators  $R_1$  and  $R_2$  (frequency  $\omega_{rj}$ ) are capacitively coupled to each transmon, serving as lossy reservoirs and readouts. We assume both resonators are cold enough; only the first two levels are included in our discussion.

The state for each QR pair is labeled as  $|q, n\rangle \in \{|g\rangle, |e\rangle, |f\rangle\} \otimes \{|0\rangle, |1\rangle\}$ . We assume that the external drives through the tunable coupling element can independently modulate

two-photon QQ and QR sidebands. The lab frame Hamiltonian of the full system is

$$H_{\text{lab}} = \sum_{j=1}^2 \left( \omega_{qj} a_{qj}^\dagger a_{qj} + \frac{\alpha_j}{2} a_{qj}^\dagger a_{qj}^\dagger a_{qj} a_{qj} + \omega_{rj} a_{rj}^\dagger a_{rj} \right) + H_{QQ} + \sum_{j=1}^2 H_{QRj}, \quad (3.10)$$

$$H_{QQ} = A_{QQ}(t) \left( a_{q1}^\dagger + a_{q1} \right) \left( a_{q2}^\dagger + a_{q2} \right), \quad (3.11)$$

$$H_{QRj} = A_{QRj}(t) \left( a_{qj}^\dagger + a_{qj} \right) \left( a_{rj}^\dagger + a_{rj} \right), \quad (3.12)$$

$$\begin{aligned} A_{QQ}(t) &= \frac{W}{\sqrt{2}} \cos \left( (\omega_{q2} - \omega_{q1} - \alpha_1 - \nu_0) t \right) \\ &\quad + \frac{W}{\sqrt{2}} \cos \left( (\omega_{q2} - \omega_{q1} + \alpha_2 + \nu_0) t \right) \\ &\quad + W \cos \left( (\omega_{q1} + \omega_{q2} - \nu_1) t \right) \\ &\quad + \frac{W}{2} \cos \left( (\omega_{q1} + \omega_{q2} + \alpha_1 + \alpha_2 + \nu_1) t \right), \end{aligned} \quad (3.13)$$

$$A_{QRj}(t) = \frac{\Omega_j}{\sqrt{2}} \cos \left( (\omega_{qj} + \omega_{rj} + \alpha_j) t \right). \quad (3.14)$$

In Eq. 3.10, the QQ interactions  $H_{QQ}$  contains 4 detuned two-photon processes:  $|ee\rangle \leftrightarrow \{|gf\rangle, |fg\rangle, |gg\rangle, |ff\rangle\}$  with modulation amplitudes  $\{W/\sqrt{2}, W/\sqrt{2}, W, W/2\}$  and frequency detunings  $\{\pm\nu_0, \pm\nu_1\}$ . The modulation amplitudes are chosen to achieve the same sideband rate for 4 QQ interactions. The two QR sidebands generate the on-resonance transition  $|e0\rangle \leftrightarrow |f1\rangle$  between each transmon-resonator pair. We keep  $W \gg \Omega_j$  such that QR sidebands are treated as system perturbation. The topology of all 4 QQ sidebands  $\{|ee\rangle\} \leftrightarrow \{|gf\rangle, |fg\rangle, |gg\rangle, |ff\rangle\}$  used in the Star Code is equivalent to a ‘‘four-pointed star’’ in a two-qutrit level diagram (see Fig. 3.3(b)), which gives the Star Code its name [50].

We perform several rotating frame transformations and restrict the Hilbert space dimension to  $3 \times 3 \times 2 \times 2$  ( $Q_1 Q_2 R_1 R_2$ ) for simplicity. We first define a series of transformation

operators

$$U_1(t) = \exp \left[ i \sum_{j=1,2} \left( \omega_{qj} + \frac{\alpha_j}{2} \right) a_{qj}^\dagger a_{qj} t \right], \quad (3.15)$$

$$U_2(t) = \exp \left[ -i \frac{\alpha_1 + \alpha_2}{2} P_{ee} t \right], \quad (3.16)$$

$$U_3(t) = \exp \left[ i \nu_0 (P_{gf} + P_{fg} + P_{ge} + P_{eg}) t \right], \quad (3.17)$$

$$U_4(t) = \exp \left[ i \nu_1 (P_{gg} + P_{ff} + P_{ef} + P_{fe}) t \right], \quad (3.18)$$

$$U_5(t) = \exp \left[ i \sum_{j=1,2} \left( \omega_{rj} + \frac{\alpha_j}{2} \right) a_{rj}^\dagger a_{rj} t \right]. \quad (3.19)$$

Here we define projectors  $P_{ab} = |ab\rangle \langle ab| \otimes I_2 \otimes I_2$ , where  $I_2$  is a  $2 \times 2$  identity matrix.

There are two useful rotating frames for understanding the Star code: The logical static frame  $H_{\text{static}}$  (with transformation unitary  $U_a = U_5 U_2 U_1$ ) and the fully rotated frame  $H_{\text{rot}}$  (with transformation unitary  $U_b = U_5 U_4 U_3 U_2 U_1$ ). In the logical static frame, all logical states are time-independent and take simple explicit forms, while in the fully rotated frame, simulation is faster.

In the logical static frame  $H_{\text{static}}$ , if the two frequency detunings  $\nu_0$  and  $\nu_1$  are unequal, there will be two time-independent zero-energy eigenstates  $\{|L_0\rangle, |L_1\rangle\}$  that form the static logical manifold. Applying rotating wave approximation (RWA) to  $H_{QRj}$ , the full system

Hamiltonian becomes

$$\begin{aligned}
H_{\text{static}} &= U_a H_{\text{lab}} U_a^\dagger + i\dot{U}_a U_a^\dagger \\
&= \tilde{H}_{QQ} + \tilde{H}_{QR1} + \tilde{H}_{QR2} - \sum_{j=1,2} \frac{\alpha_j}{2} a_{rj}^\dagger a_{rj} \\
&\quad - \frac{\alpha_1}{2} (P_{eg} + P_{ef}) - \frac{\alpha_2}{2} (P_{ge} + P_{fe}), \tag{3.20}
\end{aligned}$$

$$\begin{aligned}
\tilde{H}_{QQ} &= \frac{W}{2} \left[ (|gf\rangle \langle ee| + |fg\rangle \langle ee|) e^{-it\nu_0} \right. \\
&\quad \left. + (|gg\rangle \langle ee| + |ff\rangle \langle ee|) e^{-it\nu_1} \right] + h.c., \tag{3.21}
\end{aligned}$$

$$\tilde{H}_{QR1} = \frac{\Omega_1}{2} (|eg\rangle \langle fg| + |ef\rangle \langle ff|) \otimes |0\rangle \langle 1| \otimes I_2 + h.c., \tag{3.22}$$

$$\tilde{H}_{QR2} = \frac{\Omega_2}{2} (|ge\rangle \langle gf| + |fe\rangle \langle ff|) \otimes I_2 \otimes |0\rangle \langle 1| + h.c. \tag{3.23}$$

In the fully rotated frame, the system Hamiltonian  $H_{\text{rot}}$  is given by

$$\begin{aligned}
H_{\text{rot}} &= U_b H_{\text{lab}} U_b^\dagger + i\dot{U}_b U_b^\dagger \\
&= -\frac{\alpha_1}{2} (P_{eg} + P_{ef}) - \frac{\alpha_2}{2} (P_{ge} + P_{fe}) \\
&\quad - \nu_0 (P_{gf} + P_{fg} + P_{ge} + P_{eg}) \\
&\quad - \nu_1 (P_{gg} + P_{ff} + P_{ef} + P_{fe}) \\
&\quad + H'_{QQ} - \sum_{j=1,2} \left( \frac{\alpha_j}{2} a_{rj}^\dagger a_{rj} + \tilde{H}_{QRj} \right), \tag{3.24}
\end{aligned}$$

$$\begin{aligned}
H'_{QQ} &= \frac{W}{2} (|ee\rangle \langle gf| + |ee\rangle \langle fg| \\
&\quad + |ee\rangle \langle gg| + |ee\rangle \langle ff| + h.c.) \otimes I_2 \otimes I_2. \tag{3.25}
\end{aligned}$$

Assuming the following hierarchy of rates:  $W \gg \Omega_j \sim \kappa_j \gg \gamma_j$  which are generic features of AQEC schemes. AQEC performance is generally insensitive to the fluctuations in  $\omega_j$  and  $\kappa_j$ . In the following discussion, we assume  $\Omega_j = \Omega$ ,  $\kappa_j = \kappa$ ,  $\gamma_j = \gamma$  and  $\nu_0 = -\nu_1 = \nu$  for simplicity.

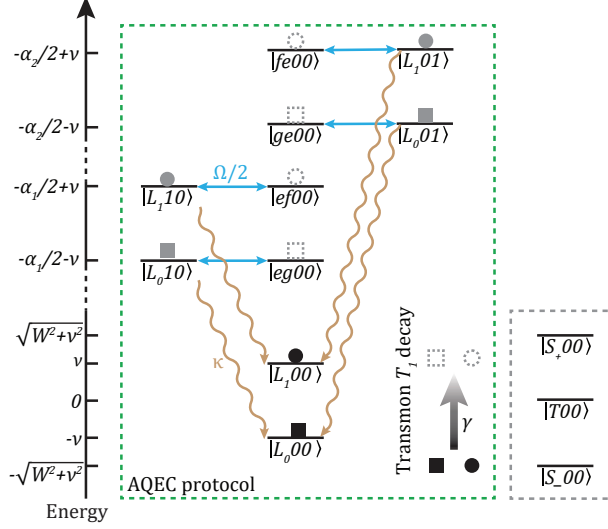


Figure 3.4: Star Code energy diagram in the rotating frame. The green dashed box covers the logical states and error states involved in the AQEC protocol, and the grey dashed box includes the other stray eigenstates that have suppressed population transfer by the energy gap. Error states from single-photon loss are restored to the parent logical states through individual correction paths. The QR sidebands (rate  $\Omega/2$ ), the resonators' photon decay (rate  $\kappa$ ), and the transmon  $T_1$  decay (rate  $\gamma$ ) are shown in the blue, brown, and black arrows respectively.

By treating QR sidebands as perturbations, the energy spectrum for  $H_{\text{rot}}$  is plotted in Fig. 3.4. The eigenstates can be grouped into three sets:  $\{|L_0\rangle, |L_1\rangle\}$ ,  $\{|eg\rangle, |ge\rangle, |ef\rangle, |fe\rangle\}$ , and  $\{|T\rangle, |S_-\rangle, |S_+\rangle\}$ . The first set forms the logical space with eigenenergies  $\{-\nu, \nu\}$ . The second set contains the states originating from a single photon loss error. The third set is comprised of stray eigenstates (not normalized for brevity) that are suppressed by the frequency detuning choice  $\pm\nu$ ,

$$|T\rangle = |gg\rangle - |gf\rangle - \frac{2\nu}{W} |ee\rangle - |fg\rangle + |ff\rangle, \quad (3.26)$$

$$\begin{aligned} |S_{\pm}\rangle &= |gg\rangle + \frac{W^2}{W^2 + 2\nu^2 \pm 2\nu\sqrt{W^2 + \nu^2}} |gf\rangle \\ &\quad - \frac{2\left(\mp\nu + \sqrt{W^2 + \nu^2}\right)}{W} |ee\rangle \\ &\quad + \frac{W^2}{W^2 + 2\nu^2 \pm 2\nu\sqrt{W^2 + \nu^2}} |fg\rangle + |ff\rangle. \end{aligned} \quad (3.27)$$

Under the assumption of  $\nu \sim W$ , the stray eigenstates maintain sufficient energy gap from the logical states. The on-resonance QR sidebands continuously pump the error states after single-photon loss to the target logical states, with an extra photon excitation appearing in the corresponding resonator  $R_j$ . These excitations in the resonators decay quickly at a rate  $\kappa$  and recover the logical state.

From another point of view, the four detuned QQ sidebands effectively introduce the 4-photon interactions  $|gf\rangle\langle fg|$  and  $|gg\rangle\langle ff|$  to the system, with  $|L_0\rangle$  and  $|L_1\rangle$  being separately the dark state of each 4-photon sideband. Since all other states are separated from the logical manifold by  $O(W)$  energy differences, the four QQ sidebands induce a dynamical decoupling effect suppressing dephasing from low-frequency phase noise. The other bright states  $\{|T\rangle, |S_-\rangle, |S_+\rangle\}$  are separated from the codewords through the QQ sideband frequency detuning  $\{\nu_0, \nu_1\}$ , so that passive error correction does not mix the error states with them. Notice that the superposition state  $|L_x\rangle = (|L_0\rangle + |L_1\rangle)/\sqrt{2}$  in the frame of Eq. 3.24 will have a fast oscillating phase between logical basis. The energy shift to codewords comes simply from rotating frame choices and has no physical consequence.

The Star Code also suppresses the no-jump error [61] as the always-on two-qubit Hamiltonian  $H_{QQ}$  maintains the form of logical states. The suppression has the same scaling as the suppression of  $1/f$  dephasing noise, achieved through the dynamical decoupling effect.

### 3.3 Star Code Simulation

Next, we will discuss the theoretical lifetime improvement against single-photon loss error for the Star Code. We approximate the lifetime improvement semi-classically and verify its agreement using simulations. First, we consider the case of  $|L_0\rangle$  and ignore the population lost to the stray eigenstates under the QR sideband. The logical states' refilling rate  $\Gamma_R$  is a two-step process: (a) the QR sidebands that resonantly bring error states to the parent logical states and (b) the resonator photon decay process. Using Fermi's golden rule and assuming Lorentzian distribution of lossy resonators' energy [41, 39], we have:

$$\Gamma_R = \frac{\Omega^2 \kappa}{\kappa^2 + \Omega^2}. \quad (3.28)$$

We further label the population of  $|L_000\rangle$  and  $|eg00\rangle$  (also for  $|ge00\rangle$ ) at time  $t$  as  $P_L(t)$  and  $P_E(t)$ . Due to the choice of symmetric parameters, the population of error states  $|eg00\rangle$  and  $|ge00\rangle$  are also the same. Assuming the system started with  $|L_000\rangle$  at time  $t = 0$ , we can express the evolution using the following differential equations:

$$\left\{ \begin{array}{l} \frac{dP_L(t)}{dt} = -2\gamma P_L(t) + 2\Gamma_R P_E(t), \\ \frac{dP_E(t)}{dt} = \gamma P_L(t) - (\gamma + \Gamma_R) P_E(t), \\ P_L(0) = 1, \\ P_E(0) = 0. \end{array} \right. \quad (3.29)$$

The solution of  $P_L(t)$  has two parts, a fast exponential decay term with a small weight

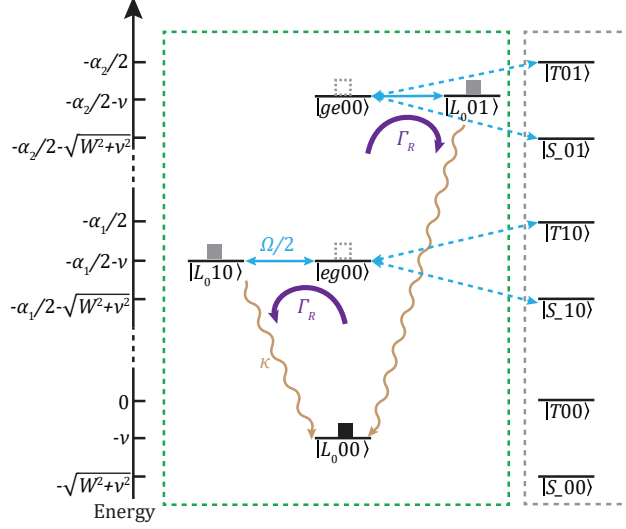


Figure 3.5: Error correction cycle for  $|L_0\rangle$ . The effective  $|L_0\rangle$  refilling rate  $\Gamma_R$  is shown in the purple arrow. A second photon loss can happen at rate  $\gamma$  before the completion of the refilling cycle. Population transfer to the grey dashed box is marked with blue dashed arrows, and the population transfer is suppressed by the energy difference  $O(\nu)$ .

and a dominant slow exponential decay term:

$$\left\{ \begin{array}{l} P_L(t) = \frac{-\gamma + \Gamma_R + \Delta}{2\Delta} \exp(t(\Delta - 3\gamma - \Gamma_R)/2) \\ \quad + \frac{\gamma - \Gamma_R + \Delta}{2\Delta} \exp(t(-\Delta - 3\gamma - \Gamma_R)/2) \\ \quad \approx (1 - 2\gamma/\Gamma_R) \exp\left(-\frac{2\gamma^2 t}{\Gamma_R + 3\gamma}\right), \\ \Delta = \sqrt{\gamma^2 + 6\gamma\Gamma_R + \Gamma_R^2}. \end{array} \right. \quad (3.30)$$

Assuming  $\Gamma_R \gg \gamma$ , the slow decay term shows quadratic lifetime improvement, compared to the physical transmon decay rate  $\gamma$ .

Then we consider the stray eigenstates  $\{|S_-\rangle, |T\rangle, |S_+\rangle\}$ . As shown in Fig. 3.5, the population transfer from the error states to the stray eigenstates is also a two-step process. By keeping the closest two eigenstates  $|S_-\rangle$  and  $|T\rangle$  in terms of energy, the refilling rates

$\{\Gamma_S, \Gamma_T\}$  are given by

$$\begin{cases} \Gamma_S = \frac{\kappa\Omega^2 k_s}{4(-\nu + \sqrt{W^2 + \nu^2})^2 + \kappa^2 + \Omega^2 k_s}, \\ \Gamma_T = \frac{\kappa\Omega^2 / (1 + \frac{\nu^2}{W^2})}{16\nu^2 + 4\kappa^2 + \Omega^2 / (1 + \frac{\nu^2}{W^2})}, \\ k_s = (\langle S_- | fg \rangle)^2. \end{cases} \quad (3.31)$$

Again, assuming the initial state is  $|L_0 00\rangle$  and treating population to  $\{|S_-\rangle, |T\rangle\}$  as an uncorrectable logical coherence loss, we have the following equations of motion:

$$\begin{cases} \frac{dP_L(t)}{dt} = -2\gamma P_L(t) + 2\Gamma_R P_E(t), \\ \frac{dP_E(t)}{dt} = \gamma P_L(t) - (\gamma + \Gamma_R + \Gamma_S + \Gamma_T) P_E(t), \\ P_L(0) = 1, \\ P_E(0) = 0. \end{cases} \quad (3.32)$$

Given  $\Gamma_R \gg \gamma, \Gamma_S, \Gamma_T$ , the slow decay rate in  $P_L(t)$  is

$$\Gamma_{L0} \sim \frac{2\gamma(\gamma + \Gamma_S + \Gamma_T)}{3\gamma + \Gamma_R + \Gamma_S + \Gamma_T}. \quad (3.33)$$

The slow decay rate for  $|L_1\rangle$  can be derived similarly

$$\Gamma_{L1} \sim \frac{2\gamma(3\gamma + \Gamma_S + \Gamma_T)}{5\gamma + \Gamma_R + \Gamma_S + \Gamma_T}. \quad (3.34)$$

Note that, for the realistic parameter ranges considered in this work,  $\Gamma_S$  and  $\Gamma_T$  will be much smaller than  $\gamma$  and contribute negligibly in determining the logical decay rates, which still show quadratic improvement compared to bare transmons' relaxation rates.

Using Eq. 3.31, 3.33 and 3.34, one can verify that larger QQ sideband rate  $W$  and detunings  $\nu$  will provide better energy isolation, leading to a higher logical states' lifetime. The ratio  $\Gamma_{L1}/\Gamma_{L0} \sim 3$  indicates that the logical qubit has approximately 3 times faster

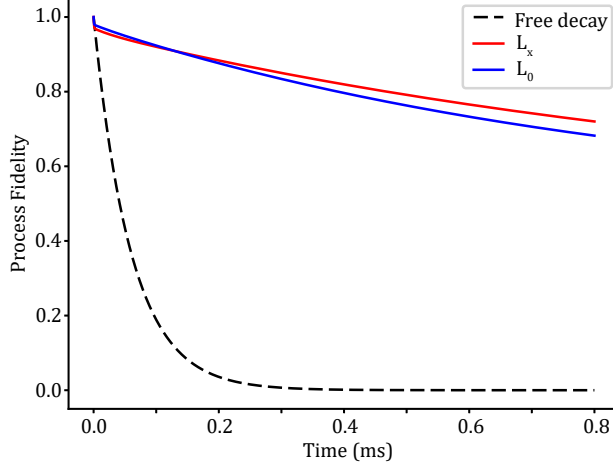


Figure 3.6: Simulated logical states' lifetime and physical qubit lifetime. Parameter used in the simulation:  $\{\alpha_1, \alpha_2, W, \nu_0, \nu_1, \Omega, \kappa\} = \{-160, -260, 10, 5.77, -5.77, 0.71, 0.5\}$  MHz,  $T_1 = 60 \mu\text{s}$ .

decay rate than the excitation rate, as the average photon number of  $a|L_1\rangle$  (error state) is three times larger than that of  $a|L_0\rangle$ .

The dominant logical error channel is the double-photon loss event. Since  $\langle L_1|a_{q1}a_{q1}|L_0\rangle = 1/\sqrt{2}$ , double-photon loss flips  $|L_0\rangle$  into  $|L_1\rangle$  and vice versa. This shows that under photon-loss only error, the slow exponential decay will bring  $|L_0\rangle$  and  $|L_1\rangle$  into each other. Therefore, the depolarization rate  $\Gamma_Z$  for the logical state is  $\Gamma_Z = \Gamma_{L_0} + \Gamma_{L_1}$ . For the transversal dephasing rate  $\Gamma_X$ , extra protection comes from the code structure. When a double-photon loss event happens on the same physical qubit (with 50% chance), the state obtains 50% overlap with  $|L_x\rangle$ . Therefore, for a quarter of the double-photon loss events,  $|L_x\rangle$  experiences no coherence loss, and the lifetime for  $|L_x\rangle$  is  $T_X = 4T_Z/3$ . For both  $T_Z$  and  $T_X$ , the lifetime improvement is quadratic given  $\Gamma_S + \Gamma_T \ll \gamma$ .

We perform rotating-frame simulations to verify the lifetime improvements. Fig. 3.6 shows the simulated process fidelity for  $|L_x\rangle$ ,  $|L_0\rangle$ , and physical qubit decay. Operators used for calculating the process fidelity for  $\{|L_0\rangle, |L_x\rangle\}$  are  $\{|L_0\rangle\langle L_0| - |L_1\rangle\langle L_1|, |L_x\rangle\langle L_x|\}$ . The logical lifetime is extracted by fitting the exponential decay constant of each logical state's process fidelity. Fig. 3.7(a) shows the lifetime of  $|L_x\rangle$  under different QQ sideband detuning

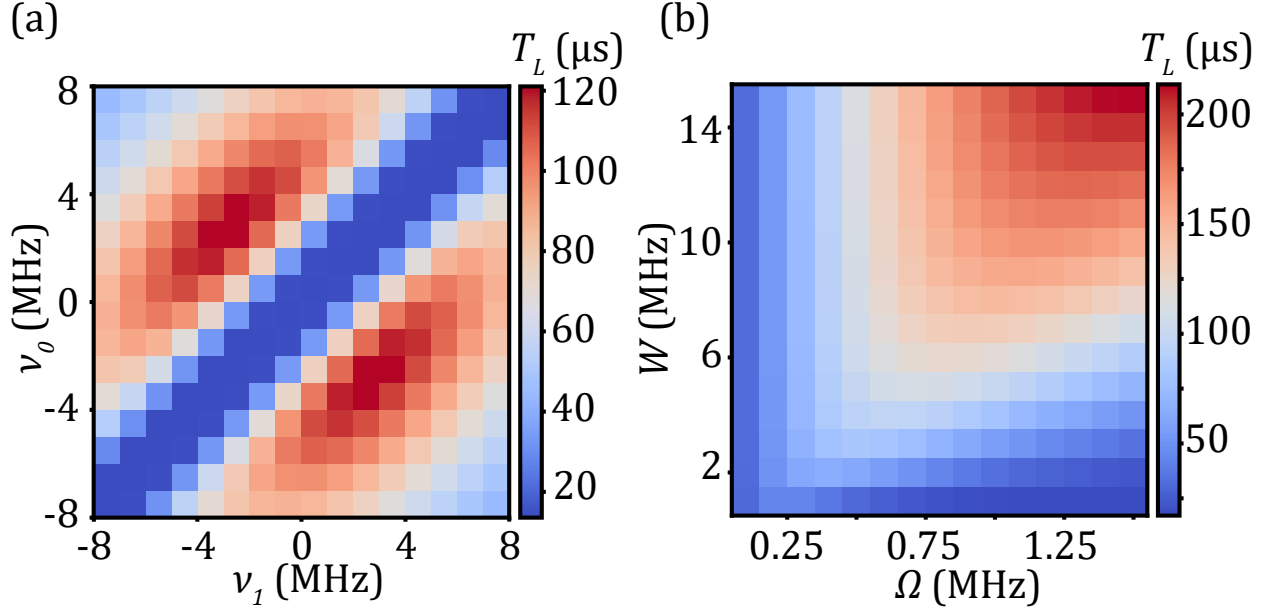


Figure 3.7: Logical lifetime ( $T_L$ ) as a function of detunings and sideband rates. Simulations are performed up to  $200\mu\text{s}$  with  $T_1 = 20\mu\text{s}$  for both transmons. The logical  $T_L$  are extracted by fitting the last  $180\mu\text{s}$  to an exponential decay profile. (a) 2D scan of QQ sideband detunings  $\nu_0$  and  $\nu_1$ . Other parameters used in the simulation:  $\{\alpha_1, \alpha_2, W, \Omega, \kappa\} = \{-160, -260, 5, 1, 0.5\}$  MHz. Optimal performance is obtained around  $\nu_0 = -\nu_1 = \pm W/\sqrt{3}$ . (b) 2D scan of QQ and QR sideband rates  $W$  and  $\Omega$ . Parameters are set to be  $\nu_0 = -\nu_1 = W/\sqrt{3}$ , and  $\Omega = \kappa$  for best AQEC performance. Simulations show significantly improved performance around  $\Omega = W/10$ .

combinations. We neglect short timescale behavior when extracting logical states' lifetimes. There is a low coherence strip along the diagonal region. This happens when  $\nu_0 = \nu_1$ , as  $\{|L_0\rangle, |L_1\rangle, |gg\rangle + |ff\rangle - |gf\rangle - |fg\rangle\}$  become degenerate eigenstates with non-orthogonal error states and violates the Knill-Laflamme condition. From Fig. 3.7(a), the maximum lifetime improvement region appears around  $\nu_0 = -\nu_1 = \pm W/\sqrt{3}$ . This can be intuitively understood as  $\{|S_-\rangle, |L_0\rangle, |T\rangle, |L_1\rangle, |S_+\rangle\}$  are evenly separated in energy (Fig. 3.4), thus providing close-to-optimal suppression of leakage to non-logical state population.

We fix the detuning relation  $\nu_0 = -\nu_1 = W/\sqrt{3}$  and sweep  $W, \Omega$  for  $|L_x\rangle$ 's lifetime. The results are plotted in Fig. 3.7(b). During the sweep, we choose  $\kappa = \Omega$ , where refilling rate  $\Gamma_R$  are optimal, and error correction performance becomes insensitive to small changes in

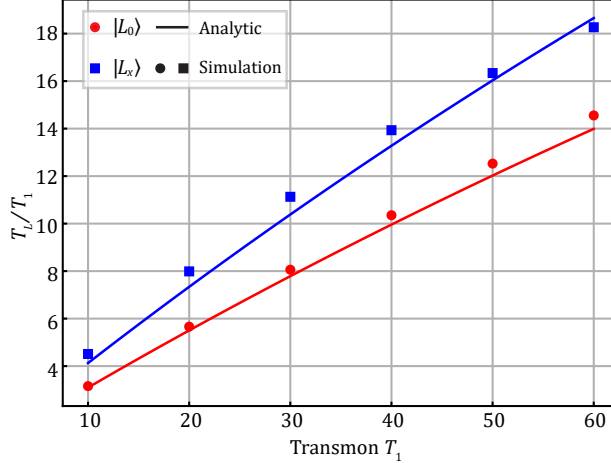


Figure 3.8: Logical lifetime improvement as a function of transmon  $T_1$  (considered identical for both transmons). Quadratic lifetime improvement (roughly linear improvement in the lifetime ratio) under AQEC is clearly seen in the plot. Logical  $T_L$  are extracted by fitting traces to the exponential decay curve  $A \exp(-t/T_L) + C$  (with  $A$  and  $C$  being free parameters), and the improvement ratio is  $T_L/T_1$ . Error bars (one standard deviation) for  $T_L$  are smaller than the marker size. Each simulation is run up to  $800 \mu\text{s}$ , and the short period is not included in the fitting. Other parameters used in the simulation are  $\{\alpha_1, \alpha_2, W, \nu_0, \nu_1, \Omega, \kappa\} = \{-160, -260, 10, 5.77, -5.77, 0.71, 0.5\}$  MHz. The analytic expression (solid lines) matches the simulation result. The depolarization lifetime of  $|L_1\rangle$  is almost the same as  $|L_0\rangle$  in simulation. All simulated logical lifetimes here are above the break-even point.

$\kappa$ . In practice,  $W = 10$  MHz and  $\Omega = 1$  MHz can be achieved in modern devices with some optimization [12, 50, 54]. Since larger  $W$  is more difficult to achieve in the system, given maximum  $W$ , optimal performance appears along the diagonals, where  $\Omega$  is roughly an order of magnitude smaller than  $W$ . Finally, we sweep  $T_1$  of the transmons and show the ratio of logical to physical lifetime in Fig. 3.8. The quadratic improvement in logical states' lifetime is clearly visible, and the data matches the analytic expression pretty well.

We note that the logical lifetime limit from other error channels (e.g.,  $1/f$  noise-induced dephasing and comparatively rare random photon addition due to finite temperature) in the Star code protocol is the same as in the original VSLQ proposal [37] because the AQEC process is the same except for a different Hamiltonian construction. The dephasing noise is coupled to a single qutrit  $Z$  operator [39], and the expectation value for this operator is

always 0 for all logical states. Therefore, the only impact of the dephasing noise comes from the transition to other states. However, this transition requires finite energy because of the always-on  $H'_{QQ}$ . The suppression process becomes equivalent to sampling  $1/f$  noise spectrum at a higher frequency, the same as the dynamical decoupling effect in the VSLQ cases. Another possible error channel is the leakage error. To prevent leakage to higher transmon energy levels, the two transmons are chosen to have large but different anharmonicities  $\alpha_j$ . This difference suppresses blue sideband transitions such as  $|gf\rangle\langle eh|$  and red sideband transitions such as  $|fe\rangle\langle hg|$  that populates  $|h\rangle$  level. Practically, the leakage outside the codespace is negligible for the range of parameters considered in simulations.

### 3.4 Coherence Limits from non-ideal Parameters

In this section, we will discuss the sensitivity of Star Code logical coherence to extra interactions that appeared in the Hamiltonian.

The  $ZZ$  interactions between transmons (Q) and readout resonators (R) are needed to distinguish the transmon state. While Star Code only requires the  $XX$  interactions between QR, the presence of QR dispersive coupling  $\chi$  helps calibrate the system. Figure 3.9 shows the simulated lifetimes for logical states  $|L_0\rangle$ ,  $|L_1\rangle$ , and  $|L_x\rangle$  in the presence of QR  $ZZ$  coupling obtained from solving the master equation. The logical state lifetime is weakly reduced in the low  $\chi$  regime. This is because the photon decay from either resonator will have different frequencies depending on the coupled transmon being in  $|g\rangle$  or  $|f\rangle$ . Such a resonator-induced dephasing does not introduce a logical dephasing error but only distorts the form of  $|L_0\rangle$  and  $|L_1\rangle$ . This noise has a Lorentzian spectrum that decays in frequency. When the QQ sideband rate  $W$  is much larger than  $\chi$ , the resonator-induced dephasing is suppressed strongly as the  $1/f$  dephasing noise. Therefore, in Fig. 3.9, the logical  $T_1$  is insensitive to small  $\chi$ .

Photon excitation in the readout resonators is detrimental to the Star Code. Suppose

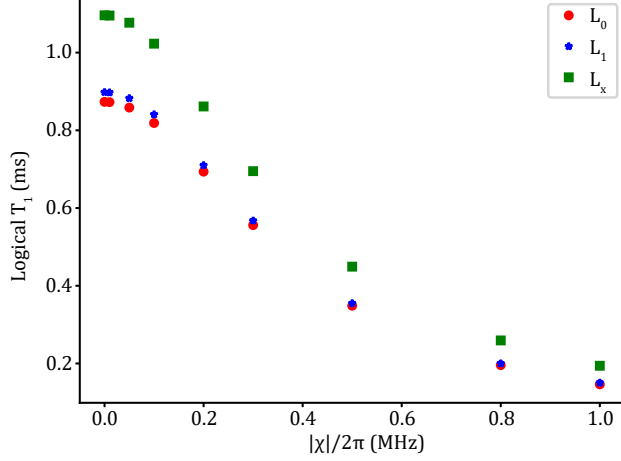


Figure 3.9: Simulated logical states' lifetime with qubit-resonator dispersive coupling  $\chi$ . Simulation parameters:  $\{\alpha_1, \alpha_2, W, \nu_0, \nu_1, \Omega, \kappa\} = \{-160, -260, 10, 5.77, -5.77, 0.71, 0.5\}$  MHz,  $T_1 = 60 \mu\text{s}$ .

$R_1$  excites a photon when the logical state is  $|L_0\rangle$ , the QR sideband  $|L_010\rangle \leftrightarrow |eg00\rangle$  will be activated and convert the logical state into the error state. This becomes a potential logical error unless the error state is flipped back before the second photon loss from the error state happens. In the real experiment, one should increase the readout frequency and thermalize the sample better for fewer photon excitation events.

The  $ZZ$  interactions between two transmons dephase the logical superposition state. Among all the  $ZZ$ s between two qutrits,  $ZZ_{ff1} = E_{|ff\rangle} - E_{|ef\rangle} - (E_{|fg\rangle} - E_{|eg\rangle})$  and  $ZZ_{ff2} = E_{|ff\rangle} - E_{|ef\rangle} - (E_{|gf\rangle} - E_{|ge\rangle})$  will cause the logical state dephasing, as a random phase between  $|L_0\rangle$  and  $|L_1\rangle$  will accumulate, which is proportional to the product of time error is corrected and  $ZZ_{ffj}$ . Longer transmon  $T_1$  and faster error correction rate (increasing QR sideband rate  $\Omega$ ) help mitigate such dephasing channel, and the cancellation requires a simultaneous cancellation of  $ZZ_{ff1}$  and  $ZZ_{ff2}$  when all QQ sidebands are on. This is achievable by adding extra detuned drives, such as the scheme discussed in Ref. [66] and Ref. [63].

The Star Code is insensitive to the small fluctuation in the QR sideband rate  $\Omega_j$  and does not require  $\Omega_1 = \Omega_2$  (used only for obtaining simpler analytic expressions in the main

text). Fluctuations in both QQ sideband rate  $W$  and detunings  $\nu_j$  are strongly suppressed as long as they are not comparable to the energy gap ( $O(W)$ ) between  $|L_0\rangle$  and  $|L_1\rangle$ .

### 3.5 Goals for Experimental Demonstration

As a summary of the theoretical results of the Star Code, we list the necessary requirements for the experimental AQEC demonstration:

(1) Two coupled anharmonic systems A and B (annihilation operators labeled as  $a$  and  $b$  separately) that can simultaneously engineer both beam-splitter ( $a^\dagger b + ab^\dagger$ ) and squeezing ( $ab + a^\dagger b^\dagger$ ) interactions.

(2) The  $ZZ_{ff1}$  and  $ZZ_{ff2}$  (See definitions in Section. 3.4) between A and B can be fully canceled.

(3) Both A and B have no significant photon excitation or white-noise dephasing channel.

(4) Frequency-selective two-photon process that simultaneously adds photons to the lossy resonator and its coupled anharmonic system.

(5) A and B both have good coherence ( $T_1$  and  $T_2$ ).

In our experiments, we decided to engineer an inductive tunable coupler between two transmons. Other superconducting qubits, such as Fluxonium, are also possible candidates for future study.

# CHAPTER 4

## TOWARDS AUTONOMOUS QUANTUM ERROR CORRECTION

This chapter will experimentally demonstrate a tunable coupler design between two transmons that meets the requirements listed in Section. 3.5. In Section. 4.1, we will detail the coupler design, circuit quantization, and characterization of various QQ and QR sidebands. Section. 4.2 will explore how the decent transmon coherence and native two-qutrit interactions enable the implementation of several two-qutrit quantum algorithms on this processor. Finally, in Section. 4.3, we will demonstrate programmable stabilization using the QQ and QR sidebands, showing that our Dissipative Floquet system is accurately modeled for a sufficiently long time for AQEC demonstration.

We have two chips of similar design labeled ‘Algorithm’ and ‘AQEC’ for our experiments with slightly different parameters. “Algorithm” is used for demonstrating two-qutrit algorithm experiments discussed in Section. 4.2, and ‘AQEC’ is for stabilization and Star Code experiments discussed in Section. 4.3 and Chapter 5. The circuit parameters for both chips are explicitly listed in the tables.

### 4.1 Two inductively coupled transmons

Fig. 4.1 shows our device of two inductively coupled transmon [12, 48, 50]. The key component is the inductive coupler based on the design in Ref. [55] that enables the realization of fast parametric interactions. Two transmons  $Q_1$  and  $Q_2$  serve as the qutrits and share a common path to ground. This path is interrupted by a Superconducting Quantum Interference Device (SQUID) loop. The SQUID functions as a tunable inductor with external DC and RF magnetic fields threaded to activate the QQ sidebands. Each transmon is ca-

---

Parts of this section have been published in Ref. [50]

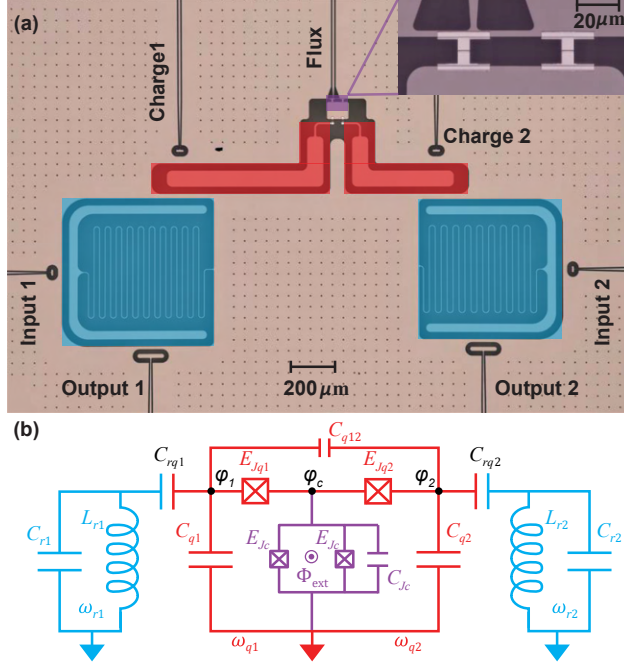


Figure 4.1: The device. (a) False-colored optical image. Two transmons (red) are inductively connected through a SQUID loop (purple, inset shows zoomed-in image). An on-chip flux line is coupled to the SQUID to activate QQ sidebands through parametric RF flux modulation at the proper DC flux position. Each transmon is capacitively coupled to the readout resonator (blue). Single transmon pulses are sent through the resonator input lines. QR sidebands are applied through corresponding charge lines. (b) Circuit schematic diagram.

capacitively coupled to a lossy resonator serving both as the readout and cold reservoir. QR sidebands can be performed by sending a charge drive at the half transition frequency to the transmon [88].

Algorithm chip				AQEC chip			
Capacitance	(fF)	Junction $E_j$	(GHz)	Capacitance	(fF)	Junction $E_j$	(GHz)
$C_{q1}$	178.0	$E_{j1}$	13.6	$C_{q1}$	165.9	$E_{j1}$	12.4
$C_{q2}$	131.0	$E_{j2}$	13.3	$C_{q2}$	123.4	$E_{j2}$	12.1
$C_c$	193.6	$E_{jc}$	1140.0	$C_c$	178.3	$E_{jc}$	1106.0
$C_{q12}$	2.0			$C_{q12}$	2.0		

Table 4.1: Capacitances and Josephson energies used in the quantization. Capacitances are extracted through finite-element simulations in ANSYS Q3D, and Josephson energies are calculated from the room-temperature resistances of nominally identical test junctions on the same chip.

We first consider the Hamiltonian of the two transmons:

$$H_Q = \vec{n}^\top C_L^{-1} \vec{n} - E_{j1} \cos(\varphi_c - \varphi_1) - E_{j2} \cos(\varphi_2 - \varphi_c) - E_{jc} \cos\left(\pi \frac{\Phi_{\text{ext}}}{\Phi_0}\right) \cos(\varphi_c), \quad (4.1)$$

$$C_L = \begin{bmatrix} C_{q1} + C_{q12} & -C_{q12} & 0 \\ -C_{q12} & C_{q2} + C_{q12} & 0 \\ 0 & 0 & C_{q1} + C_{q2} + C_{qc} \end{bmatrix}, \quad (4.2)$$

$$\vec{n}^\top = (n_1, n_2, n_c), \quad [n_j, \varphi_j] = -i. \quad (4.3)$$

Here  $\vec{n}$  and  $\vec{\varphi}$  are the charge and phase variables and can be found through the Legendre transformation. Table 4.1 includes all coefficients used in the quantization. Then we extract the linear part of  $H_Q$  to obtain

$$H_0 = \vec{n}^\top C_L^{-1} \vec{n} + \frac{E_{j1}}{2} (\varphi_c - \varphi_1)^2 + \frac{E_{j2}}{2} (\varphi_2 - \varphi_c)^2 + \frac{E_{jc}}{2} \cos\left(\pi \frac{\Phi_{\text{ext}}}{\Phi_0}\right) \varphi_c^2. \quad (4.4)$$

Next, we rewrite the charge and phase variables in the dressed basis with the unitary transformation matrix  $U$  such that  $H_0$  is simultaneously diagonalized to find out the normal

modes,

$$H_0 = \sum_{j=1,2,c} \left( \tilde{C}_j \tilde{n}_j^2 + \tilde{D}_j \tilde{\varphi}_j^2 \right), \quad (4.5)$$

$$\vec{\tilde{n}} = (\tilde{n}_1, \tilde{n}_2, \tilde{n}_c)^\top = U^{-1} \vec{n}, \quad (4.6)$$

$$\vec{\tilde{\varphi}} = (\tilde{\varphi}_1, \tilde{\varphi}_2, \tilde{\varphi}_c)^\top = U^{-1} \vec{\varphi}, \quad (4.7)$$

$$U = \begin{bmatrix} U_{11} & U_{12} & U_{1c} \\ U_{21} & U_{22} & U_{2c} \\ U_{c1} & U_{c2} & U_{cc} \end{bmatrix}. \quad (4.8)$$

In the dressed basis, the nonlinear part is reintroduced in the Hamiltonian to get

$$\begin{aligned} H_Q &= \sum_{j=1,2,c} \left( \tilde{C}_j \tilde{n}_j^2 \right) \\ &\quad - E_{j1} \cos \left( \sum_{j=1,2,c} (U_{cj} \tilde{\varphi}_j - U_{1j} \tilde{\varphi}_j) \right) \\ &\quad - E_{j2} \cos \left( \sum_{j=1,2,c} (U_{2j} \tilde{\varphi}_j - U_{cj} \tilde{\varphi}_j) \right) \\ &\quad - E_{jc} \cos \left( \pi \frac{\Phi_{\text{ext}}}{\Phi_0} \right) \cos \left( \sum_{j=1,2,c} U_{cj} \tilde{\varphi}_j \right), \end{aligned} \quad (4.9)$$

with

$$\tilde{n}_j = \frac{i}{\sqrt{2}} \sqrt{\frac{\tilde{D}_j}{\tilde{C}_j}} (a_{qj}^\dagger - a_{qj}), \quad (4.10)$$

$$\tilde{\varphi}_j = \frac{1}{\sqrt{2}} \sqrt{\frac{\tilde{C}_j}{\tilde{D}_j}} (a_{qj}^\dagger + a_{qj}). \quad (4.11)$$

We use the scQubits package [14] to quantize the Hamiltonian. The comparison between numerical values and experimental data are shown in Fig. 4.2. When  $\Phi_{\text{ext}}$  is biased close

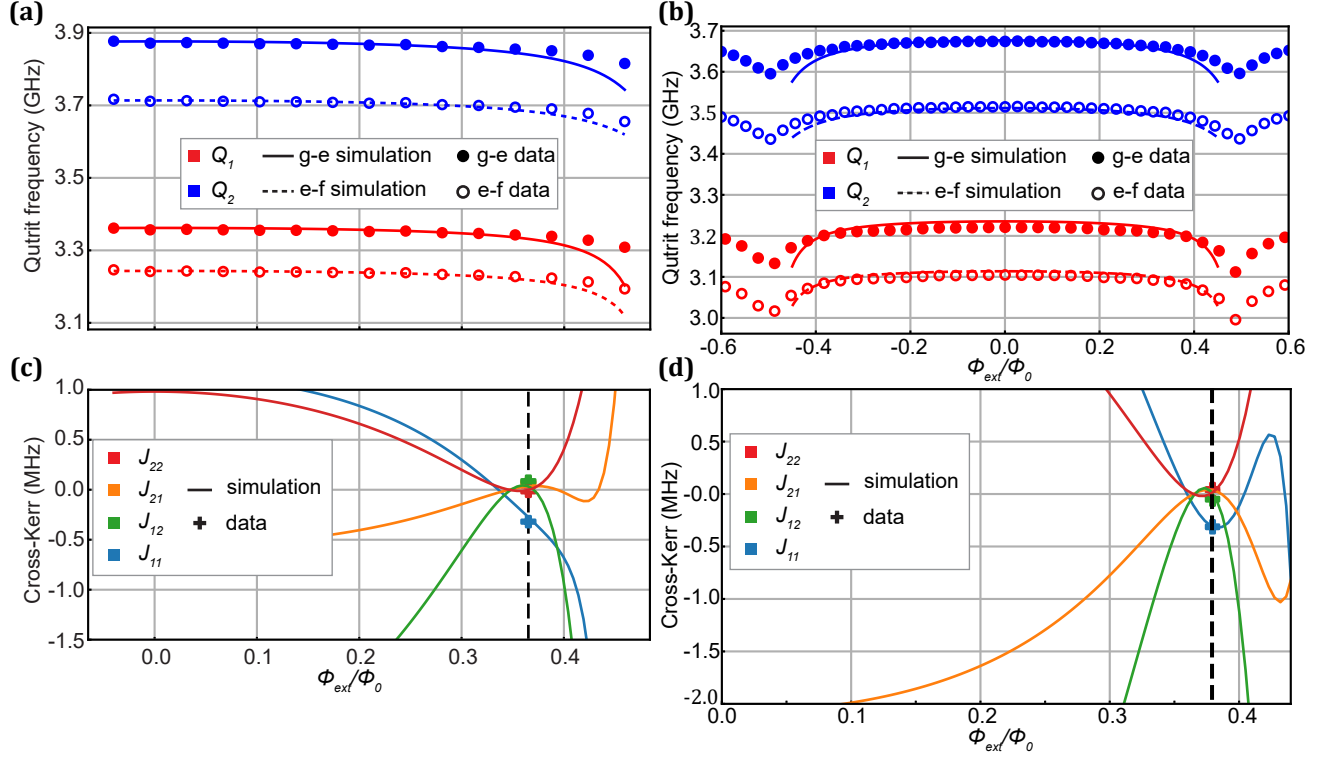


Figure 4.2: Circuit quantization results of  $H_Q$ . Comparison of (a) ‘Algorithm chip’ and (b) ‘AQEC chip’ transmon frequencies and (c) ‘Algorithm chip’ and (d) ‘AQEC chip’ cross-Kerr couplings between simulation and experiment.  $Q_1$  (red) and  $Q_2$ ’s (blue)  $|g\rangle \leftrightarrow |e\rangle$  and  $|e\rangle \leftrightarrow |f\rangle$  frequencies from numerical calculation and experiment are plotted as a function of  $\Phi_{\text{ext}}$ . Four inter-qutrit cross-Kerr coupling strengths,  $J_{11}$ ,  $J_{21}$ ,  $J_{12}$  and  $J_{22}$  are calculated, and experiment data are marked out on the Star code operating point (dashed line).

to  $\Phi_0/2$ , deviation appeared in numerics. This comes from the asymmetry of SQUID junctions’ resistances and parasitic SQUID loop inductance. This region of deviation is far from the experimental bias point. Around the DC flux position where the experiments are implemented (marked as the dashed line in Fig. 4.2 (c) and (d) ), there is a good agreement between simulated and experimental values for both transmons’ frequencies and cross-Kerr couplings. The transmon frequencies are insensitive to  $\Phi_{\text{ext}}$  when  $\Phi_{\text{ext}}$  is far away from  $\pi/2$ , ensuring a good Ramsey time for both transmons.

Relevant coherence parameters and frequencies at the operating point (coupler DC flux bias  $\Phi_{\text{DC}} = 0.185\Phi_0$  for ‘Algorithm’ chip and  $\Phi_{\text{DC}} = 0.3795\Phi_0$  for ‘AQEC’ chip) without external drives are listed in Table 4.2 and Table 4.3. The  $ZZ$  coupling (dispersive shifts)

$\Phi_{\text{DC}} = 0$		Algorithm chip			AQEC chip		
Transition	$T_1$ ( $\mu\text{s}$ )	$T_R$ ( $\mu\text{s}$ )	$T_{\text{echo}}$ ( $\mu\text{s}$ )	$T_1$ ( $\mu\text{s}$ )	$T_R$ ( $\mu\text{s}$ )	$T_{\text{echo}}$ ( $\mu\text{s}$ )	
$Q_1  e\rangle \rightarrow  g\rangle$	-	-	-	31.6	28.4	26.6	
$Q_2  e\rangle \rightarrow  g\rangle$	-	-	-	2.8	4.9	-	

Algorithm chip ( $\Phi_{\text{DC}} = 0.185\Phi_0$ )				AQEC chip ( $\Phi_{\text{DC}} = 0.3795\Phi_0$ )		
Transition	$T_1$ ( $\mu\text{s}$ )	$T_R$ ( $\mu\text{s}$ )	$T_{\text{echo}}$ ( $\mu\text{s}$ )	$T_1$ ( $\mu\text{s}$ )	$T_R$ ( $\mu\text{s}$ )	$T_{\text{echo}}$ ( $\mu\text{s}$ )
$Q_1  e\rangle \rightarrow  g\rangle$	47.9	4.5	-	24.3	15.2	24.6
$Q_2  e\rangle \rightarrow  g\rangle$	35.1	3.2	-	9.1	9.8	14.3
$Q_1  f\rangle \rightarrow  e\rangle$	21.7	2.0	-	27.1	16.7	29.3
$Q_2  f\rangle \rightarrow  e\rangle$	3.9	2.4	-	26.7	20.1	34.3
$R_1  1\rangle \rightarrow  0\rangle$	0.3			0.3		
$R_2  1\rangle \rightarrow  0\rangle$	0.3			0.3		

Table 4.2: Device coherence parameters at different DC flux points.  $Q_2$  has lower coherence at the zero flux point because of the presence of a two-level system (TLS).

between two-transmon energy levels are measured in the experiment through Ramsey fringe frequency difference, and the cross-Kerr couplings  $J_{11}$ ,  $J_{21}$ ,  $J_{12}$ ,  $J_{22}$  are calculated from those measurement results. We separately measure all 7  $ZZ$ s in the experiment through Ramsey frequency difference. The four independent  $J_{jk}$  are inferred from the experimentally measured seven cross-Kerr values: we choose the  $J_{jk}$  set that minimizes the Euclidean distance between the seven experimental and the theoretical  $ZZ$  values calculated from Eq. (4.12).

Parameter	Symbol	Algorithm chip	AQEC chip
		Value/ $2\pi$	
$Q_1$ ge frequency	$\omega_{q1}$	3.3494 GHz	3.2049 GHz
$Q_2$ ge frequency	$\omega_{q2}$	3.8310 GHz	3.6625 GHz
$Q_1$ anharmonicity	$\alpha_1$	-115.2 MHz	-116.4 MHz
$Q_2$ anharmonicity	$\alpha_2$	8 MHz	-159.6 MHz
$R_1$ frequency	$\omega_{r1}$	4.9602 GHz	4.9946 GHz
$R_2$ frequency	$\omega_{r2}$	5.4225 GHz	5.4505 GHz
$R_1$ dispersive shift	$\chi_1$	-	-180 kHz
$R_2$ dispersive shift	$\chi_2$	-	-330 kHz
$\left( E_{ ee\rangle} - E_{ ge\rangle} \right) - \left( E_{ eg\rangle} - E_{ gg\rangle} \right)$	$ZZ_{ge}$	-238 kHz	-261 kHz
$\left( E_{ fe\rangle} - E_{ ee\rangle} \right) - \left( E_{ fg\rangle} - E_{ eg\rangle} \right)$	$ZZ_{ef1}$	-148 kHz	-130 kHz
$\left( E_{ ef\rangle} - E_{ ee\rangle} \right) - \left( E_{ gf\rangle} - E_{ ge\rangle} \right)$	$ZZ_{ef2}$	-183 kHz	-301 kHz
$\left( E_{ ff\rangle} - E_{ ef\rangle} \right) - \left( E_{ fg\rangle} - E_{ eg\rangle} \right)$	$ZZ_{ff1}$	-211 kHz	-171 kHz
$\left( E_{ ff\rangle} - E_{ fe\rangle} \right) - \left( E_{ gf\rangle} - E_{ ge\rangle} \right)$	$ZZ_{ff2}$	-262 kHz	-289 kHz
$\left( E_{ ef\rangle} - E_{ gf\rangle} \right) - \left( E_{ eg\rangle} - E_{ gg\rangle} \right)$	$ZZ_{gf1}$	-402 kHz	-619 kHz
$\left( E_{ fe\rangle} - E_{ fg\rangle} \right) - \left( E_{ ge\rangle} - E_{ gg\rangle} \right)$	$ZZ_{gf2}$	-403 kHz	-464 kHz
Coefficient of $n_{q1}n_{q2}$	$J_{11}$	-304 kHz	-312 kHz
Coefficient of $n_{q1}^2n_{q2}$	$J_{21}$	38 kHz	25 kHz
Coefficient of $n_{q1}n_{q2}^2$	$J_{12}$	-24 kHz	-49 kHz
Coefficient of $n_{q1}^2n_{q2}^2$	$J_{22}$	5 kHz	43 kHz

Table 4.3: Device frequencies in the absence of external drives.  $J_{jk}$  are inferred from the 7  $ZZ$  values measured in the experiment.

$$\left\{ \begin{array}{l}
ZZ_{ge} = J_{11} + J_{12} + J_{21} + J_{22} \\
ZZ_{ef1} = J_{11} + 3J_{12} + J_{21} + 3J_{22} \\
ZZ_{ef2} = J_{11} + J_{12} + 3J_{21} + 3J_{22} \\
ZZ_{ff1} = 2J_{11} + 6J_{12} + 4J_{21} + 12J_{22} \\
ZZ_{ff2} = 2J_{11} + 4J_{12} + 6J_{21} + 12J_{22} \\
ZZ_{gf1} = 2J_{11} + 2J_{12} + 4J_{21} + 4J_{22} \\
ZZ_{gf2} = 2J_{11} + 4J_{12} + 2J_{21} + 4J_{22}
\end{array} \right. \quad (4.12)$$

When  $\Phi_{\text{DC}}$  is away from the anti-sweet spot, the transmon frequency is insensitive to the external DC flux, which ensures a decent Ramsey time for both transmons. The static  $ZZ$  strength between two transmons is suppressed around certain  $\Phi_{\text{DC}}$  labeled in the dashed lines in Fig. 4.2 (b) and (d). When considering both transmons as qutrits, there are in total 7 different  $ZZ$  values. The corresponding minimum DC flux points are different but very close for all 7  $ZZ$ s, ensuring the high-fidelity operation of the two-qutrit processor.

The  $ZZ$  suppression comes from interference of the Hamiltonian's capacitive coupling and inductive coupling terms. The residual  $ZZ$  comes from the transmons' negative anharmonicity, although the absolute  $ZZ$  value is more than a magnitude smaller than without the suppression ( $\Phi_{\text{ext}} = 0$  vs.  $\Phi_{\text{ext}} = 0.3795\Phi_0$ ). In fact, even when replacing the coupler SQUID with an ideal tunable inductor, there is still a similar stray  $ZZ$  coupling between two transmons. To reduce the minimum  $ZZ$  value, one can simultaneously reduce the coupling capacitance  $C_{q12}$  and increase coupler junction energy  $E_{jc}$ . One possible route to cancel static  $ZZ$  is to couple two objects with anharmonicities of opposite signs, such as transmon-fluxonium and transmon-CFSQ. Another possible solution is to add extra drives for  $ZZ$  cancellation, which is further discussed in Chapter. 5.

After the circuit quantization, we then calculate the QQ sideband interaction rates through flux parametric modulation. To understand the sideband rate, we follow the previous paper[55] and apply an adiabatic approximation to the Hamiltonian: The coupler mode frequency remains high ( $> 15$  GHz) above transmons' frequencies ( $< 4$  GHz) in the system. Therefore the coupler can be assumed static at the ground state. The non-dynamical potential of the coupler mode is removed by minimizing the Hamiltonian. Transmons are treated as duffing oscillators when calculating the effective sideband rate. Keeping up to 2nd order

expansions, the Hamiltonian  $H_{\text{ad}}$  under adiabatic approximation is

$$\begin{aligned}
H_{\text{ad}} &= \omega_{q1} a_{q1}^\dagger a_{q1} + \omega_{q2} a_{q2}^\dagger a_{q2} \\
&+ \frac{\alpha_1}{2} a_{q1}^\dagger a_{q1}^\dagger a_{q1} a_{q1} + \frac{\alpha_2}{2} a_{q2}^\dagger a_{q2}^\dagger a_{q2} a_{q2} \\
&+ g_1(t) \left( a_{q1}^\dagger + a_{q1} \right) \left( a_{q2}^\dagger + a_{q2} \right) \\
&+ g_2 \left( -a_{q1}^\dagger + a_{q1} \right) \left( -a_{q2}^\dagger + a_{q2} \right), \tag{4.13}
\end{aligned}$$

$$g_1(t) = \frac{\sqrt{E_{j1} E_{j2}}}{2E_{jc} \cos\left(\pi \frac{\Phi_{\text{ext}}(t)}{\Phi_0}\right)} \sqrt{\omega_{q1} \omega_{q2}}, \tag{4.14}$$

$$g_2 = \frac{\sqrt{C_{q1} C_{q2}}}{2C_{q12}} \sqrt{\omega_{q1} \omega_{q2}}. \tag{4.15}$$

Here  $g_1(t)$  and  $g_2$  are flux-tunable inductive coupling strength and constant capacitive coupling strength. Plugging in the RF flux modulation  $\frac{\pi \Phi_{\text{ext}}(t)}{\Phi_0} = \Phi_{\text{DC}} + \epsilon \cos(\omega_d t)$  into Supplementary Eq. (4.14) and assuming  $\epsilon \ll \Phi_{\text{DC}}$ , we obtain

$$\begin{aligned}
g_1(t) &= \frac{\sqrt{E_{j1} E_{j2}}}{2E_{jc}} \sqrt{\omega_{q1} \omega_{q2}} \frac{1}{\cos(\Phi_{\text{DC}} + \epsilon \cos(\omega_d t))} \\
&= \frac{\sqrt{E_{j1} E_{j2}}}{2E_{jc}} \sqrt{\omega_{q1} \omega_{q2}} \frac{(1 + \epsilon \sin(\omega_d t) \tan(\Phi_{\text{DC}}))}{\cos(\Phi_{\text{DC}})}. \tag{4.16}
\end{aligned}$$

Therefore the QQ sideband rate becomes (suppose  $|\psi_1\rangle$  and  $|\psi_2\rangle$  are states connected by the sideband)

$$\frac{\sqrt{E_{j1} E_{j2}}}{2E_{jc}} \sqrt{\omega_{q1} \omega_{q2}} \frac{\epsilon \tan(\Phi_{\text{DC}})}{\cos(\Phi_{\text{DC}})} A_{12}, \tag{4.17}$$

with

$$A_{12} = \langle \psi_1 | \left( a_{q1}^\dagger + a_{q1} \right) \left( a_{q2}^\dagger + a_{q2} \right) | \psi_2 \rangle, \tag{4.18}$$

and is proportional to the flux modulation rate.  $A_{12}$  is the state-dependent bosonic enhancement coefficient. Higher order corrections can be calculated using time-dependent

Schrieffer–Wolff transformation[71], and for our inductive coupler, both QQ blue and red sideband will have a similar interaction Hamiltonian under the same  $\epsilon$ :

$$\tilde{H}_{red} = \epsilon \frac{\sqrt{E_{j1}E_{j2}}}{2E_{jc}} \sqrt{\omega_{q1}\omega_{q2}} \frac{\tan(\Phi_{DC})}{2\cos(\Phi_{DC})} (t) a_{q1}^\dagger a_{q2} + h.c. \quad (4.19a)$$

$$\tilde{H}_{blue} = \epsilon \frac{\sqrt{E_{j1}E_{j2}}}{2E_{jc}} \sqrt{\omega_{q1}\omega_{q2}} \frac{\tan(\Phi_{DC})}{2\cos(\Phi_{DC})} (t) a_{q1} a_{q2} + h.c. \quad (4.19b)$$

The QR red ( $a_{r1}a_{r2}^\dagger + a_{r1}^\dagger a_{r2}$ ) and blue ( $a_{r1}a_{r2} + a_{r1}^\dagger a_{r2}^\dagger$ ) sidebands can also be realized through flux modulation. When the resonator is capacitively coupled to the qubit at strength  $g_{qri}$  and frequency difference  $\Delta_i = \omega_{qi} - \omega_{ri}$ , the transmon level is dressed by the resonator:

$$a'_{qi} = a_{qi} + \frac{g_{qri}}{\Delta_i} a_{ri} \quad (4.20)$$

Here  $a'_{qi}$  is the transmon annihilation operator in the dressed basis. Replacing  $a_{qi}$  with  $a'_{qi}$  in  $\tilde{H}_{TLS}$ , and choose  $\omega_d = \omega_{ri} \pm \omega_{qi}$ , we can active QR red and blue sideband between  $Q_1R_1$  and between  $Q_2R_2$ . The QR sideband rate through flux modulation is:

$$\epsilon \frac{g_{qri}}{\Delta_i} \frac{\sqrt{E_{j1}E_{j2}}}{2E_{jc}} \sqrt{\omega_{q1}\omega_{q2}} \frac{\tan(\varphi_{dc})}{\cos(\varphi_{dc})}. \quad (4.21)$$

In our system, the QR blue sideband frequencies are beyond the hardware limit ( $> 8\text{GHz}$ ). Therefore, we choose only to activate the QR red sideband through the flux line.

The QR blue sidebands have a different choice to activate [88]: The direct charge drives at half of the transition frequency with amplitude  $\epsilon_q$  can provide an effective QR blue sideband rate:

$$16g_{qri}^3 \epsilon_q^2 / \Delta_i^4. \quad (4.22)$$

This turns out to be easier to achieve in our experiments, as the drive frequency is halved and within the Fast Arbitrary Waveform Generator (AWG) sampling rate.

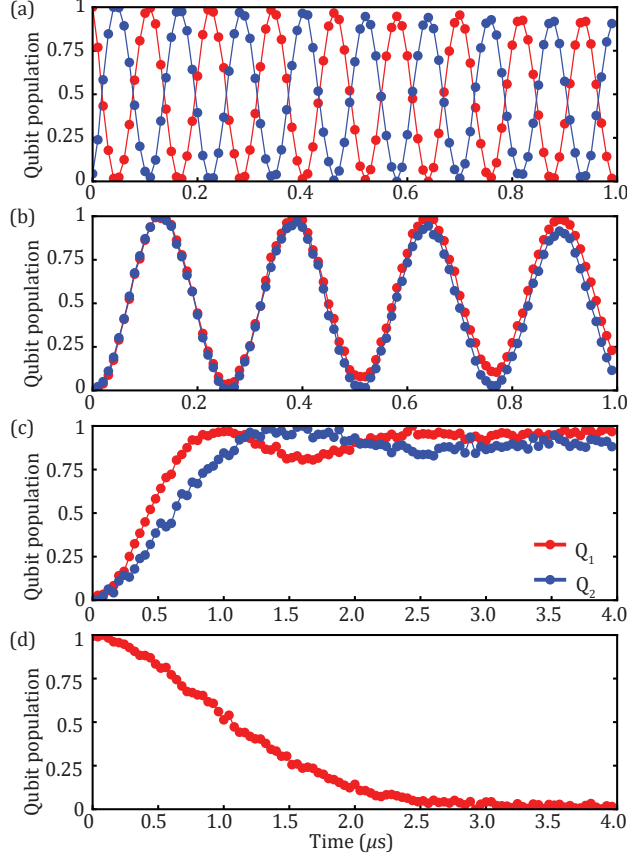


Figure 4.3: Experimentally realized QQ and QR sidebands. From top to bottom are separately (a) QQ red sideband  $|ge\rangle \leftrightarrow |eg\rangle$ , (b) QQ blue sideband  $|gg\rangle \leftrightarrow |ee\rangle$ , (c) QR blue sideband between QR1 and QR2  $|g0\rangle \leftrightarrow |e1\rangle$ , and (d) QR1 red sideband  $|e0\rangle \leftrightarrow |g1\rangle$ . Read-out on  $Q_1$  (red) and  $Q_2$  (blue) are scaled between 0 ( $|g\rangle$ ) and 1 ( $|e\rangle$ ). Data points are connected for visual guidance.

Fig. 4.3 demonstrates all realized QQ and QR sidebands needed for the various experiments. Fast QQ red sidebands at 8.5 MHz and modest QQ blue sidebands at 3.9 MHz are performed in the experiment through RF flux modulation of the inductive coupler. Both readouts for QQ red sideband (with initial state  $|eg\rangle$ ) and QQ blue sideband (with initial state  $|gg\rangle$ ) are shown in Fig. 4.3(a) and (b). The QR blue sidebands are generated through the charge lines that are coupled to the qubit pads, shown in Fig. 4.3(c) with initial state  $|g0\rangle$ . The QR1 red sidebands are activated through the coupler flux modulation (the QR2 red sideband is not shown because of frequency collision.). The on-resonance readout trace

for  $Q_1$  starting at  $|e0\rangle$  is plotted in Fig. 4.3(d).

## 4.2 Two-Qutrit Quantum Algorithms on a Programmable Superconducting Processor

After demonstrating a fast parametric coupler between two transmons with decent coherence, we move on to demonstrate a few quantum algorithms on our device [74]. Using the rich set of native entangling gates to provide excellent connectivity between different two-qutrit states, we demonstrate two-qutrit versions of Deutsch-Jozsa [19, 89], Bernstein-Vazirani [6, 89], and Grover’s search [33] algorithms without using any auxiliary qutrit (ancilla) [72]. Deutsch-Jozsa and Bernstein-Vazirani algorithms provide exponential and linear speed-ups, respectively, over corresponding classical algorithms, whereas Grover’s search provides a quadratic improvement. We perform two stages of Grover’s amplification with success probabilities significantly larger than classically achievable values.

For expression simplicity, we label the lowest three energy levels (qutrit subspace) for each transmon as  $\{|0\rangle, |1\rangle, |2\rangle\}$  in this chapter.

Gate type	On $Q_1$ (ns)	On $Q_2$ (ns)
$\pi/2_{01}$	49.50	49.71
$\pi/2_{12}$	41.27	44.15
$\pi_{01}$	94.98	95.41
$\pi_{12}$	78.52	84.28
$Z$	0	0
$H$	141.88	147.90

Table 4.4: Total gate lengths for different single-qutrit operations. The  $Z$  gates are implemented virtually.

### 4.2.1 Single-qutrit Gate operation

The native operations accessible for a single qutrit are

$$R_{01}(\phi, \theta) = \begin{bmatrix} \cos \frac{\theta}{2} & -e^{-i\phi} \sin(\theta/2) & 0 \\ e^{i\phi} \sin \frac{\theta}{2} & \cos \frac{\theta}{2} & 0 \\ 0 & 0 & 1 \end{bmatrix}, \quad (4.23a)$$

$$R_{12}(\phi, \theta) = \begin{bmatrix} 1 & 0 & 0 \\ 0 & \cos \frac{\theta}{2} & -e^{-i\phi} \sin(\theta/2) \\ 0 & e^{i\phi} \sin \frac{\theta}{2} & \cos \frac{\theta}{2} \end{bmatrix}, \quad (4.23b)$$

$$\Theta(x, y) = \begin{bmatrix} 1 & 0 & 0 \\ 0 & e^{ix} & 0 \\ 0 & 0 & e^{i(x+y)} \end{bmatrix}, \quad (4.23c)$$

Here,  $R_{01}(\phi, \theta)$  and  $R_{12}(\phi, \theta)$  are realized through sending a charge drives to the transmon pad at  $|0\rangle \leftrightarrow |1\rangle$  and  $|1\rangle \leftrightarrow |2\rangle$  transitions respectively with appropriate lengths and phases. The pure phase gate  $\Theta(x, y)$  is realized virtually: For each qutrit, we record two phase parameters  $\theta_{01}$  and  $\theta_{12}$  corresponding to the pulses applied to the  $|0\rangle \leftrightarrow |1\rangle$  and  $|1\rangle \leftrightarrow |2\rangle$  transitions respectively. To apply the  $\Theta(x, y)$  gate, we advance both  $\theta_{01}$  and  $\theta_{12}$  by  $x$  and  $y$  for all the subsequent pulses. The single-qutrit  $Z$  gate:

$$Z = \begin{bmatrix} 1 & 0 & 0 \\ 0 & \omega & 0 \\ 0 & 0 & \omega^2 \end{bmatrix} \quad (4.24)$$

becomes a special case of the generic phase gate:  $Z = \Theta\left(\frac{2\pi}{3}, \frac{2\pi}{3}\right)$ . Since all phase updates are performed in software, the  $Z$  gate (or a  $\Theta(x, y)$  gate) has 100% fidelity.

---

Parts of this section have been published in Ref. [74]

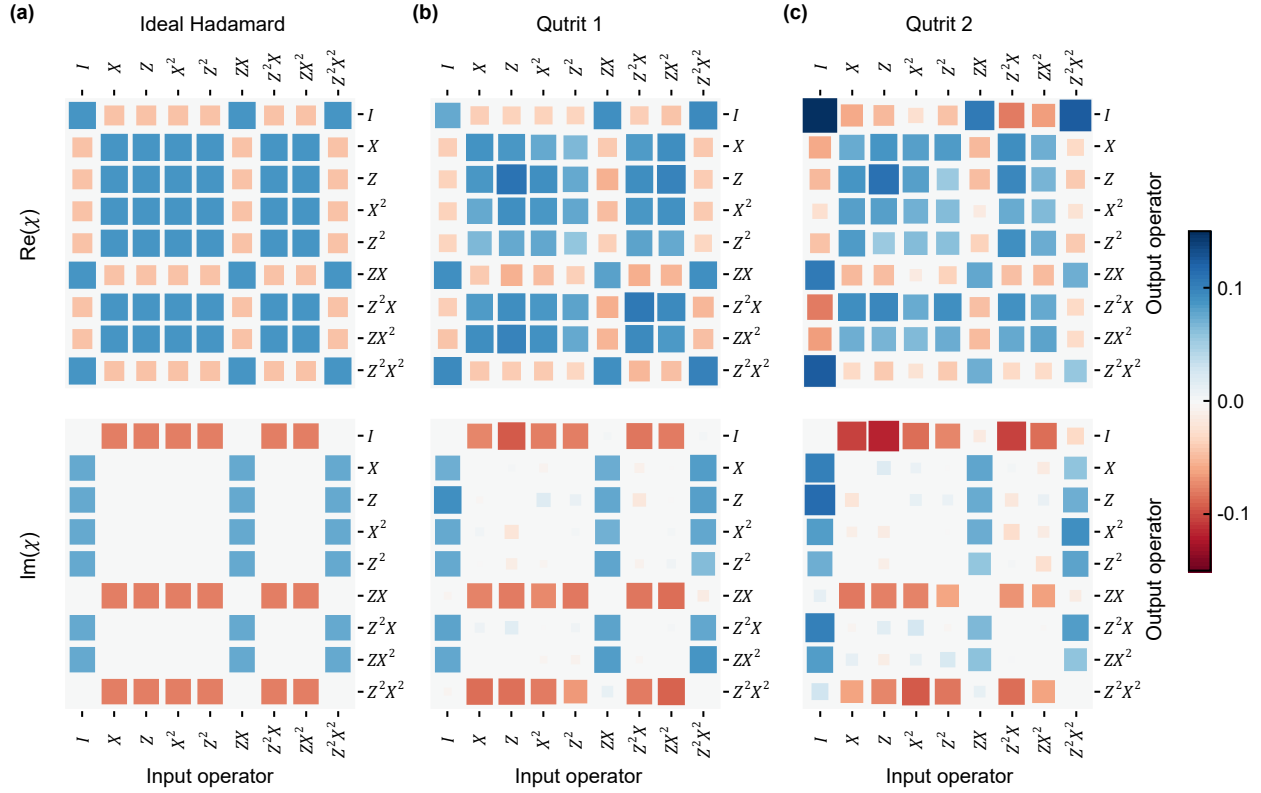


Figure 4.4: Process tomography for Hadamard gates. The top and bottom panels show real and imaginary components of the process matrix ( $\chi$ ) for (a) an ideal case, (b)  $Q_1$ , and (c)  $Q_2$ .

Eq. 4.23 forms a universal single-qutrit rotation set. For example, the  $H$  gate is deconstructed as

$$H = \frac{1}{\sqrt{3}} \begin{bmatrix} 1 & 1 & 1 \\ 1 & \omega & \omega^2 \\ 1 & \omega^2 & \omega \end{bmatrix} = R_{12} \left( 0, \frac{\pi}{2} \right) \cdot R_{01} (0, \beta) \cdot \Theta \left( \pi, \frac{\pi}{2} \right) \cdot R_{12} \left( 0, \frac{\pi}{2} \right) \cdot \Theta (0, \pi), \quad (4.25)$$

with  $\beta = 2 \tan^{-1}(\sqrt{2})$  and  $\omega = e^{\frac{2\pi}{3}i}$ . Similarly, the bit-shift gate  $X$  is decomposed as

$$X = \begin{bmatrix} 0 & 0 & 1 \\ 1 & 0 & 0 \\ 0 & 1 & 0 \end{bmatrix} = R_{01}(0, \pi) \cdot R_{12}(0, \pi). \quad (4.26)$$

Single-qutrit drives use roughly 5 MHz of Rabi rates with Gaussian-edge rectangular pulses of  $2\sigma$  tail lengths, whereas phase gates are realized by simply advancing the phases of the appropriate subsequent pulses. The envelope shape  $h(t)$  is defined in Eq. (4.27) with  $\sigma = 2.5$  ns,

$$h(t) = \begin{cases} A_0 e^{-\frac{(t-t_0-2\sigma)^2}{2\sigma^2}} & \text{if } t_0 < t < t_0 + 2\sigma, \\ A_0 & \text{if } t_0 + 2\sigma < t < t_1 - 2\sigma, \\ A_0 e^{-\frac{(t_1-2\sigma-t)^2}{2\sigma^2}} & \text{if } t_1 - 2\sigma < t < t_1, \\ 0 & \text{Otherwise,} \end{cases} \quad (4.27)$$

where,  $2\sigma$  is the Gaussian tail length,  $A_0$  is the amplitude, and  $t_1 - t_0$  is the total pulse length. The single-qutrit gates' lengths used in our experiments are shown in Table. 4.4.

Equipped with the universal single-qutrit gate set, we perform single-qutrit process tomography to benchmark the gate fidelity. We use the following nine different initial states:  $\{|j\rangle, (|j\rangle + |k\rangle)/\sqrt{2}, (|j\rangle + i|k\rangle)/\sqrt{2}\}$ ,  $\{j, k\} \in \{0, 1, 2\}$  in the process tomography. We obtain process fidelities of 98.96% ( $Q_1$ ) and 97.06% ( $Q_2$ ) for the  $H$  gate as shown in Fig. 4.4. The same for the  $Z$  gates are 97.48% ( $Q_1$ ) and 96.76% ( $Q_2$ ). Even though the  $Z$  gates should be nearly perfect, the process fidelities are limited by state preparation and measurement (SPAM) errors. Further, it is expected that the process fidelity for the  $Z$  gate should be larger than that of the  $H$  gate, which requires multiple physical pulses. The opposite experimental observation comes from different SPAM errors on different qutrit energy levels: The relaxation time of level  $|2\rangle$  is significantly smaller than that of level  $|1\rangle$ , leading to such

deviations in experiments.

### 4.2.2 Two-qutrit Gate operation

Along with single-qutrit rotations, we experimentally implement the generalized controlled-phase gate  $C_\theta(\theta, |mn\rangle) = \mathcal{I} - (1 - e^{i\theta}) |mn\rangle$  to realize a universal two-qutrit computation [11]. Here,  $C_\theta(\theta, |mn\rangle)$  represents a phase of  $\theta$  accumulated on level  $|mn\rangle$ , and  $I$  is an identity matrix of  $9 \times 9$ . We utilize sideband interactions to implement the Cphase gate in the two-qutrit subspace. The tune-up of these sidebands is very easy and similar to single-qubit Rabi experiments. We use a Gaussian-flatten pulse shape for all flux modulation drives, with 5 ns ramping and descending time. We initialize the qutrits in relevant states and sweep both frequency, and the flat length of the flux modulation drive  $\Phi_{\text{ext}}(t)$  to obtain a Chevron pattern. We demonstrate Chevron patterns for the six red sidebands in Fig. 4.5 and for the four blue sidebands in Fig. 4.6 at separately optimized pump amplitudes. The plots show average photon numbers on the qutrits as a function of time and drive frequencies. The resonance feature is selected at the drive frequency where the oscillation shows maximum contrast, as represented by the red dashed lines. We plot the line cuts along these selected frequencies for all the ten sidebands in Fig. 4.7 and use the traces to extract interaction rates and gate times. Other four red sidebands within the computational space can be utilized to implement *i*SWAP gates between relevant levels.

We have not used the blue sidebands for the algorithms due to lower rates. While theoretically larger rates should be achievable, we start to observe readout saturation [50] and distortions in the Chevron plots as visible in case of  $|01\rangle \leftrightarrow |12\rangle$  sideband (see Fig. 4.6). This distortion is most likely caused by the flux line's stray capacitive coupling to the coupler SQUID. The unwanted capacitive coupling, particularly at high (blue sideband) frequencies, results in asymmetrical parametric modulation [56, 50] of the SQUID loop. This effect can be solved by optimizing flux line geometry, allowing stronger blue sideband rates.

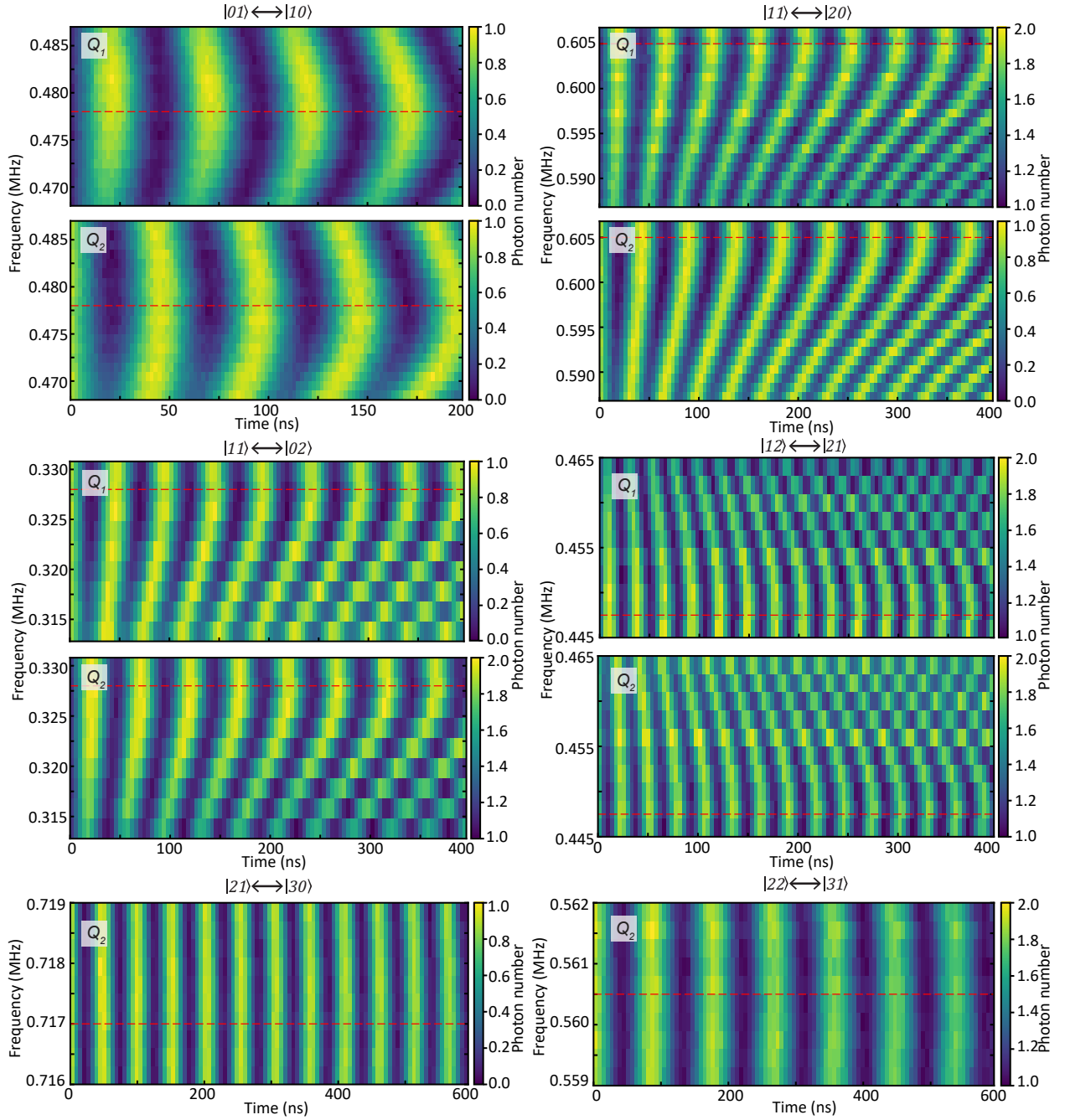


Figure 4.5: Chevron plots for the six two-qutrit red sidebands. All sidebands are parametrically activated by modulating the coupler at the corresponding transition frequencies. Pulses used for flux modulations have a rectangular shape with 5 ns long rising and falling Gaussian-shaped edges. The x-axis represents the length of the flat-top section. Both qutrits are simultaneously read out, and each data point is an average of 1000 experiments.

\*  $Q_1$ 's readout are not shown in the  $|21\rangle \leftrightarrow |30\rangle$  and  $|22\rangle \leftrightarrow |31\rangle$  cases, as the readout on  $|3\rangle$  is not optimized.

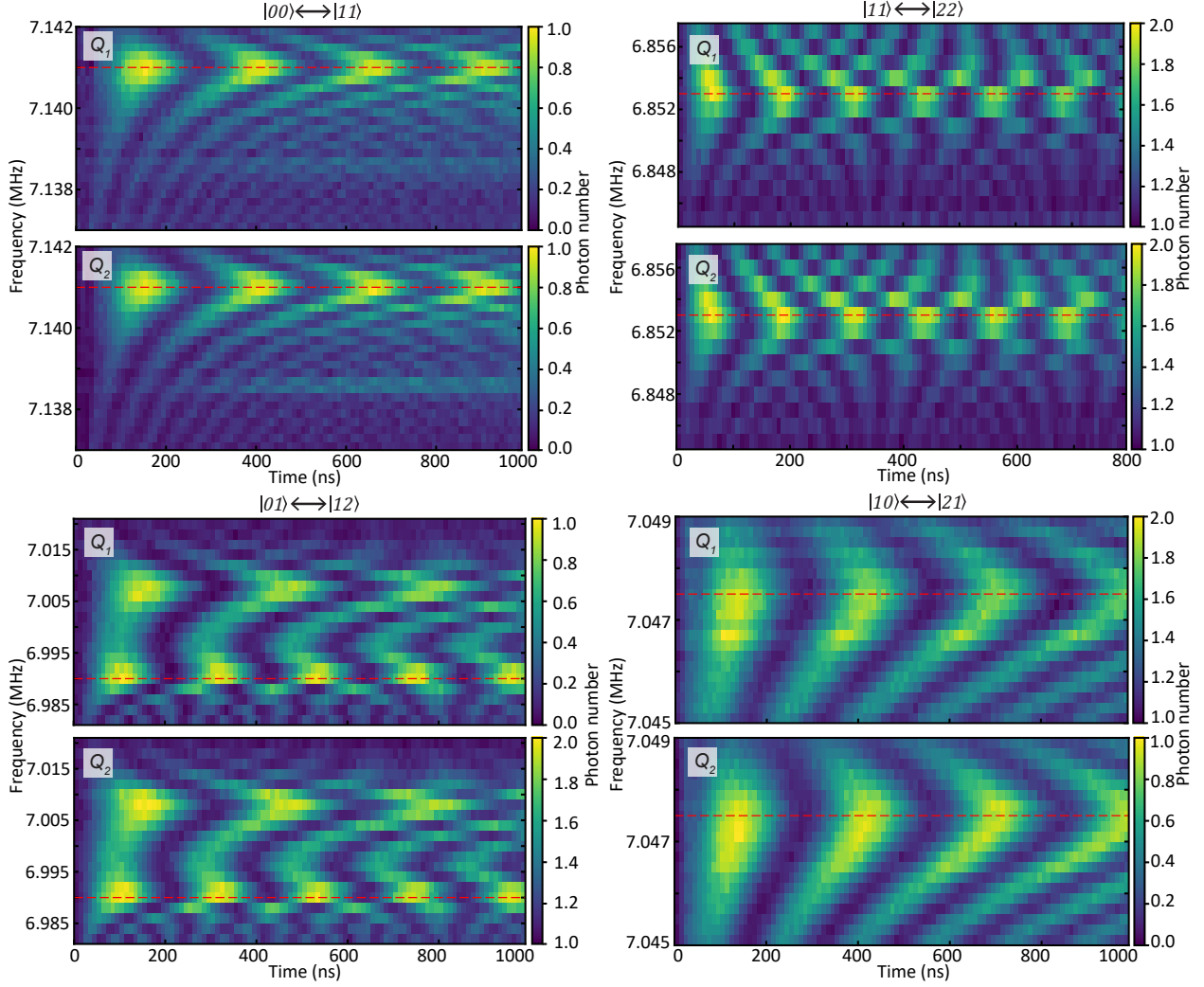


Figure 4.6: Chevron plots for the four two-qutrit blue sidebands. Sidebands are all parametrically activated through flux modulation of the coupler at relevant frequencies. Pulses used for flux modulations have a rectangular shape with 5 ns long rising and falling Gaussian-shaped edges, and the x-axis represents the length of the flat-top section. Each experimental data is an average of 1000 measurements.

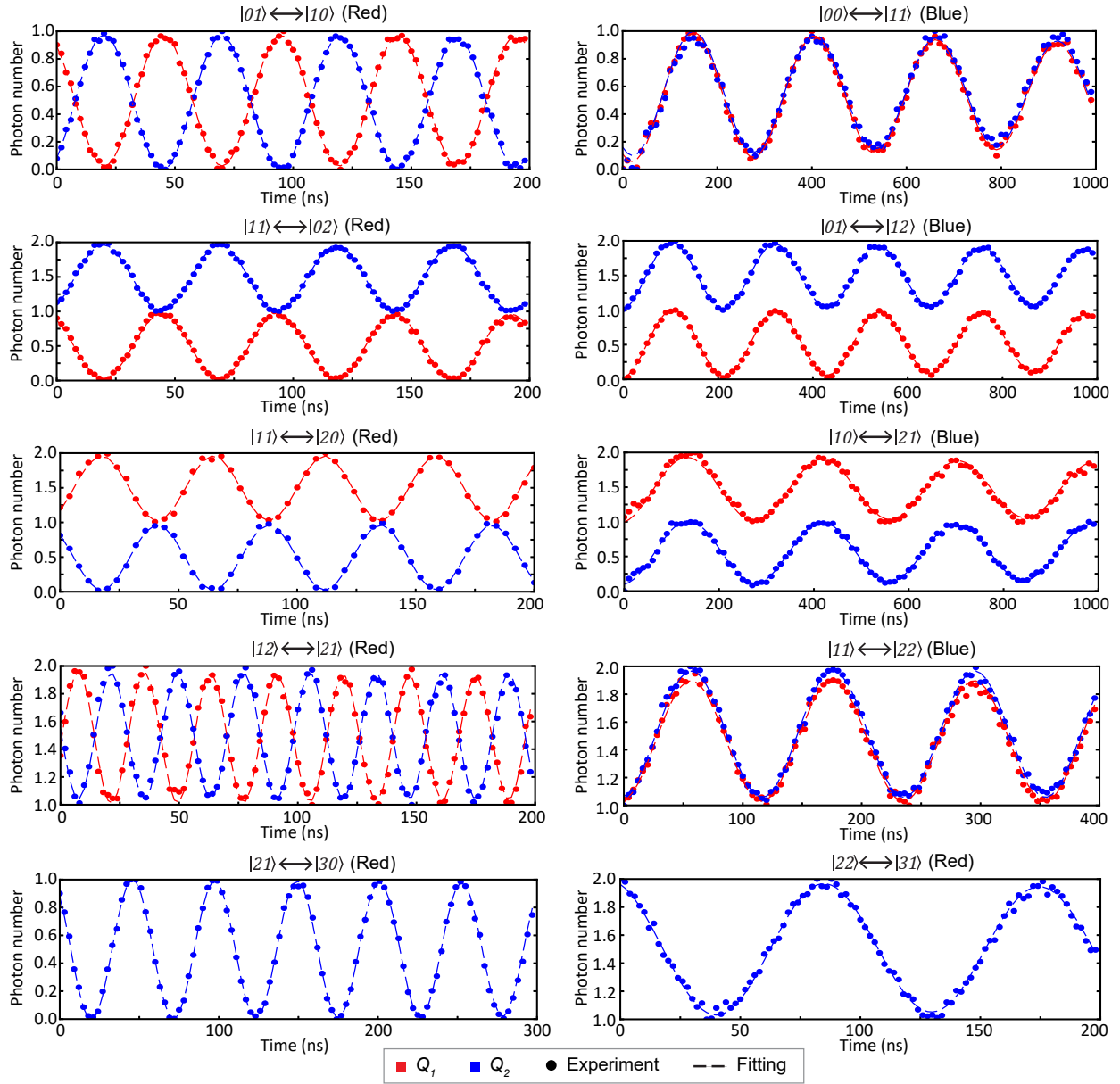


Figure 4.7: Coherent oscillations for all two-qutrit sidebands. On-resonance features from the Chevron plots are selected and fitted to extract the sideband rates and  $\pi$  rotation lengths (shown in Table. 4.5). Rectangular pulses with 5 ns long Gaussian edges are used for flux modulations, and the x-axis represents the length of the flat-top section. Each data point is an average of 1000 experiments.

Sideband	Type	Rate (MHz)	$\pi$ length (ns)
$ 10\rangle \leftrightarrow  01\rangle$	Red	20.1	30.2
$ 20\rangle \leftrightarrow  11\rangle$	Red	21.2	27.5
$ 02\rangle \leftrightarrow  11\rangle$	Red	20.3	29.7
$ 21\rangle \leftrightarrow  12\rangle$	Red	35.8	17.5
$ 21\rangle \leftrightarrow  30\rangle$	Red	19.3	29.9
$ 22\rangle \leftrightarrow  31\rangle$	Red	11.2	50.2
$ 00\rangle \leftrightarrow  11\rangle$	Blue	3.9	158.5
$ 10\rangle \leftrightarrow  21\rangle$	Blue	3.5	142.6
$ 01\rangle \leftrightarrow  12\rangle$	Blue	4.6	115.0
$ 11\rangle \leftrightarrow  22\rangle$	Blue	8.4	66.6

Table 4.5: Sideband rates and gate lengths for various interactions achieved with the device. The  $\pi$ -pulse lengths include both the flat-top part and 5 ns rising and falling Gaussian tail of the pulse. The distortion observed for the  $|01\rangle \leftrightarrow |12\rangle$  Chevron is most likely due to the stray charge coupling of the flux line to the SQUID loop (see text for details).

We use the red sideband  $|21\rangle \leftrightarrow |30\rangle$  and  $|22\rangle \leftrightarrow |31\rangle$  to implement the Cphase gate: these two QQ red sidebands bring the population out of the computational subspace. As shown in Fig. 4.8(a), we utilize two native CPhase gates  $C_\theta(\theta, |21\rangle)$  and  $C_\theta(\theta, |22\rangle)$ , which can be realized by applying two  $\pi$  rotations to  $|21\rangle \leftrightarrow |30\rangle$  and  $|22\rangle \leftrightarrow |31\rangle$  transitions with the phase of the second  $\pi$  pulse being advanced by  $\pi - \theta$  compared to the the first one. The optimized gate lengths are 55.9 ns and 94.0 ns for  $C_\theta(\theta, |21\rangle)$  and  $C_\theta(\theta, |22\rangle)$  respectively.

The CPhase gates on the states in the region (2), (4) and (6) (highlighted with yellow) need to decompose where the number indicates the number of single-qutrit rotations required. The decomposition starts from the target state, followed by the application of single-qutrit rotations to arrive at one of the states in the region (0) (following brown arrows). After applying the native CPhase gate, reverse single-qutrit rotations are administered, traversing the same path back to the target state. Fig. 4.8(b) shows the circuit decomposition of  $C_\theta(\pi, |00\rangle)$  as an example, which requires the maximum number of pulses. One can also use combinations of red and blue sidebands to further reduce the total number of gates. Note that, even though we have access to  $C_\theta(\pi, |12\rangle)$ , we do not use it due to poorer fidelity

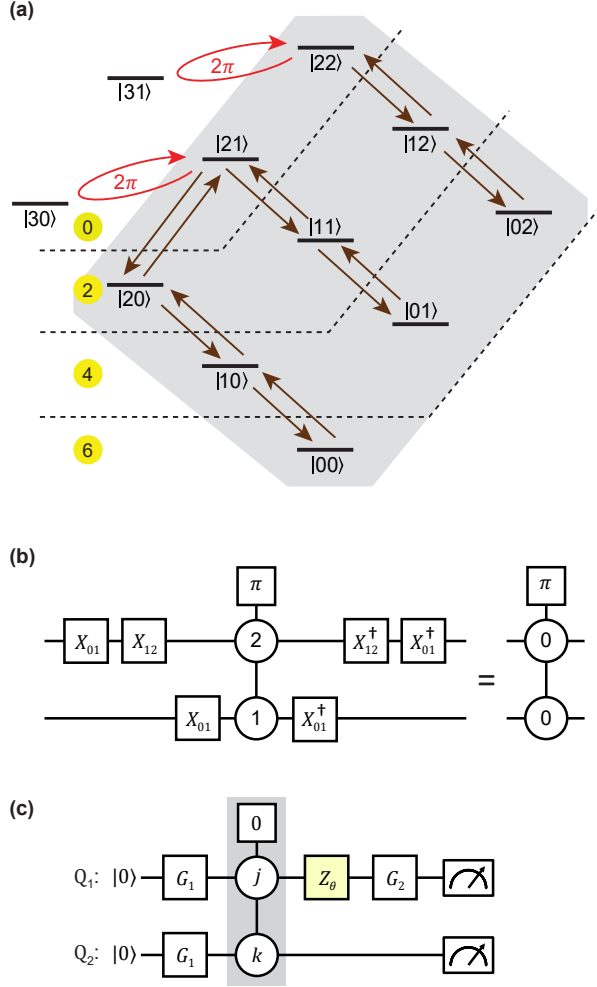


Figure 4.8: CPhase gate construction. (a) Partitioned energy level diagram. Flipping the phase of a specific target state in the region (0) is performed through a  $2\pi$  sideband rotation (shown in red arrow). Flipping the other target states requires a decomposition. The application of a  $C_\theta(\pi, |mn\rangle)$  follows the path marked with brown arrows starting from  $|mn\rangle$ . Here the numbers inside the yellow circle indicate the total number of single-qutrit  $\pi$  pulses required. (b) An example of circuit decomposition for the  $C_\theta(\pi, |00\rangle)$  gate. (c) Single-qutrit phase compensation calibration for a  $C_\theta(\pi, |jk\rangle)$  gate.

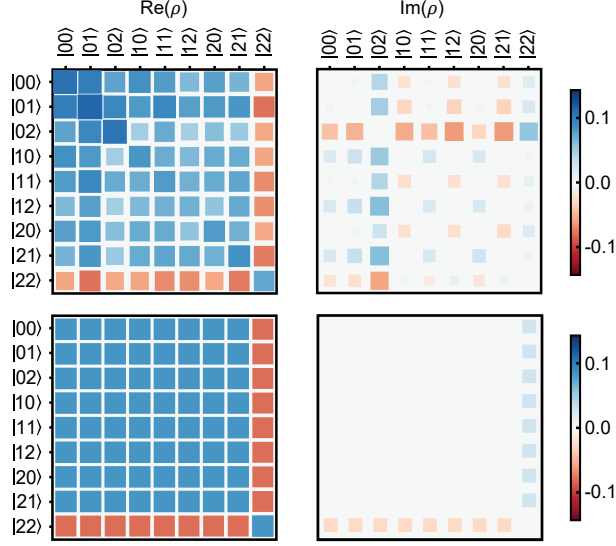


Figure 4.9: Two-qutrit tomography of the state  $\frac{1}{3}(|0\rangle + |1\rangle + |2\rangle)^{\otimes 2}$  after applying the CPhase gate  $C_{\theta}\left(\frac{8\pi}{9}, |22\rangle\right)$ . The top and bottom rows are experimental and ideal density matrices, with the real and imaginary parts shown in the left and right columns.

caused by a significantly lower lifetime of the  $|2\rangle$  and  $|3\rangle$  levels of  $Q_2$ .

The calibration of the CPhase gates involves compensation for the additional phases acquired during the gate operation [30]. In our coupler, both the AC stark shift and the rec-  
tification effect from SQUID flux modulation can cause qutrit frequencies to change during  
the gate, resulting in extra phases  $\beta_{01}^{(j)}$  and  $\beta_{12}^{(j)}$  for the  $|0\rangle \leftrightarrow |1\rangle$  and  $|1\rangle \leftrightarrow |2\rangle$  transitions  
of the  $j$ -th qutrit. We use the circuit shown in Fig. 4.8(c) to extract these additional phases.  
Starting from the ground state, we apply the gate  $G_1 = R_{01}\left(0, \frac{\pi}{2}\right)$  to both qutrits if cal-  
ibrating  $\beta_{01}^{(j)}$ , followed by  $C_{\theta}(0, |jk\rangle)$  and sweep the virtual phase  $Z_{\theta} = \Theta(\theta, 0)$  before the  
last gate  $G_2 = R_{01}\left(\pi, \frac{\pi}{2}\right)$  on  $Q_j$ . By fitting the readout on  $Q_j$  to  $C_0 + C_1 \sin\left(\beta_{01}^{(j)} + \theta\right)$ , one  
can extract the extra phase  $\beta_{01}^{(j)}$  acquired. A similar procedure is used to extract  $\beta_{12}^{(j)}$  where  
we use  $G_1 = R_{12}\left(0, \frac{\pi}{2}\right) \cdot R_{01}\left(0, \pi\right)$ ,  $G_2 = R_{12}\left(\pi, \frac{\pi}{2}\right)$ , and  $Z_{\theta} = \Theta(0, \theta)$ . Hence, each CPhase  
gate has four virtual phases corresponding to two native transitions for each qutrit. As a  
demonstration, we apply the CPhase gate  $C_{\theta}\left(\frac{8\pi}{9}, |22\rangle\right)$  on the state  $\frac{1}{3}(|0\rangle + |1\rangle + |2\rangle)^{\otimes 2}$   
(with initial state fidelity of 87.7%). The final state (shown in Fig. 4.9) obtained after

two-qutrit tomography [75] shows a fidelity of 82.4%, which is limited by the  $ZZ$  coupling between transmons and SPAM error.

### 4.2.3 Deutsch-Jozsa algorithm

After demonstrating universal control of the two-qutrit quantum processor, we move on to demonstrate some qutrit-version quantum algorithms. The Deutsch-Jozsa (DJ) algorithm [19] is one of the earliest quantum algorithms showing an exponential advantage over any classical algorithm. For an  $n$ -qutrit system, the task of the DJ algorithm is to distinguish a function  $f : \{0, 1, 2\}^n \rightarrow \{0, 1, 2\}$ , which takes  $n$ -trits as an input and outputs one trit, between two cases, a balanced or a constant function. The constant function always results in the same output (0, 1, or 2) independent of the input, whereas the balanced function outputs each of the three possibilities for exactly one-third of the possible inputs. Note that implementing the different test functions is often termed as the *oracle*. A deterministic classical algorithm needs  $3^{n-1} + 1$  queries (with at least two queries in the best case) to distinguish the two cases, whereas the DJ algorithm needs only one and hence provides the exponential speed-up.

Figure. 4.10(a) depicts our circuit implementation of the DJ algorithm. Two Hadamard gates are simultaneously applied to both qutrits initialized to  $|0\rangle$  (ground state) to prepare the state  $\frac{1}{3}(|0\rangle + |1\rangle + |2\rangle)^{\otimes 2}$ . The oracles (gray gates in Fig. 4.10(a)) are implemented by applying gates ( $W$ ) to the qutrits chosen from the set  $\mathcal{S} = \{I, X, X^2, Z, Z^2\}$ . For the constant case,  $W_1$  and  $W_2$  are picked up from the subset  $\mathcal{S}_c = \{I, X, X^2\}$ , and the total number of  $X$  gates modulo 3 specifies the constant output. For example, the gate  $X \otimes X^2$  would implement constant 0, whereas  $I \otimes X^2$  would be the case of constant 2. A balanced oracle can be realized by choosing any combination of elements from the set  $\mathcal{S}$  except for those cases that result in a constant function.

We implement 16 different balanced functions whose equivalent classical functions are

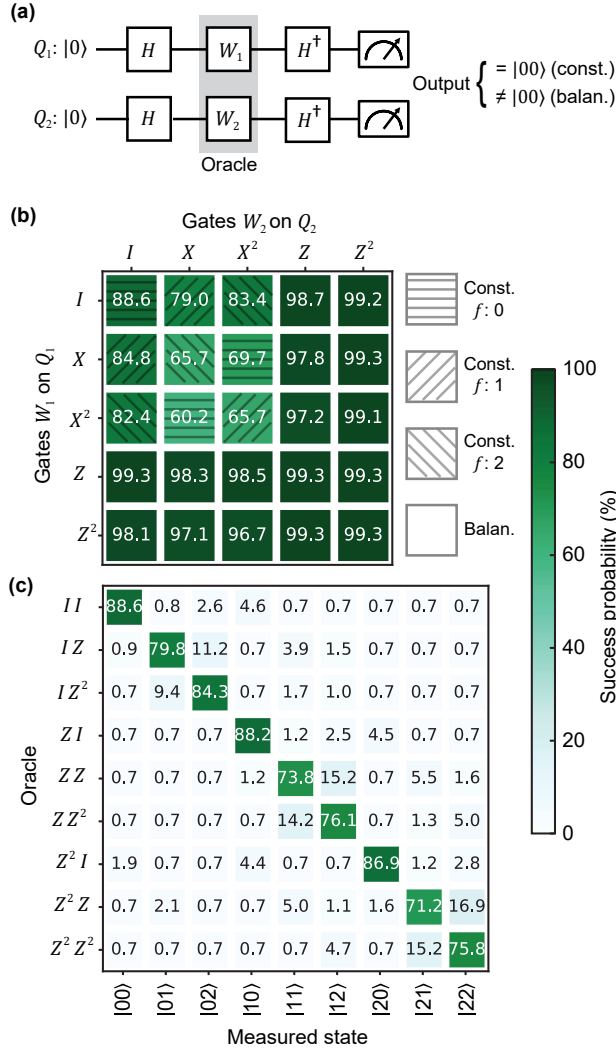


Figure 4.10: Deutsch-Jozsa and Bernstein-Vazirani algorithms. (a) Quantum circuit for the algorithms. In DJ algorithm, gates  $W_1, W_2 \in \{I, X, X^2, Z, Z^2\}$  are applied to implement a constant or a balanced oracle. The final output state being in  $|00\rangle$  or non  $|00\rangle$  distinguishes the two cases. (b) Experimental results for DJ algorithm. The rows and columns represent gates applied to  $Q_1$  and  $Q_2$  respectively. The average SPs are 75.5(3)% and 98.5(1)% for the constant (hatched boxes) and balanced (plain boxes) oracles respectively beating the classical rate of 50%. (c) Experimental results for BV algorithm. Each row corresponds to a specific oracle with the mapping  $\{I, Z, Z^2\} \rightarrow \{0, 1, 2\}$ . The diagonal terms show the SPs for all nine strings mapped to the basis states with an average of 78.3(3)%, which is much larger than the classical SP of 33.3%.

tabulated in Table 4.6. The balanced functions are implemented in our experiment as shown in Fig. 4.10(a). We use  $A$  and  $B$  to represent the classical ternary values (0, 1, and 2) for the two qutrits. The operators  $\oplus$  and  $\odot$  correspond to addition and multiplication modulo 3, respectively.

Oracle	Classical function	Oracle	Classical function
$Z \otimes I$	$A \oplus 0$	$I \otimes Z$	$0 \oplus B$
$Z \otimes X$	$A \oplus 1$	$X \otimes Z$	$1 \oplus B$
$Z \otimes X^2$	$A \oplus 2$	$X^2 \otimes Z$	$2 \oplus B$
$Z^2 \otimes I$	$(2 \odot A) \oplus 0$	$I \otimes Z^2$	$0 \oplus (2 \odot B)$
$Z^2 \otimes X$	$(2 \odot A) \oplus 1$	$X \otimes Z^2$	$1 \oplus (2 \odot B)$
$Z^2 \otimes X^2$	$(2 \odot A) \oplus 2$	$X^2 \otimes Z^2$	$2 \oplus (2 \odot B)$
$Z \otimes Z$	$A \oplus B$	$Z \otimes Z^2$	$A \oplus (2 \odot B)$
$Z^2 \otimes Z$	$(2 \odot A) \oplus B$	$Z^2 \otimes Z^2$	$(2 \odot A) \oplus (2 \odot B)$

Table 4.6: Equivalent classical functions (ternary valued) for the 16 balanced functions implemented in the Deutsch-Jozsa algorithm.

Finally, two  $H^\dagger$  gates are applied before simultaneous readout. A final measured state of  $|00\rangle$  indicates a constant function, whereas any other output implies a balanced function. The theoretical success probability (SP) for each case is 100%, and the experimental results are summarized in Fig. 4.10(b), where the hatched (unhatched) boxes represent constant (balanced) cases. The average SPs for the three constant cases with outputs  $\{0, 1, 2\}$  are separately 72.8(3)%, 76.5(3)% and 77.2(3)%, marked with horizontal, left and right hatching. The numbers in parentheses represent the standard error of the mean obtained after 20,000 repetitions of each oracle. For the 16 balanced cases, the average SP is 98.5(1)%. The SPs for all cases are well above the classical case, which would be 50% after a single query.

All experimental data are corrected for measurement error. Figure 4.11 shows the single-shot assignment probability for the nine basis states of our two-qutrit processor. We refer to this 2d array as the confusion matrix. Our readout fidelity is limited because there are no parametric amplifiers on the output lines. To fairly demonstrate the performance of

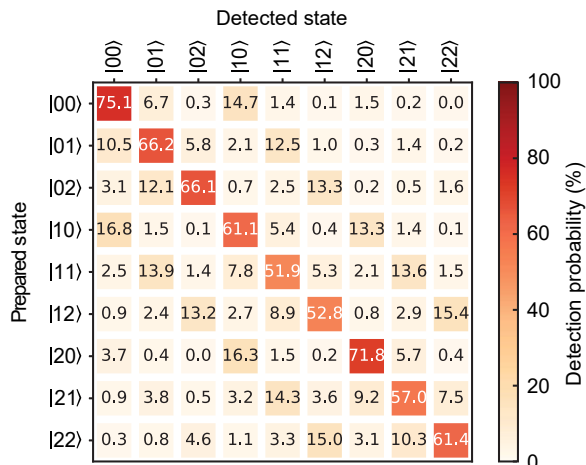


Figure 4.11: Heatmap of the confusion matrix.  $3^2$  basis states are prepared and measured for 20,000 times. The numbers represent average assignment probabilities.

the qutrit algorithms with single-shot results, we apply the inverse of the confusion matrix to the readout results to compensate for the measurement error. After correcting for the measurement error, it is possible that some of the readout counts (number of times the system found in a specific state) become negative, which happens due to drifts in the calibration parameters.

This is corrected using Maximum-Likelihood-Estimation (MLE) with the assumption that the minimum fluctuation of a measurement repeated  $N$  times should not be lower than  $\sqrt{N}$  (assuming normal distribution). We define the following cost function to avoid non-physical measurement counts:

$$f_c(\vec{p}, \vec{q}) = \sum_{j=1}^9 \left( \frac{p_j - q_j}{q_j} \right)^2, \quad (4.28)$$

with the restriction  $p_j \geq \sqrt{N}$ . Here  $\vec{q}$  contains the experiment counts (1d array of 9 elements corresponding to the basis states) after applying the inverse of the confusion matrix, and  $\vec{p}$  is the extracted counts after MLE.

#### 4.2.4 Bernstein-Vazirani algorithm

The Bernstein-Vazirani (BV) algorithm [6] for qutrits can be restated as follows: given an oracle  $f(\mathbf{x}, \mathbf{s}) \equiv \sum_{j=1}^n x_j s_j \pmod{3}$  that performs inner product between two strings of ternaries followed by modulo 3, the goal is to determine the unknown string  $\mathbf{s} = \{s_1, s_2, \dots, s_n\}$  where the user has control over the input string  $\mathbf{x}$ . The most efficient classical algorithm will need  $n$  oracle queries to find all digits of  $\mathbf{s}$ . BV algorithm, on the contrary, needs only one query and the quantum circuit is identical to the case of DJ as shown in Fig. 4.10(a). Oracles representing 9 different strings for our two-qutrit system are implemented by choosing gates ( $W$ ) from the set  $\{I, Z, Z^2\}^{\otimes 2}$  with the mapping  $\{I, Z, Z^2\} \rightarrow \{0, 1, 2\}$ . The final state of the system after measurement directly reveals the unknown string with 100% theoretical success rate. Fig. 4.10(c) tabulates the experimental results where the vertical axis represents gates applied to the qutrits corresponding to different unknown strings, and the horizontal axis shows the measured probability for each state. The diagonal entries indicate individual SPs for each input string mapped to the final state. The average SP for all 9 cases is 78.3(3)%, which is far above the classical SP of 33.3% after one query.

#### 4.2.5 Grover's Search

Grover's algorithm [33] provides a quadratic speed-up for searching an unstructured database. For a database of size  $\mathcal{N}$ , the algorithm can find the unique input that satisfies a certain condition using  $O(\sqrt{\mathcal{N}})$  search queries, while a classical algorithm requires on average  $\mathcal{N}/2$  repetitions. Several groups have recently realized Grover's search on qubit-based platforms [26, 72, 60, 91, 16]. For the two-qutrit case with  $\mathcal{N} = 3^2 = 9$ , the classical SPs with one and two rounds of search are  $\frac{1}{9} = 11.1\%$  and  $\frac{1}{9} + \frac{8}{9} \cdot \frac{1}{8} = 22.2\%$  respectively. The corresponding theoretical SPs for the original Grover's search are 72.6% and 98.4%, and can also be modified to achieve determinism [73, 51].

The quantum circuit for the two-qutrit Grover's search is illustrated in Fig. 4.12(a) that

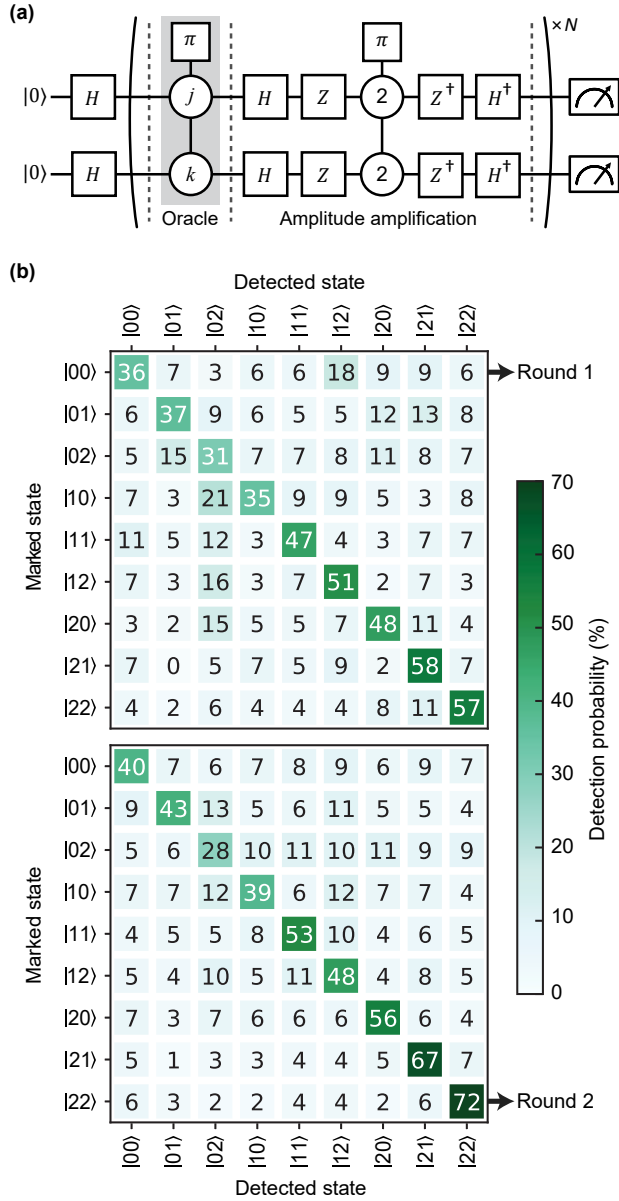


Figure 4.12: Grover's search algorithm for two-qutrits. (a) Quantum circuit. The oracles are implemented by CPhase gates  $C_\theta(\pi, |jk\rangle)$ . The diffusion operator amplifies the detection probability of the marked state. (b) Experimental results. Detection probabilities (corrected for measurement error) after one (top panel) and two (bottom panel) rounds of amplitude amplification are obtained with 20,000 averages. All individual success rates are far beyond the corresponding classical SPs of 11.1% and 22.2%.

doesn't use any auxiliary (ancilla) qutrit. It has four stages: initialization, oracle implementation, amplitude amplification, and measurement. Starting from the ground state, we apply Hadamard gates on both qutrits to initialize the system to the equal superposition state  $\frac{1}{3}(|0\rangle + |1\rangle + |2\rangle)^{\otimes 2}$ . A CPhase gate  $C_\theta(\pi, |jk\rangle)$ , that flips the phase of the target state  $|jk\rangle$ , is used to realize the oracle. Due to the structure of the Hilbert space and coherence parameters (see Table. 4.2), we have access to two native CPhase gates  $C_\theta(\pi, |22\rangle)$  and  $C_\theta(\pi, |21\rangle)$  and all other CPhase gates are realized in conjunction with single-qutrit rotations. Amplitude amplification of the marked state happens through Grover's diffusion or reflection unitary, which is constructed using a phase flip of the  $|22\rangle$  state sandwiched between Hadamard and  $Z$  gates. Here, we utilized the decomposition  $C_\theta(\pi, |00\rangle) = (ZZ) \otimes C_\theta(\pi, |22\rangle) \otimes (Z^\dagger Z^\dagger)$ . Simultaneous measurements on the qutrits are performed after one and two iterations of Grover's search for each target state. During a similar search using three qubits ( $\mathcal{N} = 8$ ), each oracle (and amplification) step requires eight CNOT gates (for a linear chain) [91], resulting in an *eight-fold rise* in entangling operations compared to our efficient two-qutrit implementation.

Figure 4.12(b) shows the experimentally obtained detection probabilities for the 9 different marked states after single (top panel) and double (bottom panel) rounds of the Grover's iteration. Each row represents a probability distribution acquired with 20,000 repetitions and after correcting for measurement error. The diagonal terms represent successful detection rates with an average SP of 44.4(3)% after the first round, which increases to 49.6(3)% with the second iteration. The performance degradation of target states closer to  $|00\rangle$  is caused by the less-efficient implementations of the corresponding oracles, where more single-qutrit rotations are required for the CPhase gate decomposition (see Section. 4.2.2). As promised by the algorithm, experimental detection probabilities for the individual correct states increased after the second iteration for all cases (except for  $|02\rangle$  and  $|12\rangle$ , which we attribute to the lower lifetime of  $Q_2$ 's  $|2\rangle$  level).

### 4.2.6 Error Analysis

Multiple error sources limit us from approaching the theoretical success rates for different quantum algorithms. In order to extract contributions from different sources, we perform master equation simulations in the lab frame for Grover’s search using the coherence and cross-Kerr parameters obtained experimentally. We consider a  $4 \times 4$  dimensional Hilbert space describing the lowest four energy eigenstates of each transmon and insert three different error channels, namely, relaxation, dephasing, and static  $ZZ$  progressively. We do not include the inductive coupler in the simulation as it has a much higher resonance frequency ( $> 15$  GHz) during any operation and thus should not be excited. We compute the squared statistical overlap (SSO) [72] between two sets of probability distribution  $\vec{p}$  and  $\vec{p}'$  defined as  $\left(\sum_{j=0}^8 \sqrt{p_j p'_j}\right)^2$  for each of the oracle implementation and then determine the mean value from nine different oracle applications. We first verify that in the absence of any error channel, our simulation produces probability distributions that are nearly identical with the ideal values. Next, we include the three error channels one by one and recompute the SSOs with respect to the ideal probability distribution with increased circuit depths. We tabulate the drop in SSOs after one and two rounds of Grover’s search in Table. 4.7, which indicate their individual error contributions to the algorithm. The average experimental SPs beat the classical rates of 11.1% and 22.2% for the two rounds by more than a factor of 2, with clear improvement in performance after the second iteration.

Two biggest error sources are the inter-qutrit dispersive coupling and the dephasing. The

Error channel	After 1 round	After 2 rounds
Relaxation ( $T_1$ )	0.83%	11.89%
Dephasing ( $T_\phi$ )	2.70%	16.07%
Static $ZZ$	5.08%	13.38%

Table 4.7: Error budget for the two-qutrit Grover’s search algorithm. Drops in SSOs after one and two rounds of amplitude amplification are shown due to different error channels.

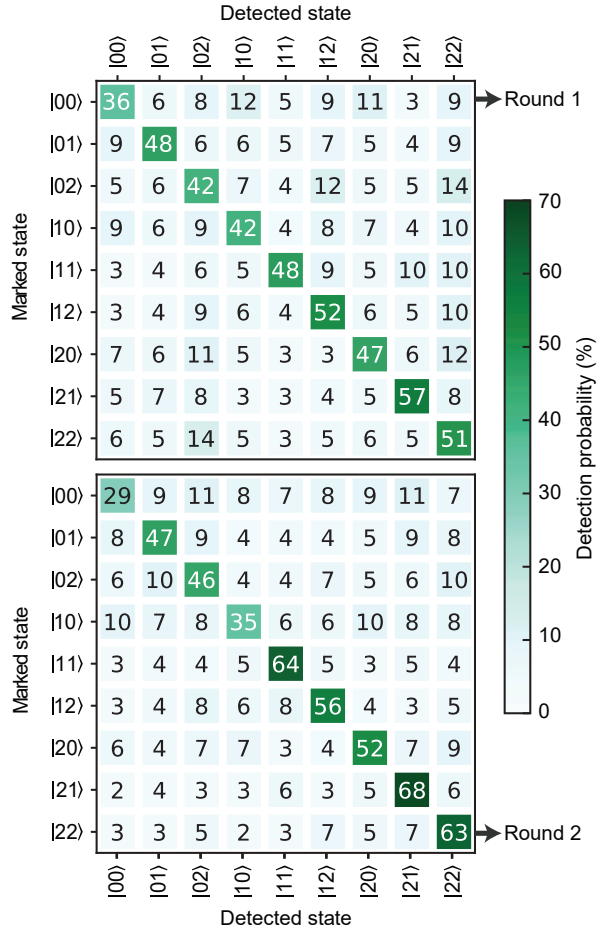


Figure 4.13: Master equation simulation of two-qutrit Grover's search with one and two stages of amplitude amplification using experimentally measured parameters. These results are in good agreement with the experimental outcomes shown in Fig. 4.12(b) in the main text.

inter-qutrit dispersive coupling includes both the static- $ZZ$  values measured in Table. 4.3 and the dynamic- $ZZ$  terms induced during (parametric) gate operations. The  $ZZ$  interactions introduce unwanted phase accumulations that reduce the performance of both single-qutrit and CPhase gates. The dephasing noise is also a significant source of error. The deepest circuit (2 stages of Grover’s search) implemented includes 17 single-qutrit and 4 two-qutrit gates, with a total execution time of  $2.11 \mu\text{s}$ . This time becomes comparable to the qutrit’s Ramsey times (see Table 4.2) and strongly degrades the success rates. The third one is the relaxation time, and its contribution is smaller than the dephasing error as our qutrits’  $T_1$  are typically longer than  $T_2$ . The fourth source is the leakage to non-computational levels. However, we use Gaussian-filtered rectangular pulses with maximum single-qutrit rotations rates being much smaller than the energy gaps, and thus errors due to leakage should not be significant. While we have not explicitly measured the leakage to the participating levels for the CPhase gates, from the continued contrast of the calibration curves (bottom two plots in Fig. 4.7), we anticipate a negligible effect. Besides, in our simulation, we keep the first 4 levels for the transmon to always include the leakage error. In order to verify that we have captured all the main sources of error, we compare the experimental results with simulated outcomes as shown in Fig. 4.13. Those show a very good agreement with SSOs of 94.0% and 97.1% for one and two stages of amplitude amplification.

### 4.3 Programmable Autonomous stabilization

After demonstrating a universal unitary operation on a two-qutrit system, we move on to engineer the dissipation process between each transmon-resonator pair. Inspired by laser cooling, tailored dissipation can be used for stabilizing entanglement, a prior step towards AQEC [86, 38, 57, 31, 50, 49] that achieve hardware efficiency in the experiment. By coupling the qubit system to some cold reservoirs, one can engineer the Hamiltonian such

---

Parts of this section have been published in Ref. [48]

that the population will flow directionally to the stabilized point in the Hilbert space, and extra entropy is autonomously dumped into the cold reservoir during the process.

In this section, we realize an autonomous stabilization protocol with superconducting circuits that allows selection from a broad class of states, including the maximally entangled states. We use microwave-only drives with tunable parameters such as drive detunings and strengths that allow fast programmable switching between Bell states of different parities. The system is based on a two-transmon inductive coupler design (see Section. 4.1) that allows fast parametric interactions between qubits without significantly compromising their coherence. The readout resonators are also used as cold reservoirs, eliminating the requirement for extra components. We perform stabilization spectroscopy and demonstrate a fidelity over 78% for all stabilized states. For odd and even parity Bell pairs, we measured 84.6% and 82.5% stabilization fidelity and a stabilization time of 1.8  $\mu\text{s}$  and 0.9  $\mu\text{s}$  respectively. The current stabilization protocol cannot realize AQEC and a larger code distance between logical states is necessary [48, 50, 49] for demonstrating quantum error correction. The structure of the section is as follows. First, we explain the Hamiltonian construction of the stabilization protocol. Then, we discuss the experimental measurement of individual stabilized states and demonstrate a dissipative switch of Bell state parity.

### 4.3.1 *Stablization theory*

We consider a system of two coupled qubit-resonator pairs  $\{Q_1, Q_2\}$  and  $\{R_1, R_2\}$ . The lossy resonators serve as both cold baths and dispersive readouts for the qubits. We label the ground and the first excited states of the qubits  $Q_{1/2}$  as  $|g\rangle$  and  $|e\rangle$ , and of the resonators  $R_{1/2}$  as  $|0\rangle$  and  $|1\rangle$ , with the full system state being represented as  $|Q_1 Q_2 R_1 R_2\rangle$ . The system Hamiltonian  $H_{\text{sys}} = H_{QQ} + H_{QR1} + H_{QR2}$  includes the dominant two-qubit interaction  $H_{QQ}$  and qubit-resonator interactions  $H_{QRj}, j = \{1, 2\}$  acting as perturbations. We label the four eigenstates of  $H_{QQ}$  as  $\{|A\rangle, |B\rangle, |C\rangle, |D\rangle\}$  with eigenenergies  $\{E_A < E_B \leq E_C \leq E_D\}$  so

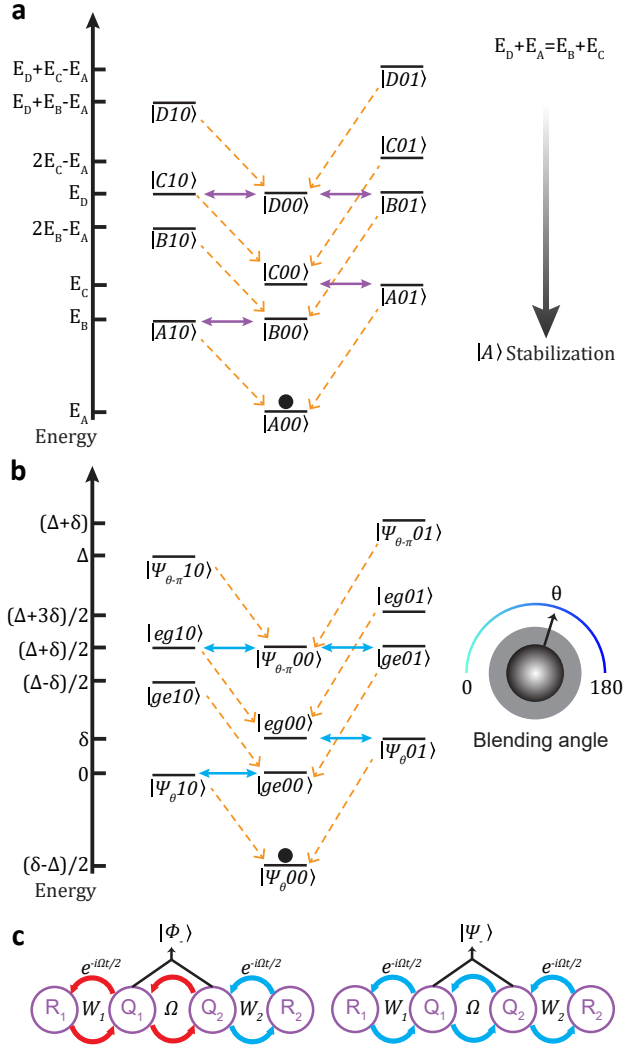


Figure 4.14: **Programmable stabilization protocol.** **a** General stabilization scheme. Two qubits' eigenstates  $\{|A\rangle, |B\rangle, |C\rangle, |D\rangle\}$  are plotted in the energy level diagram. When the energy relation  $E_D + E_A = E_B + E_C$  is satisfied,  $|A\rangle$  is stabilized. Qubit-resonator interactions and resonator photon decay rate  $\kappa$  are shown in blue and orange arrows. Qubit decay rate  $\gamma$  is assumed slowest and not plotted. **b** Stabilization of entangled states  $|\Psi_\theta\rangle = \sin(\theta/2)|gg\rangle - \cos(\theta/2)|ee\rangle$  or  $|\Phi_\theta\rangle = \sin(\theta/2)|ge\rangle - \cos(\theta/2)|eg\rangle$ . **c** A special case of **b** that stabilizes the odd and even parity bell states  $|\Phi_\pm\rangle$  and  $|\Psi_\pm\rangle$ . Circulating arrows are color-coded to represent red (exchange-like) and blue (two-photon-pumping) sidebands respectively. The QQ and QR sideband rates are separate  $\Omega$  and  $W_j$ , and the QR sideband is detuned in frequency by  $\Omega/2$ .

that  $|A\rangle$  is the target state to stabilize. Our stabilization scheme involves engineering a one-way flow of population to  $|A\rangle$  connecting all intermediate eigenstates of the system.

We now derive the energy matching requirements for an efficient stabilization protocol in our two-qubit-two-resonator system depicted in Figure 4.14(a). We control the form of the target stabilized state  $|A\rangle$  by choosing different two-qubit interaction strengths and detunings that control  $H_{QQ}$ . We change the resonator photon energy in the rotating frame by detuning the QR interactions. The dynamics of  $H_{\text{sys}}$  are captured by considering the following set of eigenstates:  $\{|A\rangle, |B\rangle, |C\rangle, |D\rangle\} \otimes \{|00\rangle, |10\rangle, |01\rangle\}$ . We neglect the resonator state  $|11\rangle$  as the probability of simultaneous population in both resonators  $\{R_1, R_2\}$  is extremely low when resonator decay rate  $\kappa$  is much larger than the qubit decay rate  $\gamma$  (assumed identical). The central column in Fig. 4.14(a) shows the eigenstates of  $H_{QQ}$  with no photons in the resonators. The left column represents the same states with one photon in the left ( $R_1$ ) resonator and similarly for the right column is associated with the second resonator ( $R_2$ ). We engineer the photon energies in  $R_1$  and  $R_2$  to be  $E_B - E_A$  and  $E_C - E_A$  respectively through tuning the QR interactions  $H_{QRj}$ . This condition puts two transitions  $|A01\rangle \leftrightarrow |C00\rangle$  and  $|A10\rangle \leftrightarrow |B00\rangle$  on resonance, shown in Fig. 4.14(a). If  $\langle A01|H_{QR1}|C00\rangle$  and  $\langle A10|H_{QR2}|B00\rangle$  are non-zero, two on-resonance oscillations between  $|C00\rangle, |A01\rangle$  and between  $|A10\rangle, |B00\rangle$  will be created. Since both resonators are lossy, the oscillation will quickly damp to  $|A00\rangle$ . To complete the downward stabilization path, we need to also connect  $|D00\rangle$  into the flow. We further require that the following terms are non-zero so that the transfer path is not blocked:  $\langle B01|H_{QR1}|D00\rangle, \langle C10|H_{QR2}|D00\rangle$ . If all four interaction strengths (shown in green double-headed arrows in Fig. 4.14(a)) are dominant over the qubit decay rate, populations in  $|B\rangle, |C\rangle$ , and  $|D\rangle$  will flow to  $|A\rangle$ . From Fermi's golden rule, the interaction strength between two states is quadratically suppressed by their energy gap and maximized when on-resonance [41]. This imposes a simple energy-matching requirement for efficient stabilization:  $E_D + E_A = E_B + E_C$ . Energy degeneracy within  $\{|B\rangle, |C\rangle, |D\rangle\}$  will

not affect the stabilization scheme, because it will not block the dissipative flow to  $|A00\rangle$  in Fig. 4.14(a).

As an explicit demonstration, we first stabilize a continuous set of entangled states  $|\Psi_\theta\rangle = \sin(\theta/2)|gg\rangle - \cos(\theta/2)|ee\rangle$ , illustrated in Fig. 4.14(b). Here,  $\theta$  can be regarded as a ‘‘blending angle’’ between the two even parity states  $|gg\rangle$  and  $|ee\rangle$ . We introduce three sideband [88] transitions into the system: qubit-qubit (QQ) blue sideband  $|gg\rangle \leftrightarrow |ee\rangle$  with rate  $\Omega$  and two qubit-resonator (QR) blue sidebands  $|g0\rangle \leftrightarrow |e1\rangle$  between  $Q_j$  and  $R_j$  with rate  $W_j$ . In this context, ‘sideband’ refers to a two-photon process where either a single photon is exchanged at the frequency difference (known as the red sideband) or two photons are simultaneously driven at the frequency sum (referred to as the blue sideband). To ensure that  $H_{QRj}$  act as perturbations over  $H_{QQ}$ , we adjust the drive strengths to satisfy  $\Omega \gg W_j$ . We further detune the QQ, QR1, and QR2 blue sideband by  $\delta$ ,  $(\Delta - \delta)/2$ , and  $(\Delta + \delta)/2$  in frequencies, with  $\Delta = \sqrt{\Omega^2 + \delta^2}$ . The detuning  $\delta$  determines the blending angle  $\theta = \tan^{-1}\left(\frac{\delta + \Delta}{\Omega}\right)$  with a range of  $[0, \frac{\pi}{2})$ . In the presence of these three drives, the rotating frame Hamiltonian  $H_{\text{sys}}$  is

$$\begin{aligned}
H_{\text{sys}} = & \frac{\Omega}{2} (a_{q1}a_{q2} + h.c.) + \delta a_{q1}^\dagger a_{q1} \\
& + \frac{W_1}{2} (a_{q1}a_{r1} + h.c.) + \frac{W_2}{2} (a_{q2}a_{r2} + h.c.) \\
& + \frac{\Delta + \delta}{2} a_{r1}^\dagger a_{r1} + \frac{\Delta - \delta}{2} a_{r2}^\dagger a_{r2}.
\end{aligned} \tag{4.29}$$

Here  $a_{qj}$  and  $a_{rj}$  are separately the  $j$ -th qubit’s and resonator’s annihilation operator. Anharmonicity  $\alpha$  is omitted from Equation (1) by treating both transmons as two-level systems. The presence of anharmonicity effectively suppresses the higher energy levels’ population in either transmon. Under the combined conditions  $\Omega \gg W_j \sim \kappa \gg \gamma$  and  $W_j = W$ , the eigenstates with zero resonator photons are  $\{|\Psi_\theta 00\rangle, |ge00\rangle, |eg00\rangle, |\Psi_{\pi-\theta} 00\rangle\}$ , with corresponding eigenenergies  $\{(\delta - \Delta)/2, 0, \delta, (\delta + \Delta)/2\}$ . Assuming the lossy resonator has a

Lorentzian energy spectrum, the two-step refilling rate  $\Gamma_t$  from  $|eg00\rangle$  to  $|\Psi_{\theta}00\rangle$  ( $|eg00\rangle \leftrightarrow |\Psi_{\theta}01\rangle, |\Psi_{\theta}01\rangle \rightarrow |\Psi_{\theta}00\rangle$ ) is [41]

$$\Gamma_t = \frac{W^2 \cos^2(\theta/2) \kappa}{\kappa^2 + W^2 \cos^2(\theta/2)}. \quad (4.30)$$

The other two-step transitions  $|ge00\rangle \rightarrow |\Psi_{\theta}00\rangle, |\Psi_{\theta-\pi}00\rangle \rightarrow |ge00\rangle$ , and  $|\Psi_{\theta-\pi}00\rangle \rightarrow |eg00\rangle$  also have the same rate.

Then we calculate the steady state fidelity for  $|\Psi_{\theta}00\rangle$ . Suppose the steady state population at the four basis states  $\{|\Psi_{\theta}\rangle, |ge\rangle, |eg\rangle, |\Psi_{\theta-\pi}\rangle\}$  are separately  $\{w, x, y, z\}$ . We assume the photon population in both resonators is transitional and ignore their contribution to the steady-state fidelity. This means  $w + x + y + z = 1$ . The steady-state configuration should balance the following two processes:

(a) two-step refilling process:  $|ge\rangle \rightarrow |\Psi_{\theta}\rangle, |eg\rangle \rightarrow |\Psi_{\theta}\rangle, |ge\rangle \rightarrow |\Psi_{\theta}\rangle$ , and  $|ge\rangle \rightarrow |\Psi_{\theta}\rangle$ .

All the transition rates are the same

$$\Gamma_t = \frac{W^2 \cos^2(\theta/2) \kappa}{\kappa^2 + W^2 \cos^2(\theta/2)} \quad (4.31)$$

(b) Single photon loss in each qubit. The following four transitions have the same rate  $\sin^2(\theta/2) \gamma$ :  $|ge\rangle \rightarrow |\Psi_{\theta}\rangle, |eg\rangle \rightarrow |\Psi_{\theta}\rangle, |ge\rangle \rightarrow |\Psi_{\theta-\pi}\rangle$ , and  $|eg\rangle \rightarrow |\Psi_{\theta-\pi}\rangle$ . The reversed four transitions have the same rate  $\cos^2(\theta/2) \gamma$ .

Therefore, the steady-state population should satisfy the following equations

$$\begin{cases} (\Gamma_t + \sin^2(\theta/2)\gamma)(x+y) - 2\cos^2(\theta/2)\gamma w & = 0, \\ (\Gamma_t + \sin^2(\theta/2)\gamma)z + \cos^2(\theta/2)\gamma w - (\Gamma_t + \gamma)x & = 0, \\ (\Gamma_t + \sin^2(\theta/2)\gamma)z + \cos^2(\theta/2)\gamma w - (\Gamma_t + \gamma)y & = 0, \\ 2\cos^2(\theta/2)\gamma(x+y) - (2\Gamma_t + 2\sin^2(\theta/2)\gamma)z & = 0, \\ w + x + y + z & = 1. \end{cases} \quad (4.32)$$

This gives the following populations

$$\begin{cases} w & = \left( \frac{\Gamma_t + \gamma \sin^2(\theta/2)}{\Gamma_t + \gamma} \right)^2, \\ x & = \frac{\cos^2(\theta/2)\gamma}{\Gamma_t + \gamma - \cos^2(\theta/2)\gamma} w, \\ y & = x, \\ z & = \frac{\cos^2(\theta/2)\gamma}{\Gamma_t + \sin^2(\theta/2)\gamma} x. \end{cases} \quad (4.33)$$

And  $\mathcal{F}_\infty = w$  is the steady state fidelity.

Similarly, we can stabilize another set of entangled states with odd parity  $|\Phi_\theta\rangle = \sin(\theta/2)|ge\rangle - \cos(\theta/2)|eg\rangle$ . We introduce three sideband interactions: QQ red  $|eg\rangle \leftrightarrow |ge\rangle$ , QR1 red  $|e0\rangle \leftrightarrow |g1\rangle$ , and QR2 blue  $|g0\rangle \leftrightarrow |e1\rangle$  with rates  $\{\Omega, W_3, W_4\}$  and frequency detunings  $\{\delta, (\Delta + \delta)/2, (\Delta - \delta)/2\}$  respectively. Under this condition, four resonant interactions will appear:  $|gg00\rangle \leftrightarrow |\Phi_{\theta 01}\rangle$ ,  $|ee00\rangle \leftrightarrow |\Phi_{\theta 10}\rangle$ ,  $|ee01\rangle \leftrightarrow |\Phi_{\theta - \pi 00}\rangle$ , and  $|gg10\rangle \leftrightarrow |\Phi_{\theta - \pi 00}\rangle$ . The detuning similarly sets the blending angle  $\theta = \arctan\left(\frac{\delta + \Delta}{\Omega}\right)$ .

With the above construction, we create a stabilization protocol that can freely tune the blending angles. As a special case, when QQ sideband detuning  $\delta = 0$ , the blending angle for both cases is  $\theta = \frac{\pi}{2}$ , which corresponds to the odd and even parity Bell states  $|\Phi_-\rangle = (|ge\rangle - |eg\rangle)/\sqrt{2}$  and  $|\Psi_-\rangle = (|gg\rangle - |ee\rangle)/\sqrt{2}$ , shown in Fig. 4.14(c).

In fact, this stabilization protocol can be generalized to stabilize an even larger group of states, including both entangled and product states, as long as the energy matching requirement  $E_D + E_A = E_B + E_C$  is satisfied when engineering  $H_{QQ}$ . The following is a list of tunable parameters to engineer  $H_{QQ}$ : QQ sideband strength  $\Omega$ , QQ sideband detunings  $\delta$ , single qubit Rabi drive strength, and single qubit Rabi drive detunings. Corresponding stabilized state  $|A\rangle$  is determined from  $H_{QQ}$ . Details about the stabilizable manifold are discussed in Section. 4.3.4.

### 4.3.2 Stabilization Experiments

We perform the stabilization experiment in a system with two transmons capacitively coupled to two lossy resonators (See Section. 4.1). Two transmons are inductively coupled through a SQUID loop. All QQ sidebands and QR red sidebands are realized by modulating the SQUID flux at corresponding transition frequencies. QR blue sidebands are achieved by sending a charge drive to the transmon at half the transition frequencies. The experimentally measured qubit coherence are  $T_1 = 24.3 \mu\text{s}$  ( $9.1 \mu\text{s}$ ),  $T_{\text{Ram}} = 15.2 \mu\text{s}$  ( $9.8 \mu\text{s}$ ),  $T_{\text{echo}} = 24.6 \mu\text{s}$  ( $14.3 \mu\text{s}$ ) for  $Q_1(Q_2)$ , and the measured resonator decay rate  $\kappa/2\pi$  are  $\{0.33, 0.43\}$  MHz for  $R_1$  and  $R_2$  respectively.

Figure 4.15 shows the time evolution of state fidelity for the odd and even parity Bell state stabilization. To stabilize  $|\Psi_-\rangle$ , a  $\Omega = 2\pi \times 2.0$  MHz QQ blue sideband,  $W_1 = W_2 = 2\pi \times 0.47$  MHz QR blue sidebands are simultaneously applied to the system. Both QR sidebands are detuned by  $\Omega/2 = 2\pi \times 1.0$  MHz in frequency to implement the stabilization scheme depicted in Fig. 4.14(c). For each stabilization experiment, we reconstruct the system density matrix through two-qubit state tomography using 5000 repetitions of 9 different pre-rotations. The stabilization fidelity measured at  $49 \mu\text{s}$  (much longer than single qubit  $T_1$  and  $T_{\text{Ram}}$ ) is 82.5%. To stabilize  $|\Phi_-\rangle$ , a  $\Omega = 2\pi \times 3.0$  MHz QQ red sideband,  $W_1 = W_2 = 2\pi \times 0.36$  MHz QR1 red and QR2 blue sidebands are simultaneously applied to the system, with both QR

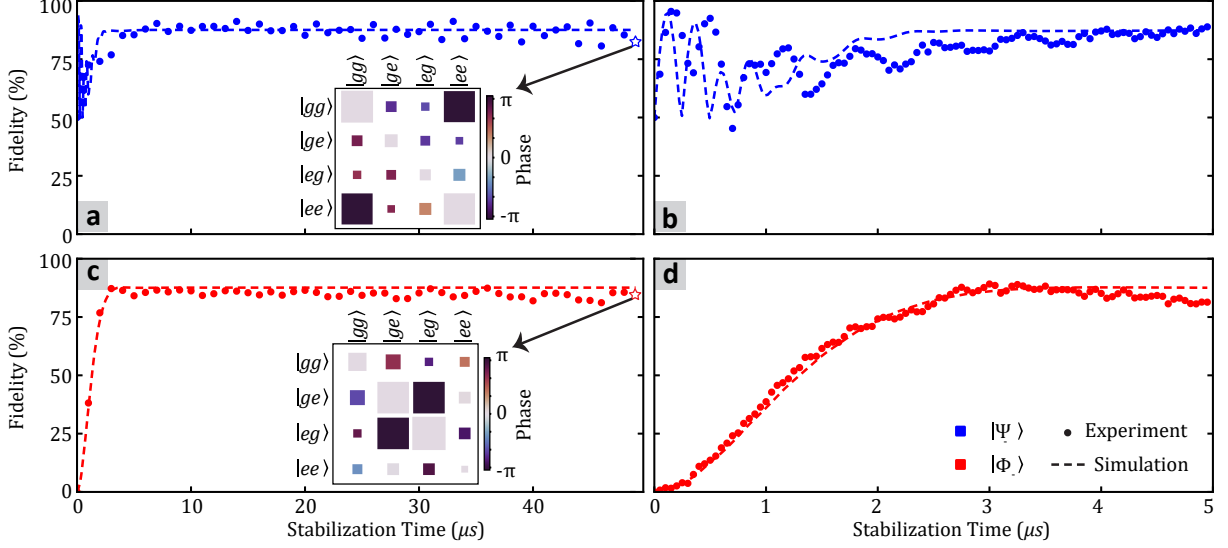


Figure 4.15: **Experimental stabilization of different Bell states.** Experimental demonstration of  $|\Psi_{-}\rangle$  (a, b) and  $|\Phi_{-}\rangle$  (c, d) stabilization with the initial state  $|gg\rangle$ . Two-qubit state tomography is performed at each time point, and the reconstructed density matrix is used to calculate the target state fidelity. The density matrices reconstructed with 5000 single shot measurements at  $49\ \mu\text{s}$  are plotted. Lab frame simulation results are shown in dash lines, matching well in short and long time scales. Parameters used in simulation:  $\{\Omega, W_1, W_2, \Gamma_1, \Gamma_2\}/2\pi = \{2.0, 0.47, 0.47, 0.33, 0.43\}$  MHz for  $|\Psi_{-}\rangle$  and  $\{3.0, 0.36, 0.36, 0.33, 0.43\}$  MHz for  $|\Phi_{-}\rangle$ . Qubit coherence time is chosen as  $\{T_1^{q1}, T_1^{q2}, T_\phi^{q1}, T_\phi^{q2}\} = \{25, 12, 25, 25\}$   $\mu\text{s}$ . Error bars (one standard deviation) are smaller than the marker size [24].

sidebands detuned by  $\Omega/2 = 2\pi \times 1.5$  MHz. The stabilization fidelity measured at  $49\ \mu\text{s}$  is 84.6%. The two-qubit state tomography data at  $49\ \mu\text{s}$  after  $ZZ$  coupling correction [76] are shown for both stabilization cases. Fidelities are calculated as  $F = (\text{tr} \sqrt{\sqrt{\rho}\sigma\sqrt{\rho}})^2$ , where  $\sigma$  is the target state and  $\rho$  is the tomography reconstructed density matrix. Error bars (one standard deviation) for all expectation values calculated from the Maximum Likelihood Estimation(MLE) reconstructed density matrix use the Tomographer package [24].

Next, we introduce QQ sideband detunings  $\delta$  and stabilize more general entangled states  $|\Psi_\theta\rangle$  and  $|\Phi_\theta\rangle$ . We choose the same sideband strengths ( $\{\Omega, W_1, W_2\}/2\pi = \{2.0, 0.47, 0.47\}$  ( $\{3.0, 0.36, 0.36\}$ ) MHz for  $|\Psi_\theta\rangle$ ( $|\Phi_\theta\rangle$ ) case) and detune QR sideband frequencies accordingly to maximize the stabilization fidelity measured at  $40\ \mu\text{s}$ . The experimentally measured

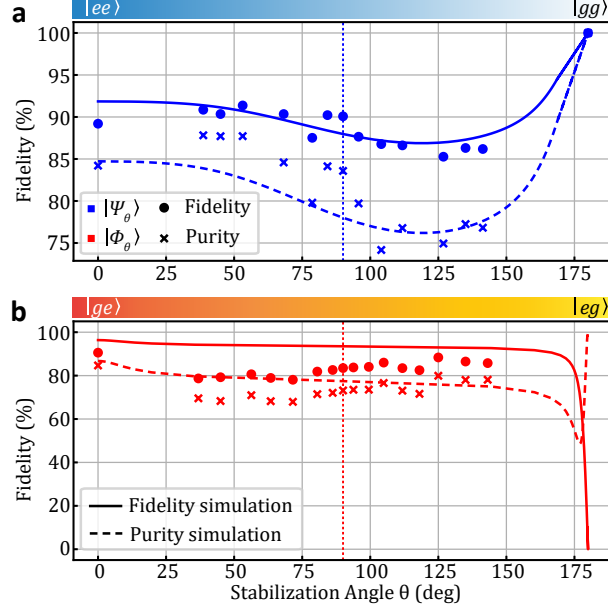


Figure 4.16: **Spectroscopy of universal Bell-state stabilization.**  $|\Psi_\theta\rangle$  (a) and  $|\Phi_\theta\rangle$  (b) are separately stabilized with a measured fidelity above 78% among different blending angle  $\theta$ . The fidelities are measured after 40  $\mu\text{s}$  of stabilization. No external drives are applied for stabilizing  $|gg\rangle$ . For  $|\Phi_\theta\rangle$  case, the fidelity dropped to 0 near  $\theta = \pi$ . The dotted lines indicate simulated fidelities for the odd and even parity Bell state stabilization. All parameters used in the simulation are the same as in Fig. 4.15. Error bars (one standard deviation) are smaller than the marker size [24].

state fidelity and state purity as a function of  $\theta$  are shown in Fig. 4.16. Under the current QR sideband color combination,  $|\Phi_\theta\rangle$  fails to stabilize near  $\theta = 180^\circ$ . This is because the interaction strength  $\langle gg00| H_{\text{sys}} |\Phi_\theta 01\rangle$  and  $\langle ee00| H_{\text{sys}} |\Phi_\theta 10\rangle$  are close to 0. Swapping QR1 and QR2 sidebands' color and detuning performs a transformation  $\theta \rightarrow \theta - \pi$  in the stabilized state. This ensures a high stabilization fidelity for arbitrary stabilization angles. Details about changing sideband colors and detunings to ensure high fidelity are presented in Section. 4.3.4.

The flexibility in our schemes and easy access to different sidebands in our device allow a further demonstration — fast dissipative switching between stabilized states. Here, we implement such an operation that can flip the parity of the stabilized Bell pair by changing sideband combinations, shown in Fig. 4.14. To quantify the stabilized parity, we measure the

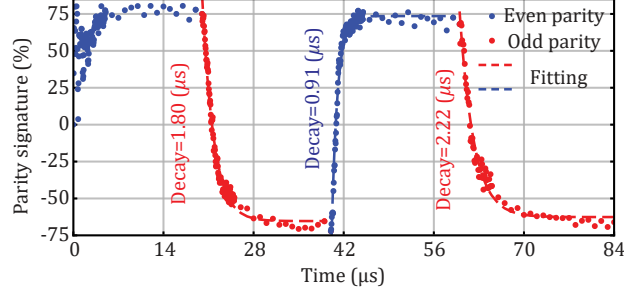


Figure 4.17: **Dissipative switching of Bell state parity.** The initial state is  $|gg\rangle$ , and the switch status is set to even parity between  $[0 \mu\text{s}, 20 \mu\text{s}]$  and  $[40 \mu\text{s}, 60 \mu\text{s}]$ , and to odd parity between  $[20 \mu\text{s}, 40 \mu\text{s}]$  and  $[60 \mu\text{s}, 85 \mu\text{s}]$ . Each experimental point is measured with the two-qubit state tomography. Stabilization time is calculated by fitting the parity signature to exponential decay after each switching event.

system's density matrix  $\rho$  and define the parity signature as  $2(|\langle ee|\rho|gg\rangle| - |\langle ge|\rho|eg\rangle|)$  describing the difference in relevant coherence parameters. The results are shown in Fig. 4.17. The scaling factor is chosen such that the ideal even and odd Bell pairs have parity signatures of  $\pm 1$ . Starting from the ground state  $|Q_1Q_2\rangle = |gg\rangle$ , the stabilized state is set to even parity Bell pair  $(|gg\rangle - |ee\rangle)/\sqrt{2}$ , and we switch the parity every  $20 \mu\text{s}$ . At  $20 \mu\text{s}$ , the stabilized state is switched to odd parity Bell pair  $(|ge\rangle - |eg\rangle)/\sqrt{2}$ , and stabilization happens quickly with a time constant  $\tau_r = 1.8 \mu\text{s}$ . At  $40 \mu\text{s}$ , the switching from odd to even parity results in a faster stabilization with  $\tau_b = 0.91 \mu\text{s}$ . The switching at  $60 \mu\text{s}$  to odd Bell state shows a similar  $\tau_r$  of  $2.20 \mu\text{s}$ . We leave the stabilization drives turned on for another  $25 \mu\text{s}$  to prove that the performance is not degraded after a few switching operations.

Further improvement of the stabilized state's fidelity is possible by reducing the transition ratio  $\frac{\gamma}{\Gamma_t}$  and increasing QQ sideband rate  $\Omega$  for a larger energy gap. Increasing qubit dephasing time also improves stabilization fidelity. To speed up the stabilization, i.e., reduce time constants, we need to increase the refilling rate  $\Gamma_t$ . Since QR sideband rate  $W$  is bounded by the QQ sideband rate  $\Omega$  to ensure the validity of the perturbative approximation, given a fixed  $W$ ,  $\Gamma_t$  is maximized when the resonator decay rate  $\kappa = W \cos(\theta/2)$ . For the even and odd parity Bell states, further increase in both resonators'  $\kappa$  compared to our current

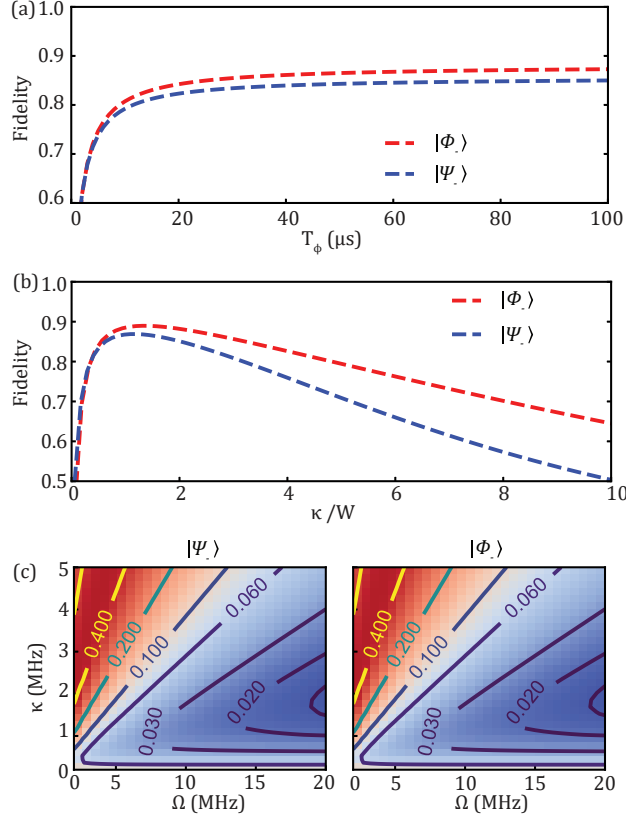


Figure 4.18: Rotating frame simulation of even and odd parity bell states' stabilization fidelity: (a) Sweeping qubit dephasing time. The other simulation parameters are the same as the experiments. (b) Sweeping the ratio between resonator decay rate  $\kappa$  and QR sideband strength  $W$  without qubit dephasing. (c) 2D sweep of  $\kappa$  and QQ sideband strength  $\Omega$  without qubit dephasing, setting  $W = \kappa$ . Infidelities are shown on the contours.

parameters would thus be beneficial.

### 4.3.3 Stabilization Robustness

We study the stabilization robustness for  $|\Psi_-\rangle$  and  $|\Phi_-\rangle$  in this section. For other stabilization angles, the discussion is similar. Fig. 4.18 shows the rotating frame simulation of steady-state fidelity by sweeping different stabilization parameters. For the  $|\Psi_-\rangle$  case, the Hamiltonian used in the simulation is Eq. (1) in the main text, and for the  $|\Phi_-\rangle$  case the Hamiltonian is modified accordingly with a different sideband combinations (See Fig. 4.14(c)). We study the state fidelity by varying parameters step-by-step towards the ideal case. First, we show

that longer qubit dephasing time helps improve steady-state fidelity. In Fig. 4.18 (a), we sweep qubit's dephasing time (assuming the same for both qubits) while choosing the following parameters  $\{\Omega, \frac{W_1}{2}, \frac{W_2}{2}, \Gamma_1, \Gamma_2\}/2\pi$  in the simulation

$$\begin{aligned} |\Psi_-\rangle \text{ case} &: \{1.4, 0.35, 0.35, 0.30, 0.33\} \text{MHz}, \\ |\Phi_-\rangle \text{ case} &: \{3.0, 0.32, 0.32, 0.30, 0.33\} \text{MHz}. \end{aligned}$$

We set the following qubit decoherence time  $\{T_1^{q1}, T_1^{q2}\} = \{21, 9\} \mu\text{s}$ . The steady state fidelities rise above 80% quickly after  $T_\phi$  exceeds 10  $\mu\text{s}$ . The fidelity for odd and even parity bell pairs saturate at 87.3% and 85.0% with the parameters used in the simulation. This demonstrates that steady-state fidelity increases as qubit dephasing time increases.

In Fig. 4.18(b), we ignore the qubit dephasing and only sweep resonator decay rate  $\kappa$ . For simplicity, we assume QR sideband rates and resonator decay rate are the same:  $W_1 = W_2 = W$  and  $\kappa_1 = \kappa_2 = \kappa$ . The fidelity peak for both parity pairs appears at  $W = \kappa$ . This can be understood as the refilling rate  $\Gamma_t$  (Eq. (2) in the main text) achieves the maximum at this point, therefore the steady-state fidelity (Eq. (3) in the main text) is also maximized at this point.

Finally, we choose the maximum refilling rate set  $W = \kappa$  in Fig. 4.18(c) and sweep both the QQ sidebands rate  $\Omega$  and resonator decay rate  $\kappa$ . The infidelity of the steady states is shown in contours. Larger  $\Omega$  and  $\kappa$  suppresses the infidelity efficiently. This indicates that our steady-state fidelity in the experiment is mainly limited by the sideband strengths. By increasing the QQ sidebands rate to above  $2\pi \times 10$  MHz, in simulation, it is possible to achieve stabilization fidelity above 98%.

We further investigate the impact of stray ZZ coupling between transmons on stabilization fidelity. This analysis uses the even and odd parity Bell states  $|\Phi_-\rangle$  and  $|\Psi_-\rangle$  as examples. We choose the following parameters  $\{\Omega, \frac{W_1}{2}, \frac{W_2}{2}, \Gamma_1, \Gamma_2\}/2\pi$  in the simulation (the same as the experimental measurements).

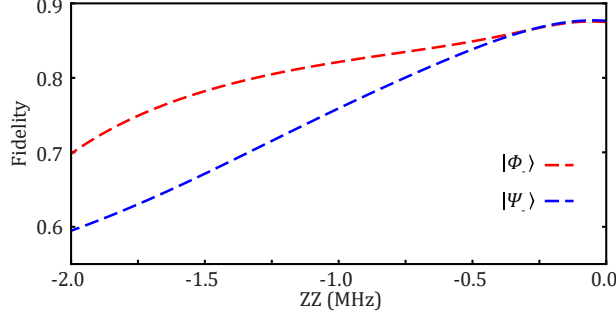


Figure 4.19: Steady state stabilization fidelity under various stray ZZ interactions between qubits. For  $|\Psi_{-}\rangle$  ( $|\Phi_{-}\rangle$ ), we choose the QQ sideband detunings as  $\delta = -ZZ(0)$  for maximum stabilization fidelity.

$$|\Psi_{-}\rangle \text{ case : } \{2.0, 0.47, 0.47, 0.33, 0.43\} \text{ MHz,}$$

$$|\Phi_{-}\rangle \text{ case : } \{3.0, 0.36, 0.36, 0.33, 0.43\} \text{ MHz.}$$

The  $Q_1(Q_2)$  coherence used in the simulation are  $\{T_1, T_\phi\} = \{25(12), 25(25)\} \mu\text{s}$ . In the presence of ZZ coupling  $\eta$ , the energy matching requirement  $E_A + E_D = E_B + E_C$  is no longer satisfied. The mismatch in energy  $\eta$  reduces the two-step refilling rate  $\Gamma'_t = \frac{W^2 \cos^2(\theta/2) \kappa}{\kappa^2 + W^2 \cos^2(\theta/2) + \eta^2}$ .

Therefore, stabilization fidelity decreases as the strength of the ZZ coupling increases. However, when the ZZ coupling strength is less than the QR sideband rate  $W$ , the refilling rate remains relatively unaffected by changes in  $\eta$ . As shown in Fig. 4.19, the stabilization fidelity does not significantly decrease for  $ZZ > -0.3$  MHz. Notably, the static ZZ coupling measured in our experiments is  $-0.261$  MHz, which falls within this acceptable range.

#### 4.3.4 Other stabilization combinations

Here we provide a list of states that can be stabilized with our protocol.

Case 1: Any two-qubit product states.

$$|\psi_{\phi_1, \phi_2}\rangle = (\cos(\phi_1/2) |g\rangle + \sin(\phi_1/2) |e\rangle) \otimes (\cos(\phi_2/2) |g\rangle + \sin(\phi_2/2) |e\rangle). \quad (4.36)$$

This can be achieved by applying two detuned single qubit rabi drives on both  $Q_1$  and  $Q_2$  with rate  $\{A_1, A_2\}$  and detunings  $\{\delta_1, \delta_2\}$ . The two-qubit rotating frame Hamiltonian becomes

$$H_p = \begin{bmatrix} 0 & A_2/2 & A_1/2 & 0 \\ A_2/2 & \delta_2 & 0 & A_1/2 \\ A_1/2 & 0 & \delta_1 & A_2/2 \\ 0 & A_1/2 & A_2/2 & \delta_1 + \delta_2 \end{bmatrix}. \quad (4.37)$$

It can be easily verified that the four eigenenergies  $\{E_A < E_B < E_C < E_D\}$  satisfy the requirements  $E_A + E_D = E_B + E_C$ . Therefore, the lowest energy eigenstate can be efficiently stabilized by detuning two QR sideband frequencies. This is also a direct extension of the single-qubit stabilization scheme [55] to the two-qubit case.

Case 2: Dressed parity Bell states. The stabilized state set can be described by one continuous variable  $\theta_1$

$$|\zeta_{\theta_1}\rangle = \cos(\theta_1/2) |\Psi_-\rangle + \sin(\theta_1/2) |\Phi_-\rangle. \quad (4.38)$$

In this case, we apply on-resonant QQ blue and single qubit rabi drive on  $Q_1$  with rate  $\Omega$  and  $A_1$  to dress the stabilized state's parity. The two-qubit Hamiltonian  $H_b$  can be written

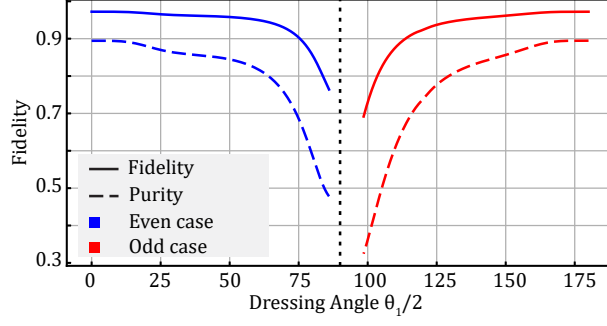


Figure 4.20: Stabilizing a one-dimensional set of entangled states. Blue and red lines represent separately using the QQ blue and QQ red sideband in the rotating frame simulation. Parameter used in the simulation:  $\{\Omega, W_1, W_2, \kappa_1, \kappa_2\}/2\pi = \{5.0, 0.5, 0.5, 0.3, 0.33\}$  MHz. Qubit coherence time are  $\{T_1, T_\phi\} = \{30, 30\}\mu\text{s}$ .

as

$$H_b = \begin{bmatrix} 0 & 0 & A_1/2 & \Omega/2 \\ 0 & 0 & 0 & A_1/2 \\ A_1/2 & 0 & 0 & 0 \\ \Omega/2 & A_1/2 & 0 & 0 \end{bmatrix}. \quad (4.39)$$

One can verify that the four eigenenergies  $E_A < E_B < E_C < E_D$  of  $H_b$  satisfy the requirement  $E_A + E_D = E_B + E_C$ . By choosing QR sidebands detunings as  $E_B - E_A$  and  $E_C - E_A$ , the eigenstate  $|A\rangle = |\zeta_{\theta_1}\rangle$  is stabilized, with the dressing angle being

$$\theta_1 = 2 \arctan \left( \frac{2A_1}{\Omega + \sqrt{4A_1^2 + \Omega^2}} \right). \quad (4.40)$$

Similarly, we apply on-resonant QQ red sideband and single qubit rabi drive on  $Q_1$  with

rate  $\Omega$  and  $A_1$ . The two-qubit Hamiltonian  $H_r$  is

$$H_r = \begin{bmatrix} 0 & 0 & A_1/2 & 0 \\ 0 & 0 & \Omega/2 & A_1/2 \\ A_1/2 & \Omega/2 & 0 & 0 \\ 0 & A_1/2 & 0 & 0 \end{bmatrix}. \quad (4.41)$$

The dressing angle  $\theta_1$  under this case is

$$\theta_1 = \pi - 2 \arctan \left( \frac{2A_1}{\Omega + \sqrt{4A_1^2 + \Omega^2}} \right). \quad (4.42)$$

Steady-state fidelity is calculated through Qutip simulation for both cases, shown in Fig. 4.20. By combining different QQ sideband colors, all dressing angles are stabilized with the scheme, except the small band region around  $\theta_1 = \pi$  where the effective transition rates provided by QR sidebands are close to 0.

Case 3: Rabi-dressed entangled states. This is a more general case where a two-dimensional set of entangled states is stabilized. We simultaneously apply a single qubit rabi drive on  $Q_1$  with the rate  $A_1$  and detuned QQ blue sideband with rate  $\Omega$  and detuning  $\delta$ . The rotating frame Hamiltonian is

$$H_g = \begin{bmatrix} -\delta/2 & 0 & A_1/2 & \Omega/2 \\ 0 & \delta/2 & 0 & A_1/2 \\ A_1/2 & 0 & -\delta/2 & 0 \\ \Omega/2 & A_1/2 & 0 & \delta/2 \end{bmatrix}. \quad (4.43)$$

The four eigenenergies of the Hamiltonian can also be grouped into two pairs sharing the same sum. By appropriately choosing two QR sideband detunings, the lowest energy eigenstate is

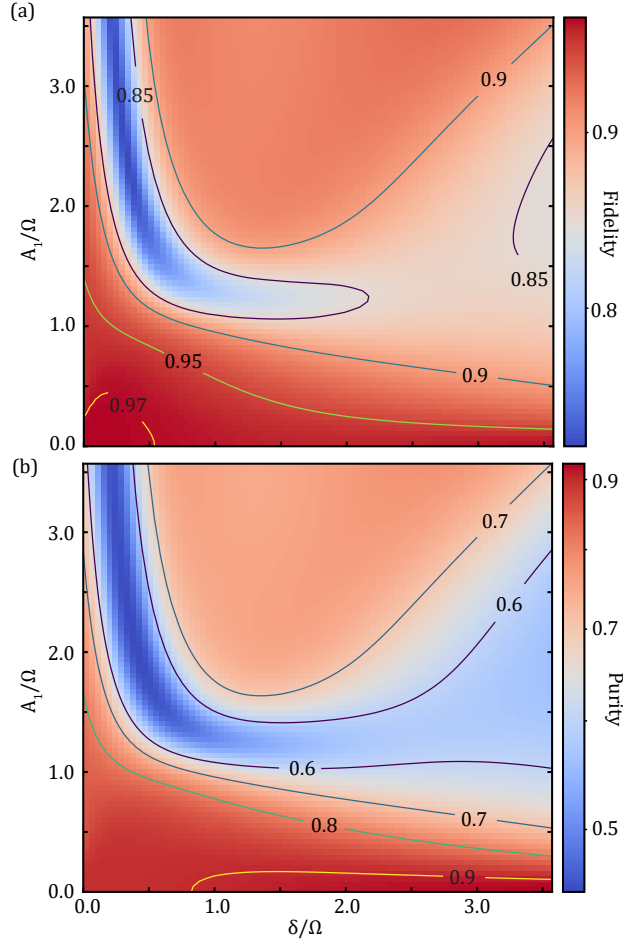


Figure 4.21: Stabilizing a 2D set of entangled states. Steady states' fidelity (a) and purity (b) are simulated in the rotating frame and plotted.  $\frac{A_1}{\Omega}$  and  $\frac{\delta}{\Omega}$  are separately two free variables that are swept to stabilize different states. Parameter used in the simulation:  $\{\Omega, W_1, W_2, \kappa_1, \kappa_2\}/2\pi = \{5.0, 0.5, 0.5, 0.3, 0.33\}$  MHz. Qubit coherence time are  $\{T_1, T_\phi\} = \{30, 30\}$   $\mu$ s.

stabilized

$$\begin{aligned}
|\xi_{\delta, A_1}\rangle &= E_{00} |gg\rangle + E_{01} |ge\rangle + E_{10} |eg\rangle - |ee\rangle, \\
x &= \sqrt{4\delta^2 A_1^2 + 4A_1^2 \Omega^2 + \Omega^4}, \\
y &= \sqrt{\delta^2 + 2(2A_1^2 + \Omega^2 + x)}, \\
E_{00} &= \frac{(\delta - y)(\delta^2 + \Omega^2 + x + \delta y)}{2\Omega(2A_1^2 + \Omega^2 + x)}, \\
E_{01} &= \frac{A_1(\delta - y)}{2A_1^2 + \Omega^2 + x}, \\
E_{10} &= -\frac{A_1(\delta^2 + \Omega^2 + x + \delta y)}{\Omega(2A_1^2 + \Omega^2 + x)}. \tag{4.44}
\end{aligned}$$

For brevity, the stabilized state  $|\xi_{\delta, A_1}\rangle$  is not normalized. The form of the state is determined by two independent variables  $\frac{\delta}{\Omega}$  and  $\frac{A_1}{\Omega}$ . We sweep these two variables and plot the simulated fidelity and purity in Fig. 4.21. This a general map covering all stabilized entangled states in the programmable operation: the vertical cut  $\frac{\delta}{\Omega} = 0$  represents the blue line in case 2 Dressed parity Bell states, the horizontal cut  $\frac{A_1}{\Omega} = 0$  represents the stabilized states shown in Fig. 1(b) in the main text, and the bottom left point  $(\frac{\delta}{\Omega}, \frac{A_1}{\Omega}) = (0, 0)$  is the even parity bell state  $|\Psi_{-}\rangle$ . Using a modest sideband rate combination, most of the states on the plot can be stabilized with fidelity over 90%. Correspondingly, changing the QQ sideband color to red can stabilize another 2D set of entangled states, which are dual to this case. All possible programmable stabilization operations can be chosen accordingly through the map provided here. States with both  $E_{01} > 1$  and  $E_{10} > 1$  cannot be stabilized under this case for instance.

Changing sideband colors and detuning frequency signs stabilize different states. This is important for stabilizing  $|\Psi_{\theta}\rangle$  and  $|\Phi_{\theta}\rangle$ : at certain blending angles, the steady state fidelity is low because of the low effective refilling rate  $\Gamma_t$

As an explicit example, we consider the  $|\Psi_{\theta}\rangle$  stabilization case. Instead of using two QR

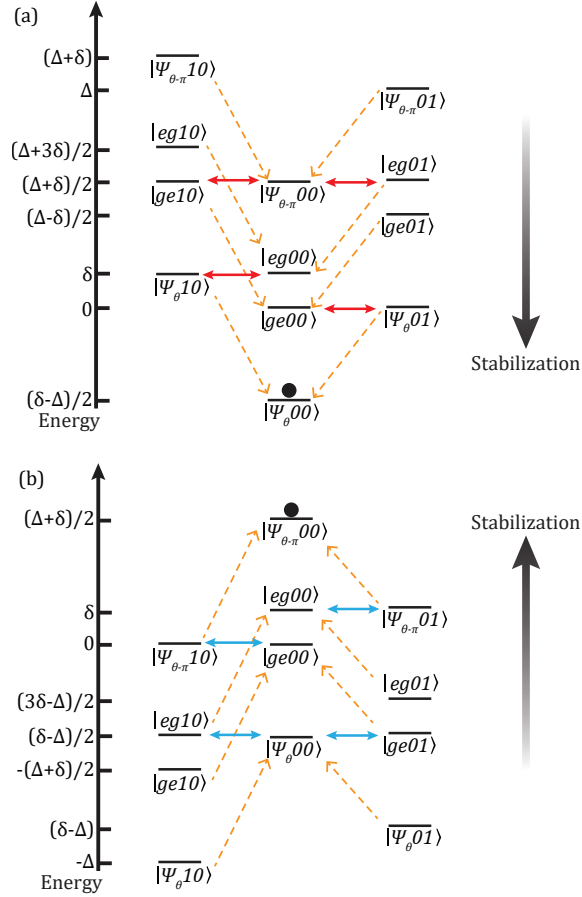


Figure 4.22: (a) Use both QR red sidebands to stabilize  $|\Psi_\theta\rangle$ . (b) Use opposite QR blue sideband detunings to stabilize  $|\Psi_{\theta-\pi}\rangle$ . The QQ sideband rates and detunings are separate  $\Omega$  and  $\delta$ , and the QR sideband is detuned in frequency by  $\frac{\Delta+\delta}{2}$ ,  $\frac{\Delta-\delta}{2}$  in (a) and  $-\frac{\Delta+\delta}{2}$ ,  $-\frac{\Delta-\delta}{2}$  in (b). Here  $\Delta = \sqrt{\Omega^2 + \delta^2}$ .

blue sidebands, we use two QR red sidebands with the same detuning and sideband rate. The rotating frame Hamiltonian now becomes

$$\begin{aligned}
H_{\text{color}} = & \frac{\Omega}{2} (a_{q1}a_{q2} + h.c.) + \delta a_{q1}^\dagger a_{q1} \\
& + \frac{W_1}{2} (a_{q1}^\dagger a_{r1} + h.c.) + \frac{W_2}{2} (a_{q2}^\dagger a_{r2} + h.c.) \\
& + \frac{\Delta + \delta}{2} a_{r1}^\dagger a_{r1} + \frac{\Delta - \delta}{2} a_{r2}^\dagger a_{r2}.
\end{aligned} \tag{4.45}$$

Fig. 4.22 (a) shows the level diagram, where the QR red sidebands now connect  $|ge00\rangle$  to  $|\Psi_{\theta}01\rangle$ , which is different from the QR blue sidebands case where  $|ge00\rangle$  and  $|\Psi_{\theta}10\rangle$  are connected. The two-step refilling rate  $\Gamma_{tc}$  for  $|ge00\rangle \rightarrow |\Psi_{\theta}00\rangle$  is

$$\Gamma_{tc} = \frac{W^2 \sin^2(\theta/2) \kappa}{\kappa^2 + W^2 \sin^2(\theta/2)}. \tag{4.46}$$

The other three two-step transitions  $|eg00\rangle \rightarrow |\Psi_{\theta}00\rangle$ ,  $|\Psi_{\theta-\pi}00\rangle \rightarrow |ge00\rangle$ , and  $|\Psi_{\theta-\pi}00\rangle \rightarrow |eg00\rangle$  have the same refilling rate. Therefore, the steady-state fidelity for  $|\Psi_{\theta}\rangle$  is

$$\mathcal{F}_{\infty} = \left( \frac{\Gamma_t + \gamma \cos^2(\theta/2)}{\Gamma_t + \gamma} \right)^2. \tag{4.47}$$

One can thus choosing the QR sideband color for higher  $F_{\infty}$ . When the  $F_{\infty}$  drops significantly near  $\theta = \pi$  for  $\Phi_{\theta}$  stabilization case, one can flip the QR sideband color for better performance.

We can also keep the same QR sideband color while choosing opposite QR sideband

detunings. The Hamiltonian becomes

$$\begin{aligned}
H_{\text{opp}} = & \frac{\Omega}{2} (a_{q1}a_{q2} + h.c.) + \delta a_{q1}^\dagger a_{q1} \\
& + \frac{W_1}{2} (a_{q1}^\dagger a_{r1} + h.c.) + \frac{W_2}{2} (a_{q2}^\dagger a_{r2} + h.c.) \\
& - \frac{\Delta + \delta}{2} a_{r1}^\dagger a_{r1} - \frac{\Delta - \delta}{2} a_{r2}^\dagger a_{r2}.
\end{aligned} \tag{4.48}$$

The level diagram is shown in Fig. 4.22 (b). All population flows to  $|\Psi_{\theta-\pi}\rangle$ , with the same refilling rate and steady-state fidelity as the  $|\Psi_\theta\rangle$  case.

### 4.3.5 Error Analysis

To accurately simulate the real system, we sequentially introduce several error channels. After each addition, we calculate its contribution to infidelity by measuring the difference in the steady-state fidelity. We use the states  $|\Phi_-\rangle$  and  $|\Psi_-\rangle$  as examples, with results detailed in Table 4.8.

Initially, in an ideal case, decoherence-free simulations are conducted within a Hamiltonian of dimension  $2 \times 2 \times 2 \times 2$  (two levels per resonator), resulting in infidelities of 1.71% and 4.98% respectively. Subsequently, transmon  $T_1$  and  $T_\phi$  are incorporated into the system, revealing that transmon decoherence accounts for the majority of the stabilization infidelity observed in experiments. A higher transmon level is then added, extending the Hamiltonian to a dimension of  $3 \times 3 \times 2 \times 2$ . The contribution of transmon  $ZZ$  coupling to the stabilization infidelities is found to be less than 1%. Other error channels contribute minimally, such as leakage to the  $|f\rangle$  state and inaccuracies in sideband frequency calibration. The discrepancy between the theoretically predicted and experimentally measured state fidelities is primarily attributed to the thermal excitation rate in the transmons when all sidebands are active. An excitation rate of 0.9 ms in both transmons sufficiently explains these deviations in the simulation.

Stabilized state infidelity	$ \Phi_{-}\rangle$	$ \Psi_{-}\rangle$
Ideal implementation	1.71%	4.98%
Transmon $T_1$	7.56%	5.25%
Transmon dephasing	3.14%	2.21%
$ f\rangle$ state leakage	$\sim 0.1\%$	$\sim 0.1\%$
$ZZ$ interactions	0.85%	0.98%
Thermal excitation*	$\sim 2.0\%$	$\sim 2.0\%$
QR frequency mismatch <sup>†</sup>	$< 0.18\%$	$< 0.57\%$
QQ frequency mismatch <sup>†</sup>	$< 0.1\%$	$< 0.1\%$
Total predicted fidelity	$\sim 15.64\%$	$\sim 16.19\%$
Experimental infidelity	15.4%	17.5%

Table 4.8: **Infidelity channels for odd and even parity Bell states stabilization.**

\* The transmon excitation rate is approximately 0.9 ms, as inferred from the residual infidelities observed in the experiments.

<sup>†</sup> Frequency mismatch are assumed to be at most 20kHz.

## CHAPTER 5

### AUTONOMOUS QUANTUM ERROR CORRECTION

Large-scale quantum computers will inevitably need quantum error correction to protect information against decoherence. Traditional error correction typically requires many qubits, along with high-efficiency error syndrome measurement and real-time feedback. Autonomous quantum error correction instead uses steady-state bath engineering to perform the correction in a hardware-efficient manner. In this section, we implement a new AQEC protocol, called the Star code, that only requires easy-to-realize two-photon interactions. We develop a coherence-preserving two-transmon coupler that can parametrically generate all interactions needed for the protocol. With AQEC turned on, the logical states show higher coherence times than the uncorrected case limited by stray ZZ coupling between transmons. The structure of the Chapter is as follows. First, we explain the circuit implementation of the Star code using the inductively coupled transmons. Then, we experimentally calibrate each parametric process used in the code. Finally, we prepare the logical states and characterize the coherence improvement.

#### 5.1 Device implementation and sideband calibration

The Star code encodes a logical qubit using two orthogonal states in a nine-dimensional (two-qutrit) Hilbert space as  $|L_0\rangle = (|gf\rangle - |fg\rangle)/\sqrt{2}$  (logical “zero”), and  $|L_1\rangle = (|gg\rangle - |ff\rangle)/\sqrt{2}$  (logical “one”) where  $|g\rangle$ ,  $|e\rangle$ , and  $|f\rangle$  represent the lowest three energy levels of a transmon. The error states after a single photon-loss (one transmon in  $|e\rangle$ ) are orthogonal to the logical space and to each other. Further, both logical states have an equal expected photon number so that the single-photon loss (transmon decay) does not reveal information about the state it was emitted from. We engineer a parent Hamiltonian for the logical states through  $|gf\rangle\langle fg|$  and  $|gg\rangle\langle ff|$  parametric processes. These processes are all implemented by driving through

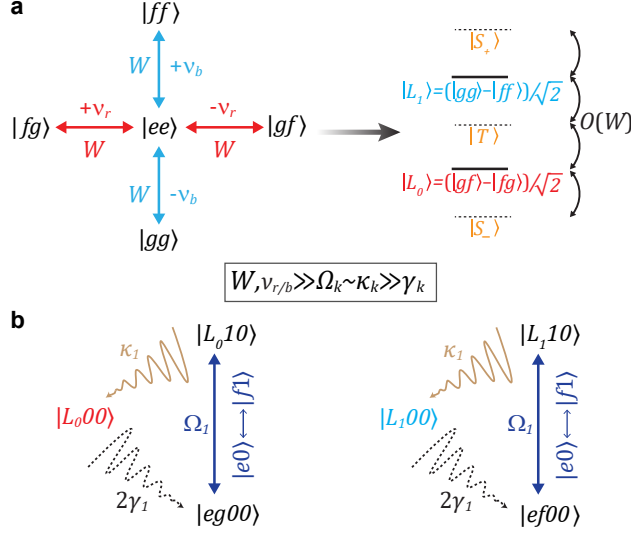


Figure 5.1: **Illustration of the autonomous error-correction scheme.** The protocol requires simultaneous application of two QQ blue sidebands ( $|ee\rangle \leftrightarrow |gg\rangle$  and  $|ee\rangle \leftrightarrow |ff\rangle$ ), two QQ red sidebands ( $|ee\rangle \leftrightarrow |fg\rangle$  and  $|ee\rangle \leftrightarrow |gf\rangle$ ), and two QR error correcting sidebands ( $|e0\rangle \leftrightarrow |f1\rangle$ ). All six drives are always-on. **a** Star code logical word formation. All QQ sidebands have nominally equal rates  $W$ . The two drives within a pair have opposite detunings from the on-resonance values. This opens up the energy gaps of  $O(W)$  between logical states and other states  $\{|S_{\pm}\rangle, |T\rangle\}$  (see Sec. 3.2 for full expression). With only QQ sidebands on, this forms the “QQ echoed” qubit sharing the same logical states as the star code. **b** The AQEC cycle for  $|L_0\rangle$  (left) and  $|L_1\rangle$  (right) when a single-photon-loss event occurs. Logical state  $|L_000\rangle$  ( $|L_100\rangle$ ) loses a photon from transmon  $Q_1$  at a rate  $2\gamma_1$  and becomes the error state  $|eg00\rangle$  ( $|ef00\rangle$ ). QR error correcting sidebands (applied on-resonance) bring the state at rate  $\Omega_1$  to  $|L_010\rangle$  ( $|L_110\rangle$ ) with one photon populating  $R_1$ .  $R_1$ ’s photon decays quickly (at a rate  $\kappa_1$ ) and recovers the original logical state. AQEC cycle for  $Q_2$ ’s photon loss event is similar.

$|ee\rangle$  as an intermediate state, producing the star topology in Hilbert space that gives the code its name (see Fig. 5.1a). An intermediate state allows these to be achieved using only 2-photon drives (QQ sidebands). We use the convention of calling them QQ red (single-photon exchange with low-frequency drives) and blue (two-photon pumping with high-frequency drives) sidebands. Despite both sets of drives going through  $|ee\rangle$ , the logical states can be made dark with respect to  $|ee\rangle$  by detuning the  $|L_0\rangle$  ( $|L_1\rangle$ ) sidebands by  $\pm\nu_r$  ( $\pm\nu_b$ ) and setting equal drive strength  $W$ .

The star code requires engineering a Hamiltonian  $\tilde{H}_{\text{static}}$ , which consists of 4 QQ side-

bands between two transmons and 2 QR blue sidebands between each QR pair:

$$\tilde{H}_{QR1} = \frac{\Omega_1}{2} a_{r1}^\dagger (|fg\rangle \langle eg| + |ff\rangle \langle ef|) \otimes I_4 + h.c., \quad (5.1)$$

$$\tilde{H}_{QR2} = \frac{\Omega_2}{2} a_{r2}^\dagger (|gf\rangle \langle ge| + |ff\rangle \langle fe|) \otimes I_4 + h.c., \quad (5.2)$$

$$\begin{aligned} \tilde{H}_{QQ} = \frac{W}{2} & \left( |ee\rangle \langle gf| e^{2\pi i \nu_r t} + |ee\rangle \langle fg| e^{2\pi i \nu_r t} \right. \\ & \left. + |ee\rangle \langle gg| e^{2\pi i \nu_b t} + |ee\rangle \langle ff| e^{2\pi i \nu_b t} \right) + h.c. \end{aligned} \quad (5.3)$$

$$\tilde{H}_{\text{static}} = \tilde{H}_{QQ} \otimes I_4 + \sum_{j=1,2} \tilde{H}_{QRj} + H_c. \quad (5.4)$$

We label the full state as  $|Q_1 Q_2 R_1 R_2\rangle$  and keep the lowest two levels for each resonator.

Here  $I_n$  is the  $n \times n$  identity matrix.

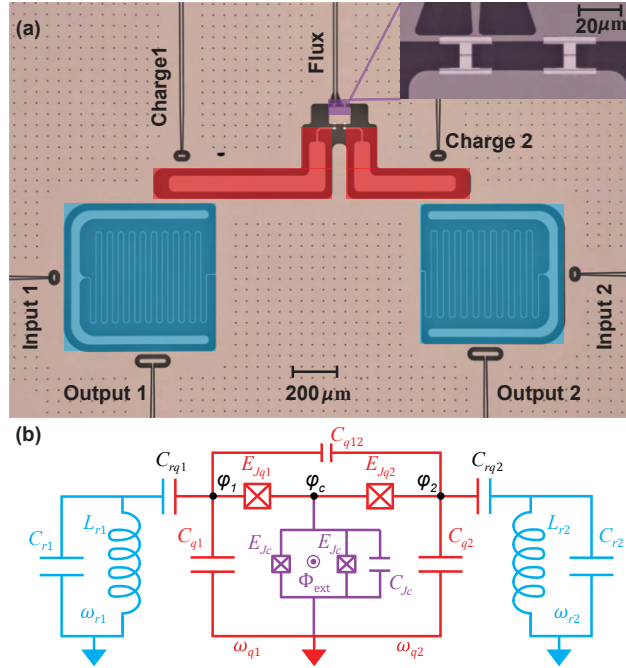


Figure 5.2: The device. (a) False-colored optical image. Two transmons (red) are inductively connected through a SQUID loop (purple, inset shows zoomed-in image). An on-chip flux line is coupled to the SQUID for activating QQ sidebands through parametric RF flux modulation at the proper DC flux position. Each transmon is capacitively coupled to the readout resonator (blue). Single transmon pulses are sent through the resonator input lines. QR sidebands are applied through corresponding charge lines. (b) Circuit schematic diagram.

We realize this protocol using the circuit shown in Fig. 5.2(a). The key component is the inductive coupler based on the design in Ref. [55] that enables the realization of fast parametric interactions. Two transmons  $Q_1$  and  $Q_2$  serve as the qutrits and share a common path to ground. This path is interrupted by a Superconducting Quantum Interference Device (SQUID) loop. The SQUID is a tunable inductor with external DC and RF magnetic fields threaded to activate the QQ sidebands. Each transmon is capacitively coupled to a lossy resonator serving as the readout and cold reservoir. QR sidebands can be performed by sending a charge drive at the half transition frequency to the transmon [88]. Full circuit quantization is shown in Fig. 5.2(b).

We first characterize the individual qubits and realize the required sidebands to create and correct the logical states. We adjust the DC flux point to minimize the Cross-Kerr coupling between transmons which can dephase the logical superposition states (See Sec. 3.4 for further discussion). The measured Cross-Kerr couplings are all lower than 320 kHz while maintaining Ramsey dephasing times  $T_{R_{ge}} = 15.2(9.8) \mu\text{s}$  with relaxation time  $T_{1_{ge}} = 24.3(9.1) \mu\text{s}$ , for  $Q_1(Q_2)$  (See Table. 4.2).

To calibrate the QR sidebands for selective photon pumping, we initialize the system in  $|eg00\rangle$  and apply a continuous charge drive at frequency  $(\omega_{r1} + \omega_{q1} + \alpha_1)/2$  to activate a 2-photon  $|e0\rangle \leftrightarrow |f1\rangle$  transition between  $Q_1$  and  $R_1$  at a rate of 0.49 MHz. The system achieves a steady state  $|fg00\rangle$  within  $3 \mu\text{s}$  as shown by red points in Fig. 5.3(a). Similarly, a 0.59 MHz QR2 drive takes  $|ge00\rangle$  to  $|gf00\rangle$  in a similar time (blue points in Fig. 5.3(a)). The decay of transmon reduces the final average photon number slightly below 2.

We achieve at least 20 MHz QQ red sidebands ( $|j, k\rangle \leftrightarrow |j + 1, k - 1\rangle$ ) and 5 MHz QQ blue sidebands ( $|j, k\rangle \leftrightarrow |j + 1, k + 1\rangle$ ) separately at the operating point, demonstrating a fast, coherence-preserved two-qutrit coupler with suppressed  $ZZ$  interaction. Blue sidebands have a slower rate limited by stray signals from higher flux modulation frequencies (See discussion in Sec. 5.3).

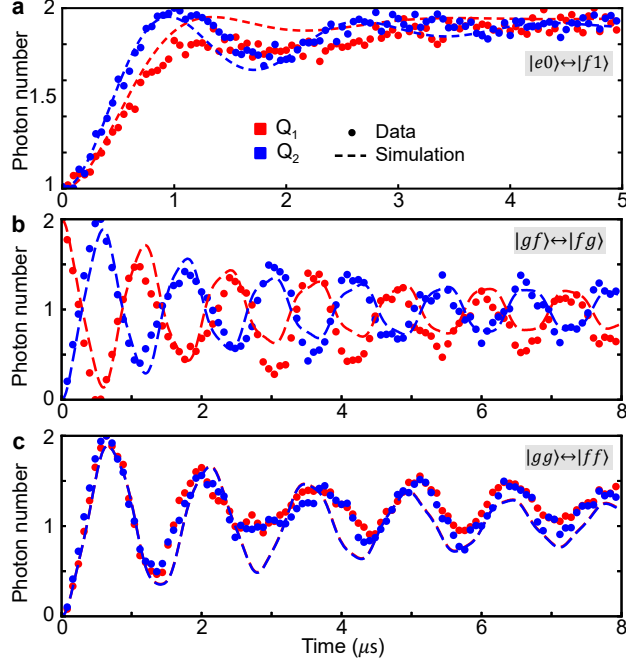


Figure 5.3: **Different parametric oscillations.** Photon numbers in individual transmons are measured as a function of time. **a** Error correcting QR sidebands  $|e0\rangle \leftrightarrow |f1\rangle$  applied separately at rates  $\Omega_1 = 0.49$  MHz and  $\Omega_2 = 0.59$  MHz to the transmon-resonator pairs with  $|e\rangle$  as initial states. Effective transitions **b**  $|gf\rangle \leftrightarrow |fg\rangle$  and **c**  $|gg\rangle \leftrightarrow |ff\rangle$  are measured when all QQ and QR sidebands are simultaneously turned on. Extracted sideband rates and detunings from simulation are  $W_r = 1.45$  MHz,  $W_b = 1.25$  MHz,  $\nu_r = 0.8$  MHz,  $\nu_b = -0.9$  MHz,  $\Omega_1 = \Omega_2 = 0.39$  MHz. Other parameters are based on experimentally measured data shown in Table. 4.3. Oscillation distortions qualitatively match the lab frame simulations (dashed lines). Measurement errors are smaller than the marker size.

By driving all six sidebands, the core effective 4-photon processes,  $|fg\rangle \leftrightarrow |gf\rangle$  and  $|gg\rangle \leftrightarrow |ff\rangle$  and the error-correcting QR drives can be realized simultaneously. In practice, the QQ red and blue sideband rates ( $W_r = 1.45$  MHz and  $W_b = 1.25$  MHz) are slightly different. When applying all sidebands, we choose a smaller  $W$ , because the coupler was found to heat and shift the readout resonator when driven at larger rates making tomographic reconstruction inaccurate. We choose almost opposite detunings ( $\nu_r = 0.8$  MHz,  $\nu_b = -0.9$  MHz) for larger energy separation of the eigenstates and better error correction performance. Both QR sidebands are turned on at rates  $\Omega_1 = \Omega_2 = 0.39$  MHz. Fig. 5.3(b) shows the evolution when the initial state is  $|fg\rangle$ . The average photon number of  $Q_1$  (in

red) and  $Q_2$  (in blue) are read out simultaneously, and the oscillation between 0 and 2 forms an effective 4-photon red sideband. Note that this effective swap process is slightly different from the direct  $|fg\rangle \leftrightarrow |gf\rangle$  transition as the population in  $|ee\rangle$  will appear intermediately when the initial state has overlap with the eigenstates that have  $|ee\rangle$  component. Under this condition,  $|ee\rangle$  is no longer the dark state when all six sidebands are on. Oscillation damping originates from the detuning-induced slow interference and decoherence of the qutrit subspace, and this distortion is captured by the simulation as well. Similarly, by choosing the initial state as  $|gg\rangle$ , the effective four-photon blue sideband  $|gg\rangle \leftrightarrow |ff\rangle$  can be observed in Fig. 5.3(c).

## 5.2 Error correction performance

The logical state initialization requires sequential application of multiple single-qutrit and two-qutrit rotations. For  $|L_0\rangle$  and  $|L_1\rangle$ , QQ red and blue sidebands are used to generate entanglement, and for  $|L_x\rangle = (|L_0\rangle + |L_1\rangle)/\sqrt{2} = (|g\rangle + |f\rangle)(|g\rangle - |f\rangle)/2$ , only single qutrit rotations are required. The preparation times for initial states are separately 313 ns, 142 ns, and 282 ns for  $|L_0\rangle$ ,  $|L_1\rangle$  and  $|L_x\rangle$ . The detailed preparation circuit is discussed in Sec. 5.4. We perform full two-qutrit state tomography [7, 76] and obtain initial state fidelities of 88.1%, 89.1% and 88.7% for the three states respectively. The tomography sequences and density matrix reconstruction are shown in Sec. 5.4.

We characterize the performance of the Star code by comparing three different cases — free decay, QQ sideband spin-locking (4 QQ echo), and full AQEC. For free decay, we do not apply any drive after the state preparation. For the 4 QQ echo case, we turn on the QQ sidebands  $|ee\rangle \leftrightarrow \{|gf\rangle, |fg\rangle, |gg\rangle, |ff\rangle\}$  with a similar rate-detuning configuration as shown in Fig. 4.14a ( $W_r = 1.0$  MHz,  $W_b = 1.7$  MHz,  $\nu_r = 1.5$  MHz,  $\nu_b = 0.0$  MHz). This case shows coherence improvement from spin-locking. The full AQEC ( $W_r = 1.45$  MHz,  $W_b = 1.25$  MHz,  $\nu_r = 0.8$  MHz,  $\nu_b = -0.9$  MHz,  $\Omega_1 = \Omega_2 = 0.39$  MHz) demonstrates

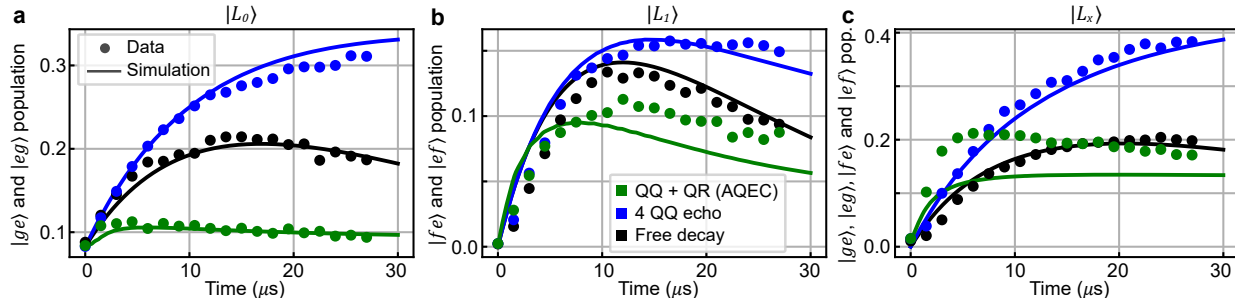


Figure 5.4: **Error population under different conditions.** Black, blue, and green points represent tomographic measurement results under free decay, 4 QQ echo, and full AQEC. The y-axes represent the combined population of error states for initial states **a**  $|L_0\rangle$ , **b**  $|L_1\rangle$ , and **c**  $|L_x\rangle$ . Population accumulates at the error states in the free decay case, enhanced in the 4 QQ echo case, and corrected with AQEC drive on. The experimental data is explained with master equation simulations shown in solid lines. Error bars (one standard deviation) are smaller than the marker size [24]. Detailed fitting parameters used for the solid lines are shown in Sec. 5.8.

further improvement from photon-loss correction. We plot the density matrices of the logical states after preparation and after 9  $\mu\text{s}$  in Sec. 5.4 for reference.

To demonstrate that our protocol corrects single-photon loss error, in Fig. 5.4, we plot the combined population of error states as a function of time for all three cases. The error populations are computed through the expectation values of  $\varepsilon_0 = |ge\rangle\langle ge| + |eg\rangle\langle eg|$  for  $|L_0\rangle$ ,  $\varepsilon_1 = |ef\rangle\langle ef| + |fe\rangle\langle fe|$  for  $|L_1\rangle$ , and  $\varepsilon_0 + \varepsilon_1$  for  $|L_x\rangle$  corresponding to the states after single-photon loss. We extract the error population from the density matrices reconstructed with full two-qutrit state tomography at each time point up to 27  $\mu\text{s}$  using the Maximum Likelihood Estimation (MLE) from 5000 repetitions of 81 different pre-rotation measurements for each state. This is a direct demonstration of the AQEC’s effectiveness, as it measures the error state population designed to correct by the protocol. Compared to the free decay cases (black dots), turning on the AQEC clearly corrects photon loss and suppresses the error rate below the free decay cases (green dots). The error rates for all three logical states increase in the 4 QQ echo case (blue dots), as enhanced qutrit decay rates in the presence of sideband can lead to extra photon loss.

In addition to correcting photon loss, it is also important to characterize how well

the AQEC protocol preserves the coherence of the logical states. To quantify the coherence, we plot the fidelity decay for each logical state. Fidelities are calculated as  $F = (\text{tr} \sqrt{\sqrt{\rho_m} \rho_{th} \sqrt{\rho_m}})^2$ , where  $\rho_{th} = |L_i\rangle \langle L_i|$ ,  $i = 0, 1, x$  depending on the compared logical states, and  $\rho_m$  is the experimentally measured density matrix. All expectation values' error bars are calculated using the Tomographer package [24]. Fitting the data to the exponential decays for  $|L_0\rangle$  and  $|L_1\rangle$  [69], the logical states' coherence are improved from 17.9  $\mu\text{s}$  ( $|L_0\rangle$ ) and 3.4  $\mu\text{s}$  ( $|L_1\rangle$ ) in the free decay cases, to 20.3  $\mu\text{s}$  and 16.8  $\mu\text{s}$  in the four QQ echo cases, and up to 28.1  $\mu\text{s}$  and 16.3  $\mu\text{s}$  in the error correction cases (see Fig. 5.5(a), (b)). This demonstrates a factor of 1.6 and 4.8 improvement in logical state coherence against the free decay case. We believe the coherence limit of  $|L_0\rangle$  and  $|L_1\rangle$  is limited by QR sidebands not being sufficiently small compared to the QQ sidebands, which causes leakage into the  $\{|T\rangle, |S_{\pm}\rangle\}$  states.  $|L_x\rangle$ 's lifetime after error correction is on par with the free decay case. The uncompensated ZZ coupling between transmons dephases the  $|L_x\rangle$  after error correction, but not for  $|L_0\rangle$  and  $|L_1\rangle$ . Therefore, we expect  $|L_x\rangle$ 's coherence time should be worse than that for  $|L_0\rangle$  and  $|L_1\rangle$ . The fact that turning on QR sidebands does not significantly worsen the  $|L_x\rangle$  coherence shows that without photon loss error, QR sidebands do not introduce significant dephasing error.

The large difference in free-decay coherence times between  $|L_0\rangle$  and  $|L_1\rangle$  originates from the low-frequency dephasing noise on  $\Phi_{\text{DC}}$  through the flux line. It causes a shift in both transmons' frequencies in the same direction, which  $|L_1\rangle$  is sensitive to but  $|L_0\rangle$  is not. The passive echo protection from the Star code drives suppresses this; consequently, in the 4 QQ echo case both logical states have similar coherence time.

The AQEC performance is primarily limited by three factors in our experiment. The most important fact is that the QQ sideband rates  $W_r$  and  $W_b$  are well below their ideal values. Stronger drives would further suppress phase noise (lifetimes in the 4 QQ echo experiment are well below  $2T_1$ , indicating room for improvement), and the increased energy separation

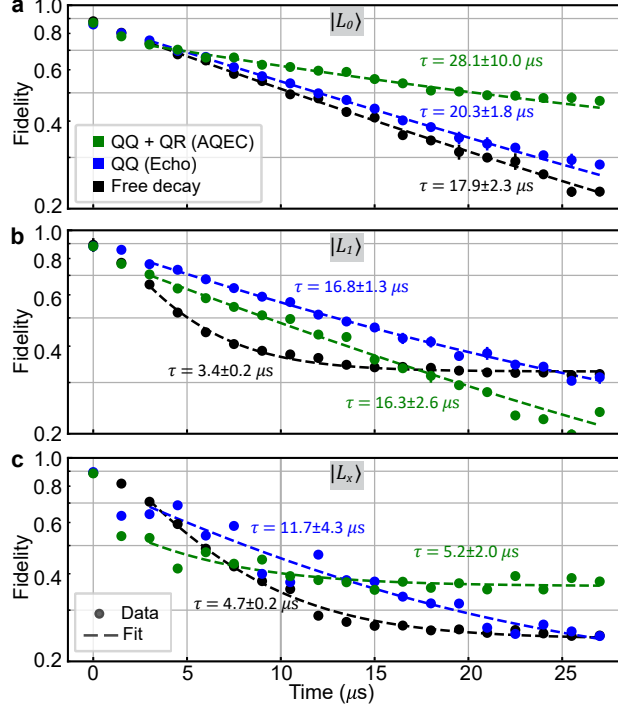


Figure 5.5: **Coherence improvement.** Black, blue, and green circles are experimentally measured state fidelities at a given time. The fidelities are extracted from the tomographic reconstruction of states with 5000 repeated measurements. Error bars (one standard deviation) are smaller than the marker size [24]. The improvement with AQEC turned on is explained by the master equation simulation. **a**  $|L_0\rangle$  and **b**  $|L_1\rangle$  traces are fitted to the exponential decay curve  $A \exp(-t/\tau) + C$ , and **c**  $|L_x\rangle$  traces are fitted to  $A \exp(-t/\tau)$ . The offset  $C$  is necessary since fidelity will achieve steady-state values. The error (one standard deviation) for  $\tau$  are obtained from the fitting. The large uncertainty comes from treating  $C$  as a free variable in the fitting. The fast transition period (first  $1.5 \mu\text{s} \sim \Omega_j^{-1}$  in the AQEC case is not included in the fitting\* for a better representation of logical coherence.

\*First  $10.5 \mu\text{s}$  data are used in  $|L_1\rangle$ 's free decay case for better fitting.

would also allow us to use stronger QR drives, correcting photon loss more quickly. Although the coupler supports 9 MHz QQ sidebands for short periods, when  $W_b$  goes beyond 5 MHz the readout resonator frequency starts to shift, introducing systematic measurement distortion (See Sec. 5.3 for details). This problem worsens with all six tones applied and we stay well below this limit to ensure reliable tomography results. The second limit is the  $ZZ$  coupling between the transmons, an extra dephasing channel for superposition states (see Sec. 5.5 for details). Our coupler is operated at the minimum  $ZZ$  flux bias of the coupler to minimize

the effect. It could be further mitigated by stronger QR sidebands enabling faster error correction, or through additional off-resonant QQ drive terms to dynamically cancel it. The third limit comes from heating and physical coherence drop when sidebands are turned on. The average photon number in the readout increases from  $< 0.01$  (free decay and 4 QQ echo cases) to 0.03 (AQEC case), which will actively convert a logical state to the error state under the QR interactions and significantly reduces logical lifetime. Photon-excitation events in the transmon are also non-correctable errors, but they should make smaller contributions to logical coherence (see Sec. 5.8). Further improvement can thus come from two paths—improving isolation between control signals or improving physical qubit coherence so that weaker drives can be more effective. Other limits are in the order of milliseconds (see Sec. 5.8) and do not affect our results considerably.

### 5.3 Chip design: Flux line optimization

In our device, we use the on-chip flux line to generate various two-qubit interactions through parametric modulation. A typical parametric coupler design includes two qubits capacitively or inductively coupled through a tunable coupler. Modulation of the coupler frequency and the qubit-coupler coupling strength contribute to the two-qubit interaction strength. For a capacitively coupled system [71, 17, 30, 80], coupler frequency modulation contributes dominantly to the QQ sideband rate, and time-dependent Schrieffer-Wolff transformation (SWT) proves that [71] the ratio of interaction strengths between bswap and iswap is  $\frac{\omega_1 - \omega_2}{\omega_1 + \omega_2}$  ( $\omega_j$  is  $Q_j$ 's frequency). Therefore, a capacitive coupler provides a slower bswap than the iswap. In contrast, an inductively coupled system [55, 12] modulates the coupling strength between the qubit and coupler more effectively, and both iswap and bswap will have the same zeroth-order terms in the SWT expansion, thus theoretically sharing the same rate under same modulation amplitude. Previous experiments achieved fast iswap interactions, but a similar bswap rate has not yet been demonstrated in either parametric coupler type.

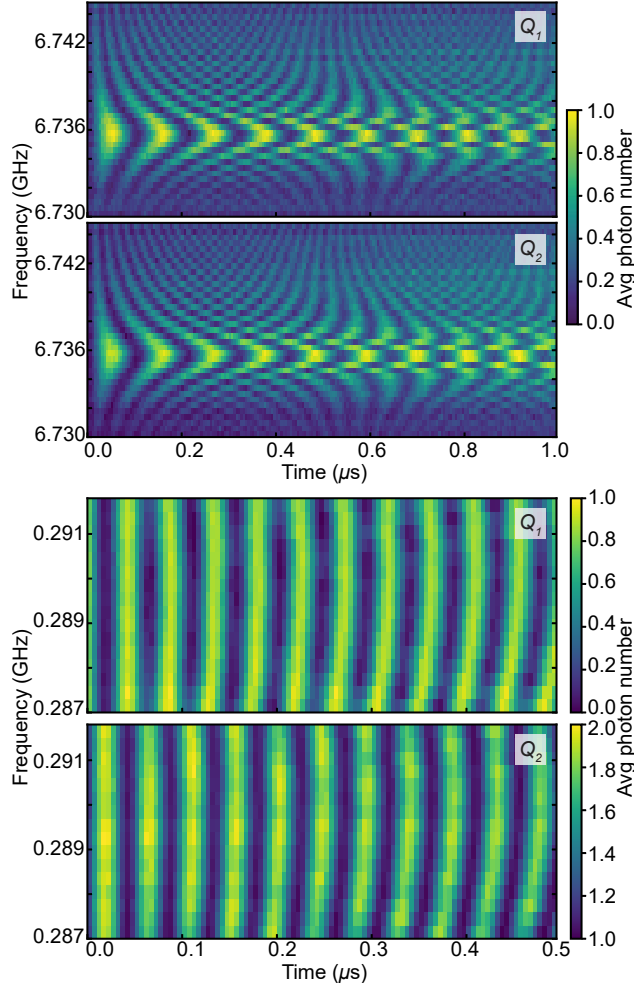


Figure 5.6: Chevron plots for fast QQ sidebands. The state of both transmons are simultaneously read out and shown as photon numbers. Top two figures show 9 MHz  $|gg\rangle \leftrightarrow |ee\rangle$ , and bottom two demonstrate 21 MHz  $|ee\rangle \leftrightarrow |gf\rangle$  oscillations.

We experimentally realize a comparable maximum rates of 9 MHz bswap and 21 MHz iswap (shown in Fig. 5.6).

In the experiment, we notice that turning a strong bswap on will shift both resonators' frequencies after a long time, resulting in the 'saturation' feature (Fig. 5.7). Such a readout frequency shift is both sideband strength and duration dependent, and the shift persists for a noticeable period after all sidebands are turned off. Distinguishing transmons' states through readout becomes difficult when this happens. A readout is possible when the shift is reversed after waiting for a sufficiently long period but degrades readout fidelity due to

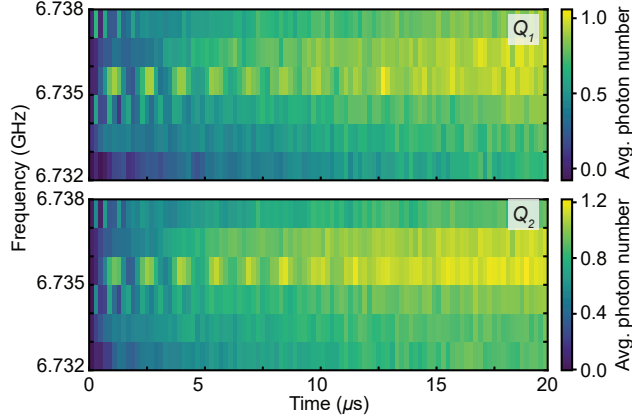


Figure 5.7: Readout saturation feature for fast (rate 9 MHz) QQ blue sideband  $|gg\rangle \leftrightarrow |ee\rangle$  in the long time scale. Top and bottom panel show readout signals from the first and second resonators.

transmons' relaxation. While case-dependent dynamic demarcation can distinguish states, this method becomes complex and inaccurate. In our experiment, we decided to lower the RF modulation amplitude and minimize the saturation region by optimizing the flux line geometry.

One source for the readout saturation at the bswap drive frequency is the flux line's stray charge coupling to the SQUID [12]. The on-chip flux line can be considered an antenna. The coupler is located in the near-field region, and the electrical field amplitude is proportional to the flux modulation frequency. Since bswap's drive frequencies are normally a magnitude higher than that of the iswap operations, a much stronger stray-charge drive is observed when the bswap drive is on.

We verify this fact using ANSYS HFSS simulation (see Fig. 5.8), where the electrical field amplitude is observed to increase over an order of magnitude when the modulation frequency is increased by a factor of 10. The stray charge drive limits the maximum power we can use for the flux modulation, and we focus on geometrical optimization to improve the flux-to-charge drive ratio. In order to do so, we maximize the mutual inductance between the SQUID and the flux line by increasing the SQUID loop size and bringing the flux line closer to the loop. The loop size in our experiment is limited by the SQUID's hysteresis [28] set by the

ratio  $\frac{L_{\text{loop}}}{L_{jc}}$ , where  $L_{jc}$  is the inductance of each junction in the SQUID (assumed identical) and  $L_{\text{loop}}$  is the SQUID loop inductance. When  $\frac{L_{\text{loop}}}{L_{jc}} > 1$ , transmon frequencies become hysteric as a function of  $\Phi_{\text{DC}}$ , and the region grows with the ratio. Dissipation appears when modulating within the hysteric region and should be avoided in our experiment. This property sets an upper bound for SQUID loop length.

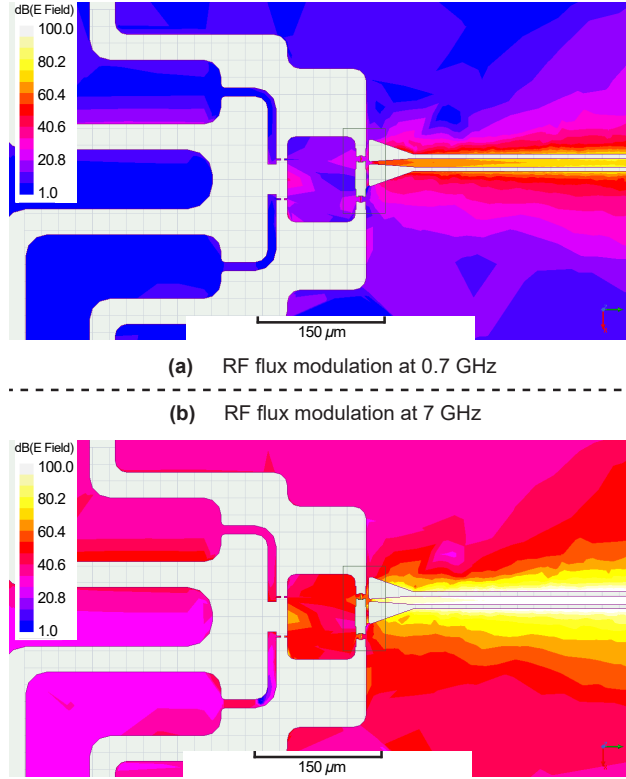


Figure 5.8: Distribution of electrical field's amplitude (in log scale) when RF flux drive is modulated at (a) 700 MHz and (b) 7 GHz obtained from HFSS simulation.

We use HFSS simulation to calculate flux threaded by the SQUID loop and vary the geometry to maximize. Assuming the electrical field is geometry insensitive around the SQUID, maximizing SQUID flux increases the ratio between the mutual inductive coupling and stray capacitive coupling strength of the flux line. The original and optimized designs are shown in Fig. 5.9. The simulation suggests a factor of 3.5 improvement in the ratio.

Being strongly coupled to the SQUID, the flux line is also a channel for transmons' relaxation. In order to improve Purcell protection, we design a Stepped-Impedance band-stop

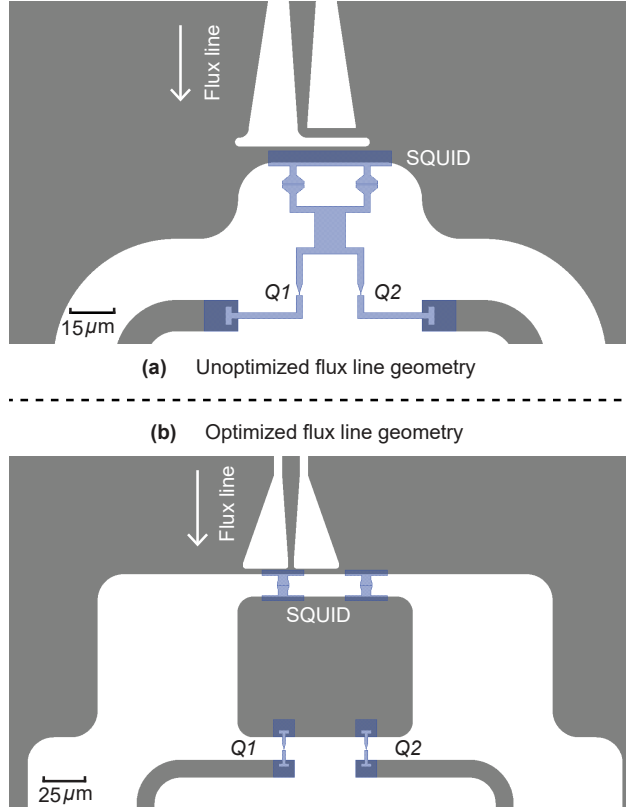


Figure 5.9: SQUID design. (a) Old design without optimization. (b) Current design by maximizing the mutual inductance between the flux line and SQUID. The Ta and Al areas are colored as grey and blue separately, and the bare sapphire is colored white.

Purcell Filter (SIPF) as shown in Fig. 5.10, which strongly blocks transmon frequencies while allowing the QQ red and blue sideband drives to pass (see Fig. 7.1 for the full measurement setup).

## 5.4 Full Star Code calibration process

We need to calibrate the QQ and QR sideband frequencies to implement the Star code when all sidebands are simultaneously on. The presence of external sidebands will change both transmons' frequencies through AC-stark shift and rectifying effect (RF modulation under a nonlinear frequency-flux response). In the experiment, we systematically perform the calibration, shown in Fig. 5.11.

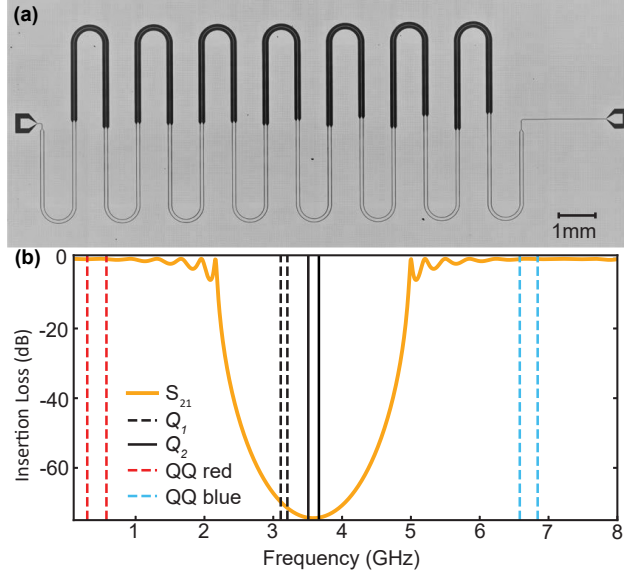


Figure 5.10: The stepped impedance Purcell filter (SIPF). (a) Optical image of our SIPF chip made using Ta on sapphire. (b) Calculated SIPF insertion loss. Transmon transitions, QQ red and blue sideband frequencies are marked in the plot.

In Fig. 5.11a, the static  $ZZ$  dispersive shift is characterized by measuring the Ramsey fringe frequency difference depending on the other qubit's state. In steps Fig. 5.11b and Fig. 5.11c, we first turn on all 6 QQ and QR drives at their bare frequencies. All QQ sideband rates are set to  $W$  when independently turned on. Two QQ red sidebands and two QQ blue sidebands are pair-swept separately as the 'red/blue pair'. The pair width and center are the sidebands' frequency difference and average. In each iteration step, we update sequentially the red and blue pair centers, and the QR sideband frequencies. For each pair, we sweep the center frequency as a function of time with all six sidebands on. We use  $|gg\rangle$  (blue pair) and  $|fg\rangle$  (red pair) as the initial states. Reading out the average photon number in both transmons, the 2D sweep plots show a fringed chevron pattern (shown in Fig. 5.12). The pattern's center line is the new pair center. The fringe rate represents the actual sideband detunings  $\nu_{b/r}$  and rate  $W_{b/r}$ , and the detunings can be updated by changing pair width at this stage. After extracting both pairs' new centers, the QR sidebands are calibrated with  $|eg\rangle$  and  $|ge\rangle$  as the initial state when all drives are on. Populating  $|f\rangle$  with

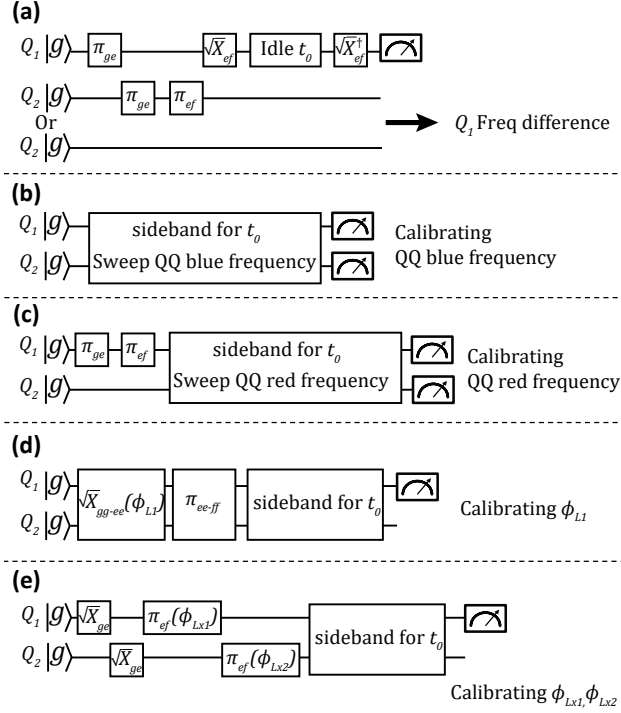


Figure 5.11: Gate circuits for the Star code calibration. (a) Pulse sequence for calibration of  $ZZ_{ff1}$ . Ramsey-like protocol is used for the partner transmon being in  $|g\rangle$  or  $|f\rangle$ . The other  $ZZ$ s are calibrated similarly. (b) QQ blue and (c) QQ red sideband frequency calibration sequence. QQ sideband pair frequencies are iteratively swept and updated based on the time-domain pattern. (d)  $|L_1\rangle$  preparation phase calibration sequence. The phase point that has minimum  $|e\rangle$  population in the sweep is chosen as the calibrated  $\phi_{L1}$ . The preparation phase for  $|L_0\rangle$  is calibrated similarly. (e)  $|L_x\rangle$  preparation phase calibration protocol. All  $\sqrt{X}$  operators represent  $\pi/2$  rotations.

the  $|e0\rangle \leftrightarrow |f1\rangle$  process is most efficient when QR sidebands are on resonance. Because of none zero  $ZZ_{ff1}$  and  $ZZ_{ff2}$ , the QR sidebands cannot be exactly on resonance for both  $|L_i\rangle$ . In the experiment, we calibrate QR sidebands to be on resonance for the  $|L_0\rangle$ . For  $|L_1\rangle$ , the error correction process will be slower but not dephase the state after correction. After a few iterations, we get decent frequency calibrations of all six sidebands.

Logical state preparation includes both charge and flux drives with appropriate relative phases. Fig. 5.11d is to calibrate  $|L_0\rangle$  and  $|L_1\rangle$ 's preparation phase. For the logical state  $|L_0\rangle$ , we first apply two  $\pi_{ge}$  pulses sequentially on  $Q_1$  and  $Q_2$  to prepare  $|ee\rangle$  through charge lines. Afterwards a  $(\pi/2)_{|ee\rangle \leftrightarrow |gf\rangle}$  pulse with a phase offset  $\phi_{L0}$  and a  $\pi_{|ee\rangle \leftrightarrow |fg\rangle}$

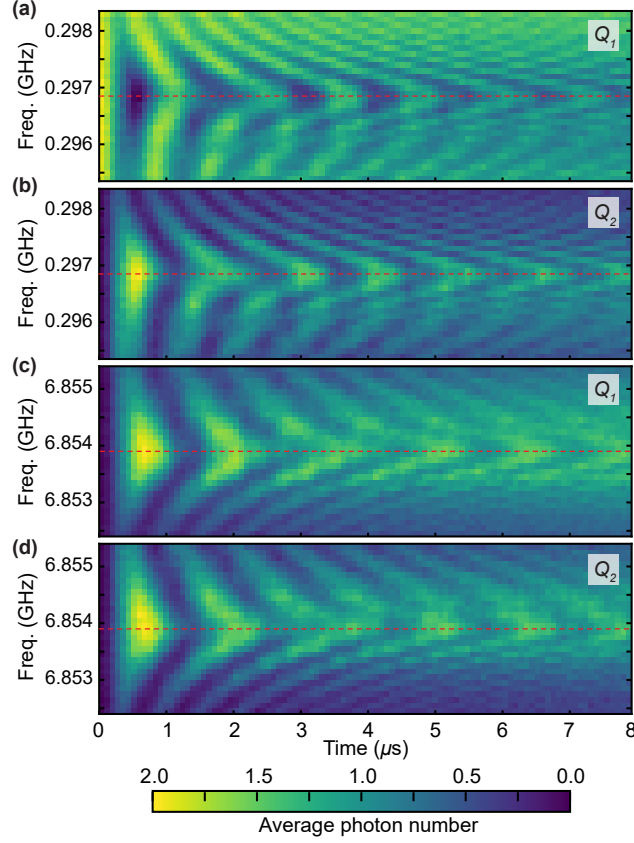


Figure 5.12: Simultaneous QQ sideband calibration. All six tones used in the Star code are simultaneously turned on during the frequency-time sweep. The red (top two panels) and blue (bottom two panels) QQ sideband pair frequencies are swept individually for calibration in the presence of the other pair. Red dash lines in the plots represent the pairs' center frequency choices. (a) and (b) are  $Q_1$  and  $Q_2$ 's average photon number when sweeping the red pair with the initial state  $|fg\rangle$ . (c) and (d) are  $Q_1$  and  $Q_2$ 's average photon number when sweeping the blue pair with the initial state  $|gg\rangle$ .

pulse are applied through the flux line. To prepare  $|L_1\rangle$ , a  $(\pi/2)_{|gg\rangle\leftrightarrow|ee\rangle}$  pulse with some phase  $\phi_{L1}$  followed by a  $\pi_{|ee\rangle\leftrightarrow|ff\rangle}$  are applied through the flux line. These steps generally prepare  $(|gf\rangle - e^{i\phi_{L0}}|fg\rangle)/\sqrt{2}$  and  $(|gg\rangle - e^{i\phi_{L1}}|ff\rangle)/\sqrt{2}$ . For non-zero  $\{\phi_{L0}, \phi_{L1}\}$ ,  $|ee\rangle$  is populated under the action of  $\tilde{H}_{\text{static}}$ , and we use this feature to find the correct preparation phases. We sweep the phase  $\phi_{L0(1)}$  in the presence of all six tones and observe  $|e\rangle$  population on both qutrits. The correct preparation phases are determined by values that minimize  $|e\rangle$  population of both transmons during the first  $8\mu\text{s}$  of error correction, as presented in Fig. 5.13.

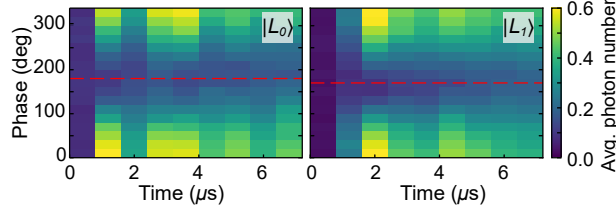


Figure 5.13: Preparation phase calibration of  $|L_0\rangle$  (left) and  $|L_1\rangle$  (right) in the error correction experiment. The population of  $|e\rangle$  on  $Q_1$  are measured after turning on all sidebands for up to  $8\ \mu\text{s}$ , and the red dash line marks the calibrated phase position. We choose  $Q_1$  due to higher readout fidelity.

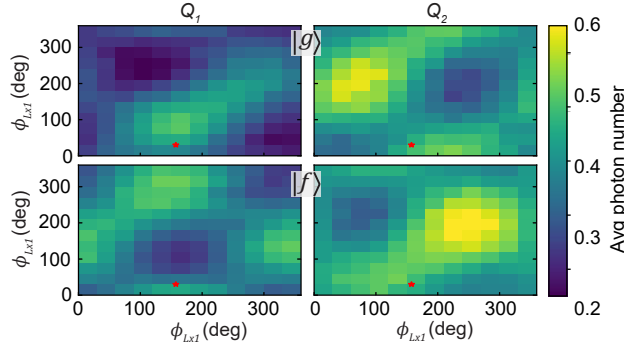


Figure 5.14: Phase calibration for  $|L_x\rangle$  preparation. Population of  $|g\rangle$  (top) and  $|f\rangle$  (bottom) on  $Q_1$  (left) and  $Q_2$  (right) are measured after  $8\ \mu\text{s}$ , and the red star marks the calibrated phase position.

Preparation of  $|L_x\rangle = (|L_0\rangle + |L_1\rangle)/\sqrt{2}$  does not require any sideband pulses as it is a product state  $(|g\rangle - |f\rangle)(|g\rangle + |f\rangle)/2$ . We apply a  $(\pi/2)_{ge}$  pulse with a specific phase, followed by a  $\pi_{ef}$  pulse on both transmons. These pulses prepare the state

$$\left(|g\rangle + e^{i\phi_{Lx1}} |f\rangle\right) \left(|g\rangle + e^{i\phi_{Lx2}} |f\rangle\right) / 2, \quad (5.5)$$

leaving two preparation phases  $\phi_{Lx1}$  and  $\phi_{Lx2}$  left for calibration. The correct phase combination can be calibrated on the 2D  $\phi_{Lx1}$ - $\phi_{Lx2}$  phase sweep plot. Correct preparation phases will keep equal populations of  $|g\rangle$  and  $|f\rangle$  for both transmons at any time after turning on all sidebands. In Fig. 5.11e, both transmons'  $|g\rangle$  and  $|f\rangle$  populations are measured  $8\ \mu\text{s}$  after turning sidebands on. Fig. 5.14 shows the 2D phase sweep plot. This yields four

phase coordinates  $\{\phi_{Lx1}, \phi_{Lx2}\} = \{0, 180^\circ\} \otimes \{0, 180^\circ\}$ , and two of the four correspond to  $(|L_0\rangle \pm |L_1\rangle)/\sqrt{2}$ . We distinguish the logical  $|L_x\rangle$  by taking two-qutrit state tomography measurements after turning on the sidebands for  $9\ \mu\text{s}$  and choose the error-corrected case. The calibration process for the 4 QQ echo case is the same, except the QR sidebands are off.

In the experiment, we pick the largest QQ sideband rate  $W$  that does not cause a significant heating effect and choose the other parameters  $\{\nu_{r/b}, \Omega_{1/2}\}$  accordingly. As discussed in Sec. 3.2, larger  $W$  means better AQEC performance. Given the maximum  $W$  fixed, the optimal QQ red and blue sideband detunings  $\{\nu_r, \nu_b\}$  appear around  $\nu_r = -\nu_b = \pm W/2$  [49]. In the experiment, we select the optimal sideband detunings before calibration, then extract the actual detunings (changed by AC stark shift) after the calibration  $\{\nu_r, \nu_b\} = \{0.8, -0.9\}$  MHz. The AQEC performance is not sensitive to the detuning choice around the optimal point in the simulation. We choose the QR sideband rate  $\Omega$  that has around the best AQEC performance in simulation given fixed  $W$ .

## 5.5 ZZ cancellation

Realizing AQEC requires error transparency to single photon loss error. This makes  $ZZ$  coupling an extra logical dephasing channel as it does not commute with  $\tilde{H}_{\text{star}}$ . In a two qutrit system, there are in total 7 different  $ZZ$  frequency shifts coming from 4 cross-Kerr coupling strengths  $J_{11}, J_{21}, J_{12}, J_{22}$  (See Sec. 4.1). However, not all  $ZZ$  couplings are detrimental to the Star code. The error transparency requires no phase accumulation between logical states during the error correction process. This is equivalent to having the same energy for the photon lost from one transmon, independent of the state of the partner transmon,

$$\begin{aligned} E_{ff} - E_{ef} &= E_{fg} - E_{eg}, \\ E_{ff} - E_{fe} &= E_{gf} - E_{ge}. \end{aligned} \tag{5.6}$$

Here  $E_{jk}$  refers to the energy of the state  $|jk\rangle$ . Eq. (5.6) are equivalent to  $ZZ_{ff2} = ZZ_{ff1} = 0$  (see Sec. 4.1). When this is not the case, a random phase difference will accumulate between logical states after the error correction, introducing dephasing to the logical superposition states. The other  $ZZ$ s are naturally error transparent in the logical manifold since  $|ee\rangle$  is dark and will not affect the logical states' coherence. To suppress the  $ZZ$ -induced logical dephasing, we can increase the QR sideband rate  $\Omega_j$ , shortening the  $|e\rangle$  population time in both qutrits and reducing the accumulated random logical phase. To eliminate this dephasing channel, we need a coupler that has zero  $ZZ_{ff1}$  and  $ZZ_{ff2}$  when all external sidebands are turned on. This can be potentially realized in our current coupler with dispersive shift engineering. We consider a two-transmon system with static interaction that produces a set of dispersive shifts for cancellation. The base Hamiltonian  $H_{\text{base}}$  is

$$H_{\text{base}} = \sum_n (\epsilon_{1,n} |n_1\rangle \langle n_1| + \epsilon_{2,n} |n_2\rangle \langle n_2|) + \sum_{nm} \Delta_{nm} |n_1 m_2\rangle \langle n_2 m_1|, \quad (5.7)$$

where  $\epsilon_{1/2,n}$  are energies for single transmon levels,  $\Delta_{nm}$  is the static energy shift to the state when transmon 1 has  $n$  photons and transmon 2 has  $m$  photons. For the ground state  $\epsilon_{1/2,0}$  and  $\Delta_{00}$  are set to 0. We add to  $H_{\text{base}}$  a QQ red sideband through the coupler,

$$H_D = 2g \sin(2\pi\nu t) (a_{q1}^\dagger a_{q2} + a_{q1} a_{q2}^\dagger). \quad (5.8)$$

We assume the frequency detuning  $\nu$  is far off-resonant so that  $\nu \gg g$ , and this will introduce an energy shift  $D_{jk}$  to all levels:

$$D_{jk}^{(R)} = \frac{g^2 j(k+1)}{E_{j,k} - E_{j-1,k+1} - \nu} + \frac{g^2 j(k+1)}{E_{j,k} - E_{j-1,k+1} + \nu} + \frac{g^2 (j+1)k}{E_{j,k} - E_{j+1,k-1} - \nu} + \frac{g^2 (j+1)k}{E_{j,k} - E_{j+1,k-1} + \nu}. \quad (5.9)$$

For a detuned QQ blue sideband drive, one can find a similar expression for the energy shift,

$$D_{jk}^{(B)} = \frac{g^2(j+1)(k+1)}{E_{j,k} - E_{j+1,k+1} - \nu} + \frac{g^2(j+1)(k+1)}{E_{j,k} - E_{j+1,k+1} + \nu} + \frac{g^2jk}{E_{j,k} - E_{j-1,k-1} - \nu} + \frac{g^2jk}{E_{j,k} - E_{j-1,k-1} + \nu}. \quad (5.10)$$

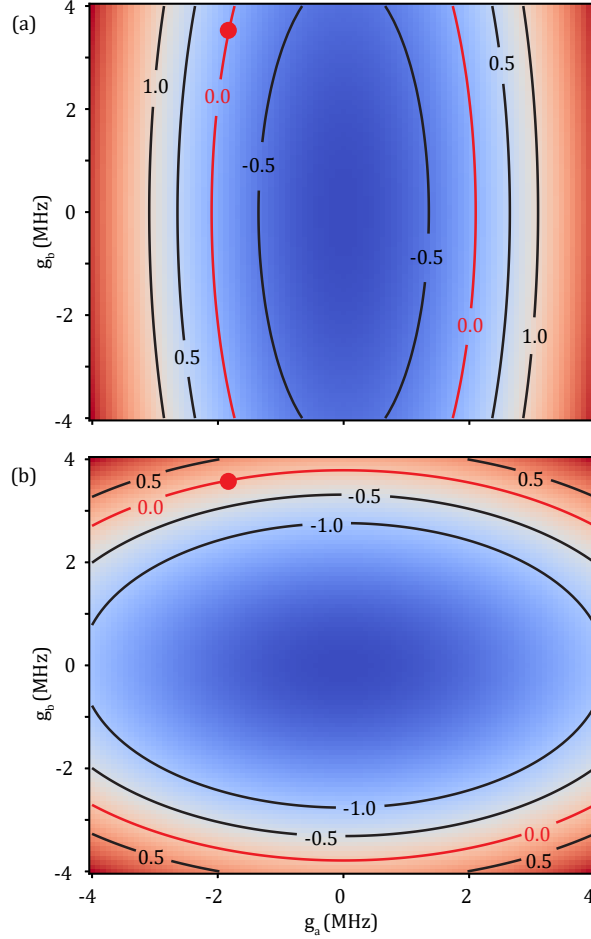


Figure 5.15:  $ZZ$  cancellation. Total  $ZZ_{ff1}$  (a) and  $ZZ_{ff2}$  (b) (in MHz) are shown in the contour while sweeping amplitudes of two extra detuned external drives ( $|ef\rangle \leftrightarrow |gh\rangle$  and  $|fe\rangle \leftrightarrow |hg\rangle$ ). Individual  $ZZ$  cancellation contour line (with value 0) is marked. One of the four simultaneous cancellation points is highlighted in red circle.

When multiple external QQ sidebands are applied, the total dispersive shift to each energy level is given by  $D_{jk} = \sum D_{jk}^{(R)} + \sum D_{jk}^{(B)}$ , where the sum is over all external QQ sidebands. Specifically for the Star code scheme, we can modulate two extra QQ sidebands

near  $|ef\rangle \leftrightarrow |gh\rangle$  and  $|fe\rangle \leftrightarrow |hg\rangle$ . This can introduce either positive or negative  $D_{12}$  and  $D_{21}$  to the system, depending on the choices of frequency detuning. The required  $g$  for complete  $ZZ$  cancellation can be less than 5 MHz. Therefore, it is theoretically possible to cancel  $ZZ_{ff1}$  and  $ZZ_{ff2}$  simultaneously under such two extra drives.

We choose the experiment sideband parameters  $\{W_r, W_b, \nu_r, \nu_b\} = \{1.45, 1.25, -0.8, 0.9\}$  MHz and current total  $ZZ$  rate  $\{ZZ_{ff1}, ZZ_{ff2}\} = \{-0.6, -2.2\}$  MHz. We add two external drives:  $|ef\rangle \leftrightarrow |gh\rangle$  and  $|fe\rangle \leftrightarrow |hg\rangle$  with frequency detunings  $\{-2, 2\}$  MHz and sweep the drive strengths  $\{g_a, g_b\}$ . Here  $\{g_a, g_b\}$  is the coefficient  $g$  for  $H_D$  (Eq. (5.8)). We calculated the total  $ZZ_{ff1}$  and  $ZZ_{ff2}$  based on Eq. (5.9) and Eq. (5.10) and plot the 2D sweep results in the following Fig. 5.15. The simultaneous  $ZZ$  cancellation points are highlighted in the figure. Therefore it is always possible to fully cancel  $ZZ_{ff1}$  and  $ZZ_{ff2}$  with external drives. We did not turn on the cancellation sidebands in the experiment, because our readout suffers from frequency shift under strong flux modulation amplitude as discussed in Sec. 5.3.

## 5.6 State transfer rate

Logical lifetime is calculated analytically given the level diagram in Fig. 3.4. Assuming only photon loss (dephasing is suppressed), there are two uncorrectable error channels: a second photon loss before the error correction and the population trapped in the quasi-stable state. All error correction is a two-step refilling process. For  $Q_1$ 's photon loss error, the refilling rate from  $|eg00\rangle$  to  $|L_000\rangle$  and from  $|ef00\rangle$  to  $|L_100\rangle$  are both  $\Gamma_{R1} = \frac{\Omega_1^2 \kappa_1}{\Omega_1^2 + \kappa_1^2}$ . Due to the finite energy gap, the QR sideband also introduces a slow oscillation between  $|eg00\rangle$  and  $\{|S_-10\rangle, |T10\rangle, |S_+10\rangle\}$  (discussions for  $|ef00\rangle$  is similar). Once the photon in the resonator decays, the population is trapped in  $|S_-00\rangle, |T00\rangle, |S_+00\rangle$ , causing the logical decoherence. The quasi-stable states' refilling rate  $\{\Gamma_{S_-}^{L0;R1}, \Gamma_T^{L0;R1}, \Gamma_{S_+}^{L0;R1}\}$  are also two-step refilling processes:

$$\left\{ \begin{array}{l} \Gamma_{S-}^{L0;R1} = \frac{\kappa_1 \Omega_1^2 (\langle S_- | fg \rangle)^2}{\kappa_1^2 + \Omega_1^2 (\langle S_- | fg \rangle)^2 + 4(x_3 + \nu_r)^2}, \\ \Gamma_T^{L0;R1} = \frac{\kappa_1 \Omega_1^2 (\langle T | fg \rangle)^2}{\kappa_1^2 + \Omega_1^2 (\langle T | fg \rangle)^2 + 4(x_2 + \nu_r)^2}, \\ \Gamma_{S+}^{L0;R1} = \frac{\kappa_1 \Omega_1^2 (\langle S_+ | fg \rangle)^2}{\kappa_1^2 + \Omega_1^2 (\langle S_+ | fg \rangle)^2 + 4(x_1 + \nu_r)^2}. \end{array} \right. \quad (5.11)$$

The refilling rate superscript means when  $|L_0\rangle$  is the initial state, using  $R_1$  to correct photon loss in  $Q_1$ . The subscript shows the final state. The other three sets of refilling rates  $\{\Gamma_{S-}^{L0;R2}, \Gamma_T^{L0;R2}, \Gamma_{S+}^{L0;R2}\}$ ,  $\{\Gamma_{S-}^{L1;R1}, \Gamma_T^{L1;R1}, \Gamma_{S+}^{L1;R1}\}$ ,  $\{\Gamma_{S-}^{L1;R2}, \Gamma_T^{L1;R2}, \Gamma_{S+}^{L1;R2}\}$  have a similar expression.

The error correction performance benefits from larger  $\Gamma_{Rj}$  and smaller quasi-stable states' refilling rates.  $\Gamma_{Rj}$  are increased with  $\Omega_j$ , which is bounded by  $W_{r/b}$  for perturbation validity. Quasi-stable states' refilling rates are suppressed with larger  $W_{r/b}$  and  $\nu_{r,b}$ . From Eq. (5.11), quasi-stable states' refilling rates are quadratically reduced with a larger energy gap  $|x_j + \nu_{r,b}|$ . Increasing  $W_{r,b}$  and  $\nu_{r,b}$  generally helps increase the energy gaps  $|x_j + \nu_{r,b}|$ . And as a special case, when  $\nu_r = -\nu_b = \nu$ ,  $W_r = W_b = W$ ,  $\{x_j\}$  is  $\{-\sqrt{W^2 + \nu^2}, 0, \sqrt{W^2 + \nu^2}\}$ . Clearly, the energy gap is increased with larger  $W$  and  $\nu$ .

With our experiment parameters

$$\begin{aligned} & \{W_r, W_b, \Omega_1, \Omega_2, \kappa_1, \kappa_2, \nu_r, \nu_b\} \\ & = \{1.45, 1.25, 0.39, 0.39, 0.53, 0.48, 0.8, -0.9\} \text{ MHz}, \end{aligned}$$

The quasi-stable states  $\{|S_{\pm}, |T\rangle\rangle\}$  have the following overlap with the basis  $\{|fg\rangle, |gg\rangle\}$ :

Transition label	Description	Rate (kHz)
$\Gamma_{R1}$	$Q_1$ decay error correction rate	186.2
$\Gamma_{R2}$	$Q_2$ decay error correction rate	190.9
$\Gamma_{S_-}^{L0;R1}$	$ L_0\rangle \rightarrow  S_-\rangle$ rate ( $Q_1$ decay)	8.0
$\Gamma_T^{L0;R1}$	$ L_0\rangle \rightarrow  T\rangle$ rate ( $Q_1$ decay)	3.7
$\Gamma_{S_+}^{L0;R1}$	$ L_0\rangle \rightarrow  S_+\rangle$ rate ( $Q_1$ decay)	0.1
$\Gamma_{S_-}^{L0;R2}$	$ L_0\rangle \rightarrow  S_-\rangle$ rate ( $Q_2$ decay)	7.4
$\Gamma_T^{L0;R2}$	$ L_0\rangle \rightarrow  T\rangle$ rate ( $Q_2$ decay)	3.4
$\Gamma_{S_+}^{L0;R2}$	$ L_0\rangle \rightarrow  S_+\rangle$ rate ( $Q_2$ decay)	1.0
$\Gamma_{S_-}^{L1;R1}$	$ L_1\rangle \rightarrow  S_-\rangle$ rate ( $Q_1$ decay)	0.1
$\Gamma_T^{L1;R1}$	$ L_1\rangle \rightarrow  T\rangle$ rate ( $Q_1$ decay)	6.0
$\Gamma_{S_+}^{L1;R1}$	$ L_1\rangle \rightarrow  S_+\rangle$ rate ( $Q_1$ decay)	10.7
$\Gamma_{S_-}^{L1;R2}$	$ L_1\rangle \rightarrow  S_-\rangle$ rate ( $Q_2$ decay)	0.1
$\Gamma_T^{L1;R2}$	$ L_1\rangle \rightarrow  T\rangle$ rate ( $Q_2$ decay)	5.1
$\Gamma_{S_+}^{L1;R2}$	$ L_1\rangle \rightarrow  S_+\rangle$ rate ( $Q_2$ decay)	10.0

Table 5.1: Calculated refilling process rate in our experiment. Logical refilling rate  $\{\Gamma_{R1}, \Gamma_{R2}\}$  dominants over other logical error rate.

$$\begin{aligned}
& \{(\langle S_- | fg \rangle)^2, (\langle T | fg \rangle)^2, (\langle S_+ | fg \rangle)^2\} \\
& = \{0.294, 0.174, 0.032\},
\end{aligned} \tag{5.12}$$

$$\begin{aligned}
& \{(\langle S_- | gg \rangle)^2, (\langle T | gg \rangle)^2, (\langle S_+ | gg \rangle)^2\} \\
& = \{0.023, 0.185, 0.293\}
\end{aligned} \tag{5.13}$$

All refilling process rates are shown in Table 5.1.

## 5.7 Two-qutrit tomography

Following the basis choice in Ref. [7], we apply 81 post rotations  $S_j$  from the tomography rotation set  $S \otimes S$ :  $S = \{I, R_{ge}(0, \frac{\pi}{2}), R_{ge}(\frac{\pi}{2}, \frac{\pi}{2}), R_{ge}(0, \pi), R_{ef}(0, \frac{\pi}{2}),$

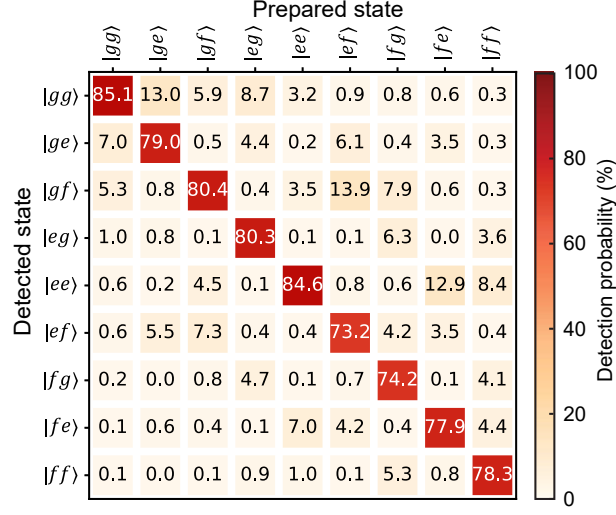


Figure 5.16: Single shot confusion matrix. Two-qutrit basis states are prepared and measured 5000 times.

$$R_{ef} \left( \frac{\pi}{2}, \frac{\pi}{2} \right), R_{ef} \left( 0, \frac{\pi}{2} \right) R_{ge} (0, \pi), R_{ef} \left( \frac{\pi}{2}, \frac{\pi}{2} \right) R_{ge} (0, \pi),$$

$R_{ef} (0, \pi) R_{ge} (0, \pi) \}$ . Here  $I$  is the identity gate, and the rotations  $R_{ge}$  and  $R_{ef}$  are defined as follows

$$R_{ge} (\phi, \theta) = \begin{bmatrix} \cos \frac{\theta}{2} & -e^{-i\phi} \sin \frac{\theta}{2} & 0 \\ e^{i\phi} \sin \frac{\theta}{2} & \cos \frac{\theta}{2} & 0 \\ 0 & 0 & 1 \end{bmatrix}, \quad (5.14)$$

$$R_{ef} (\phi, \theta) = \begin{bmatrix} 1 & 0 & 0 \\ 0 & \cos \frac{\theta}{2} & -e^{-i\phi} \sin \frac{\theta}{2} \\ 0 & e^{i\phi} \sin \frac{\theta}{2} & \cos \frac{\theta}{2} \end{bmatrix}. \quad (5.15)$$

Simultaneous single-shot readouts are collected after each of the 81 rotations. Fig. 5.16 shows the single shot confusion matrix of our readout. To compensate for the measurement error, we applied the inverse of the confusion matrix to the readout result. Maximum-Likelihood-Estimation (MLE) is used to reconstruct the physical density matrix  $\rho_m$  that

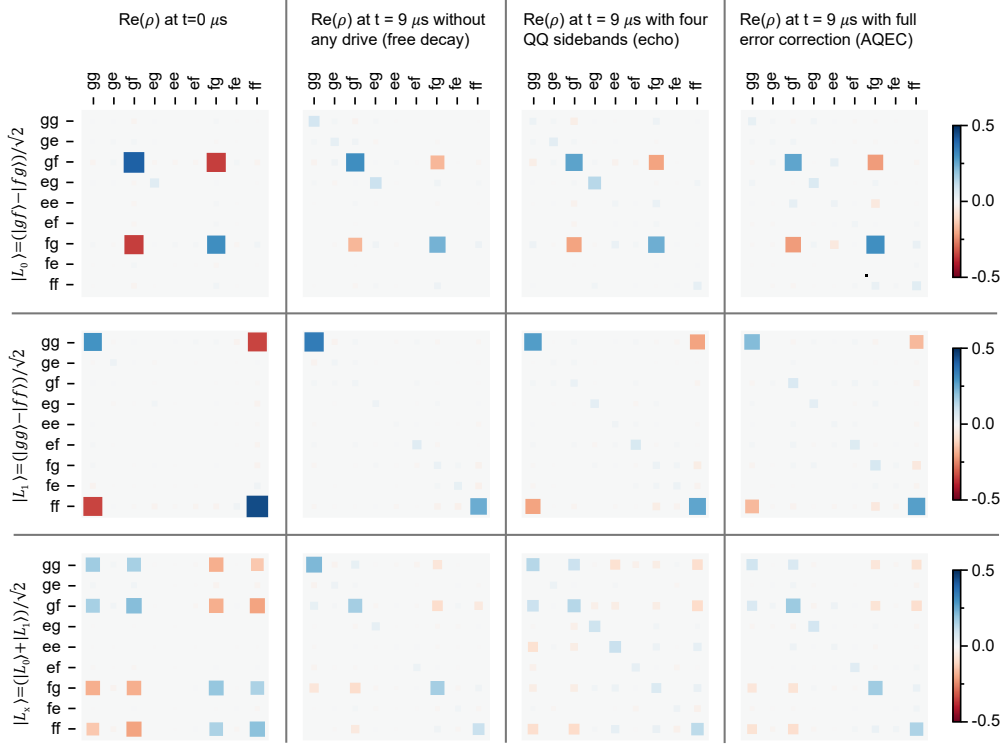


Figure 5.17: Evolution of the logical states under different conditions. Panels from top to bottom correspond to the logical state  $|L_0\rangle$ ,  $|L_1\rangle$  and  $|L_x\rangle$ . The real part of the density matrices are plotted as the imaginary components are small after phase rotation. The left column shows the initial states. Improvements in the coherence can be seen for the echo case when compared to free decay. With the full Star code protocol, further improvements are observed.

minimizes the cost function  $f_c$ ,

$$f_c(\vec{p}, \vec{q}) = \sum_{j=1}^{81} \sum_{a,b=g,e,f} \left( \frac{p_{j,|ab\rangle} - q_{j,|ab\rangle}}{q_{j,|ab\rangle}} \right)^2, \quad (5.16)$$

$$p_{j,|ab\rangle} = \langle ab | S_j \cdot \rho_m | ab \rangle,$$

$$q_{j,|ab\rangle} = \langle ab | S_j \cdot \rho_{exp} | ab \rangle.$$

Here  $q_{j,|ab\rangle}$  is the measured probability for  $|ab\rangle$  after the  $j$ th tomography rotation. For any state tomography data, we repeat the same experiment 5000 times to approximate each  $q_{j,|ab\rangle}$ . We first obtain  $\rho_{exp}$  from direct inversion of the experimental data and then perform

MLE to find the physical density matrix  $\rho_m$ .

The tomographically reconstructed states after preparation and after 9  $\mu\text{s}$  for the three cases of free decay, 4 QQ echo, and AQEC are illustrated in Fig. 5.17.

## 5.8 Error analysis

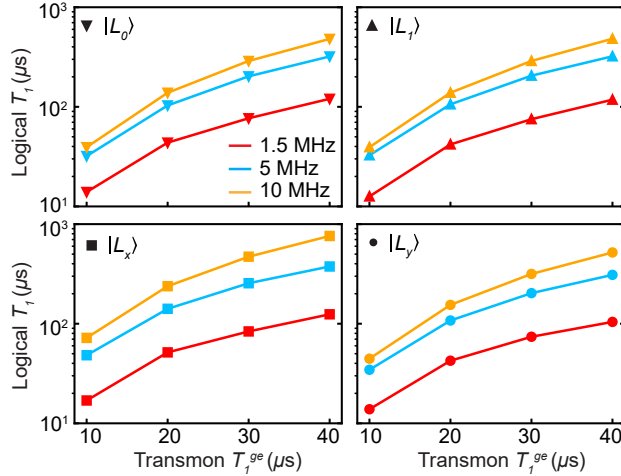


Figure 5.18: Theoretical logical lifetime in the rotating frame. The logical lifetime increases as a function of physical  $T_1$ . A larger QQ sideband rate also provides higher logical qubit coherence. Parameter used for simulation are  $\{W = 10, 5 \text{ MHz}, \Omega_j = 1.0 \text{ MHz}, \nu_r = -\nu_b = \frac{W}{2}\}$ ,  $\{W = 1.5 \text{ MHz}, \Omega_j = 0.4 \text{ MHz}, \nu_r = -\nu_b = 0.85 \text{ MHz}\}$  and  $\kappa = 0.5 \text{ MHz}$ .

All simulations are carried out in a Hamiltonian of dimension  $3 \times 3 \times 2 \times 2$  (two levels for each resonator). We first simulate the theoretical lifetime improvement with only photon-loss error in the static frame (See Sec. 3.3), and the results are shown in Fig. 5.18. All simulated data show improvements beyond the break-even point, even with only  $10 \mu\text{s}$   $T_1^{ge}$  and modest rate requirements for QQ and QR sidebands. The logical coherence limits come from the double photon-loss event and off-resonant population to other stray states from the spectrum crowding (see Ref. [49]). A logical error happens when a second photon decays (from  $|e\rangle$  to  $|g\rangle$ ) before getting corrected.  $|L_x\rangle$  has a higher lifetime than  $|L_j\rangle$  because it is partially protected against double photon loss in a single transmon (See discussion in Sec. 3.3). Longer

physical  $T_1^{ge}$ , larger  $W_{r/b}$ , and  $\Omega_j$  for a faster error correction rate help increase this limit.

To simulate the real system, several error channels are introduced in the static frame  $\tilde{H}_{\text{static}}$  — single photon decay  $T_1^{ge,j}$  and  $T_1^{ef,j}$ , single transmon dephasing  $T_\phi^j$ , single-photon excitation  $T_1^\dagger$ , resonator photon population  $n_{\text{res}}$  and extra correlated dephasing  $T_\phi^{|ff\rangle}$  at  $|ff\rangle$  level. Since only  $ZZ_{ff1}$  and  $ZZ_{ff2}$  have effects on the logical state, we model the  $ZZ$ s by directly adding energy shifts to  $|fe\rangle$  and  $|ef\rangle$ , so that all logical basis still share the same energy and remain static in the frame. In the presence of external drives, the parameters will be different from the free decay case. We use experimentally measured  $ZZ_{ff1}$  and  $ZZ_{ff2}$  values in the simulation. The full master equation is solved in QuTip,

$$\begin{aligned}
\frac{\partial \rho(t)}{\partial t} = & -i [H_{\text{full}}, \rho(t)] \\
& + \left( \sum_{j=1,2} \left( \frac{1}{T_1^{ge,j}} D_j[|g\rangle \langle e|] + \frac{1}{T_1^{ef,j}} D_j[|e\rangle \langle f|] \right. \right. \\
& + \frac{1}{T_1^\dagger} D_j[|e\rangle \langle g|] + \frac{2}{T_1^\dagger} D_j[|f\rangle \langle e|] \\
& + \frac{1}{T_\phi^j} D_j[|e\rangle \langle e|] + \frac{4}{T_\phi^j} D_j[|f\rangle \langle f|] \\
& + \kappa_j n_{\text{res}} D[a_{rj}^\dagger] + (1 + n_{\text{res}}) \kappa_j D[a_{rj}] \\
& \left. \left. + \frac{1}{T_\phi^{|ff\rangle}} D_{12}[|ff\rangle \langle ff|] \right) \rho(t). \tag{5.17}
\end{aligned}$$

Here we define

$$H_{\text{full}} = \tilde{H}_{\text{static}} + \sum_{j=1,2} \chi_j n_{qj} n_{rj} + (ZZ_{ff1} |fe\rangle \langle fe| + ZZ_{ff2} |ef\rangle \langle ef|) \otimes I_4, \quad (5.18)$$

$$D[A]\rho = A\rho A^\dagger - \frac{1}{2} (A^\dagger A\rho + \rho A^\dagger A), \quad (5.19)$$

$$D_1[A] = D[A \otimes I_3 \otimes I_4], \quad (5.20)$$

$$D_2[A] = D[I_3 \otimes A \otimes I_4], \quad (5.21)$$

$$D_{12}[A] = D[A \otimes I_4]. \quad (5.22)$$

Since transmons' anharmonicities are much larger than the transmon decay rate, each level's decay and dephasing are phase-independent. The system's full density matrix  $\rho(t)$  is calculated and used to extract the coherence time and correctable error rate. Table 5.2 includes all parameters used in the master equation simulation. The final simulation results for the experimental comparison using fidelity metric are shown in Fig. 5.19. For each separate case (free decay, 4 QQ echo, and AQEC), parameters are the same for all logical states  $|L_0\rangle$ ,  $|L_1\rangle$ , and  $|L_x\rangle$ .  $T_\phi^j$  is increased in the 4 QQ Echo and AQEC cases because of the echo suppression of  $1/f$  noise.

Table 5.3 shows the lifetime limitations from different error channels in the AQEC case. In the ideal implementation, we include only the single photon decay and QR couplings  $\chi_j$  in the simulation. The transmon photon excitation is enhanced when all sidebands are turned on. However, excitation error on  $|L_x\rangle$  is partially correctable under three-level approximation, and thus  $|L_x\rangle$  is more insensitive to it compared to  $|L_{0/1}\rangle$ . Resonator photon excitation happens from the heating effect when QR sidebands are on. Larger cavity photon number  $n_{\text{res}}$  will dephase all logical states and is one of the dominant error sources in our system. With higher resonator frequencies or an extra coupler between transmon and

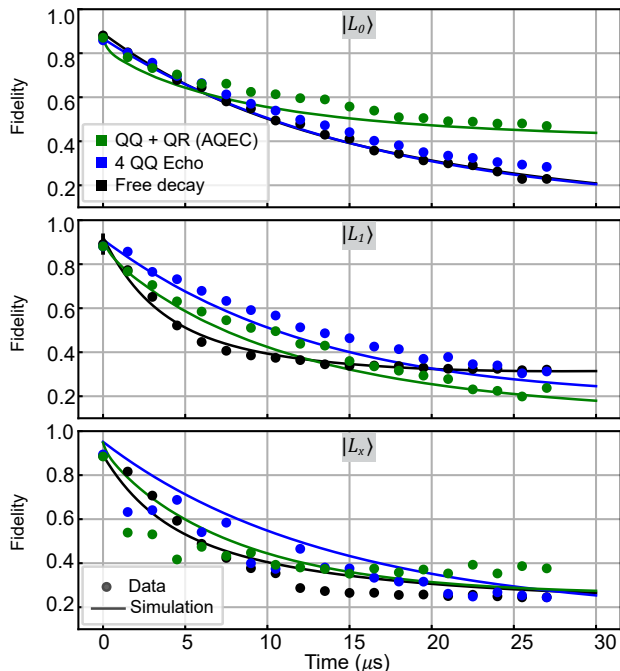


Figure 5.19: Simulation of the Star code performance in the static frame with the experimental data using fidelity metric. Error bars (one standard deviation) are smaller than the marker size.

resonator,  $n_{\text{res}}$  can be reduced under the same QR rate  $\Omega_j$ . The next two dominant error channels are cross-Kerr of between the transmons and QR frequency mismatch.  $ZZ_{ff1}$  and  $ZZ_{ff2}$  will dephase logical superposition states, as discussed in Sec. 3.4 (but has no effect on individual logical states). QR frequency mismatch is unavoidable in the presence of  $ZZ$ . In the experiment, we apply on-resonance  $|e0\rangle \leftrightarrow |f1\rangle$  drive for  $|L_0\rangle$  (corresponding the partner transmon being in  $|g\rangle$ ). Consequently, for  $|L_1\rangle$  the QR sidebands become detuned by  $ZZ_{ff1}$  and  $ZZ_{ff2}$  (corresponding to the partner being in  $|f\rangle$ ) and effectively perform slower error correction. The QQ sideband frequency mismatch comes from a modest upper bound of the system's frequency drift (around 10 kHz). This is not comparable to the  $W$  and has no significant influence on the logical states. Other dephasing noise sources include  $1/f$  noise, white noise, and  $|ff\rangle$ 's correlated dephasing. Among those three, the white noise affects AQEC performance as it has a constant noise spectrum that cannot be suppressed through the spin echo. Star code protocol is also insensitive to small sideband amplitude drifts. The

phase between logical states is defined by different sideband pairs, and amplitude drifts have to be comparable to  $W$  to change the logical states. Further, when all sidebands are on, both transmons' physical  $T_1$  are shortened, which slightly reduces the performance. Other insignificant error sources include leakage to higher transmon energy levels ( $|\alpha_j| \gg W$ ) and population in the coupler mode ( $\omega_c \gg \omega_j$ ). Those are not considered in the simulation as the transition frequency is far away.

Simulation parameters	Free decay	4 QQ echo	AQEC
$Q_1 T_1^{ge,1}(\mu s)$	18.0	21.0	21.0
$Q_1 T_1^{ef,1}(\mu s)$	33.0	29.0	23.0
$Q_1 T_\phi^1(\mu s)^\dagger$	15.0	23.0	23.0
$Q_1 T_1^\uparrow(\mu s)$	$\infty$	$\infty$	600.0
$Q_2 T_1^{ge,2}(\mu s)^*$	8.0	9.0	9.0
$Q_2 T_1^{ef,2}(\mu s)$	33.0	29.0	23.0
$Q_2 T_\phi^2(\mu s)^\dagger$	15.0	23.0	23.0
$Q_2 T_1^\uparrow(\mu s)$	$\infty$	$\infty$	600.0
$T_\phi^{ ff\rangle}(\mu s)$	4.4	80.0	80.0
$\kappa_1$ (MHz)	0.53	0.53	0.53
$\kappa_2$ (MHz)	0.48	0.48	0.48
$\chi_1$ (MHz)			-0.2
$\chi_2$ (MHz)			-0.2
$n_{\text{res}}$	0.00	0.00	0.03
$W_r$ (MHz)		1.00	1.45
$W_b$ (MHz)		1.70	1.25
$\nu_r$ (MHz)		1.50	0.80
$\nu_b$ (MHz)		0.00	-0.90
$\Omega_1$ (MHz)			0.39
$\Omega_2$ (MHz)			0.39
$ZZ_{ff1}$ (MHz)			0.6
$ZZ_{ff2}$ (MHz)			2.2

Table 5.2: Parameters used in the master equation simulation.  $\{W_{r/b}, \Omega_j, \nu_{r/b}\}$  are extracted through Fig. 5.12 in simulation;  $ZZ_{ff1}$  and  $ZZ_{ff2}$  are experimentally measured through  $|e0\rangle \leftrightarrow |f1\rangle$  on-resonance frequency difference when all sidebands on. All coherence numbers  $\{T_1, T_\phi\}$ ,  $n_{\text{res}}$ , and  $\chi_j$  are free parameters chosen in the simulation to match the experimental data. The other parameters listed are all obtained from measurements. Irrelevant parameters in each case are not shown in the table and are not included in the simulation.

$\dagger$  Dephasing in the 4 QQ echo and AQEC cases are higher because of the QQ sideband spin-echo improvement.

\*  $Q_2$ 's  $T_1^{ge}$  is lower than  $Q_1$ 's because of the TLSs around the transition frequency. Effects to the codewords performance are minimal as the population on  $|e\rangle$  is corrected.

Error channels limit	$ L_0\rangle$	$ L_1\rangle$	$ L_y\rangle^{\ddagger}$	$ L_x\rangle$
Ideal implementation*	95 $\mu$ s		95 $\mu$ s	160 $\mu$ s
Transmon photon excitation	$\sim 360$ $\mu$ s		360 $\mu$ s	$\sim 3$ ms
$n_{\text{res}}$ dephasing <sup>†</sup>	$\sim 55$ $\mu$ s		$\sim 40$ $\mu$ s	$\sim 40$ $\mu$ s
Other dephasing noise <sup>†</sup>	$\sim 50$ $\mu$ s		$\sim 35$ $\mu$ s	$\sim 35$ $\mu$ s
Transmon $ZZ$ dephasing	$\infty$		$\sim 30$ $\mu$ s	$\sim 30$ $\mu$ s
QR frequency mismatch	$> 10$ ms	$\sim 45$ $\mu$ s		
QQ frequency mismatch	$> 10$ ms		$> 10$ ms	$\sim 1.5$ ms
QQ rate mismatch	$> 10$ ms		$> 10$ ms	$\sim 4$ ms
Reduced physical $T_1$	$\sim 330$ $\mu$ s		$\sim 330$ $\mu$ s	$\sim 400$ $\mu$ s
Total predicted lifetime	$\sim 18.2$ $\mu$ s	$\sim 13.0$ $\mu$ s	$\sim 10.0$ $\mu$ s	$\sim 10.3$ $\mu$ s
Experimental lifetime	$28.1 \pm 10.0$ $\mu$ s	$16.3 \pm 2.6$ $\mu$ s		$5.2 \pm 2.0$ $\mu$ s

Table 5.3: Various decoherence channels for the logical qubit. Ideal implementation represents logical states' lifetime with QR coupling and only  $T_1$  error. Each limit is extracted using the simulation through lifetime difference after adding relevant error channels. The average photon number in the resonator ( $n_{\text{res}}$ ) increases during external drives and dephases transmons through photon shot noise. Other dephasing noise include  $1/f$  noise, white noise, correlated dephasing noise, and any other noise source. The total effect is represented with  $T_\phi^j$  in the simulation.  $ZZ$  between transmons introduces a large mismatch in QR frequency for  $|L_1\rangle$  and  $|L_x\rangle$ , and the effect is combined with  $ZZ$  dephasing for  $|L_x\rangle$  case. The drifts in sideband amplitudes frequencies are less than 5% and 20 kHz, and those limits are in the order of ms.

\* Ideal implementation includes QR couplings  $\chi_j$  but no QQ  $ZZ$  couplings.

<sup>†</sup>  $n_{\text{res}}$  and  $T_\phi^j$  are determined through simulation-experiment matching.

<sup>‡</sup>  $|L_y\rangle$ 's lifetime is estimated through simulation, based on  $|L_x\rangle$ 's experimental error channels.

## CHAPTER 6

### OUTLOOK AND CONCLUSIONS

In summary, we have theoretically proposed a hardware-efficient AQEC code, the Star code, and experimentally demonstrated all required interactions utilizing only two transmon-resonator pairs and a linear coupler to perform the second-order transitions. Three levels per transmon are used to store information, with the middle level capturing photon loss error, and entropy is dumped to the resonator autonomously through the always-on cooling sidebands. Inter-transmon parametric drives are applied to the coherence-preserving coupler for separating the Star code logical space from other eigenstates. We demonstrated a clear low-frequency dephasing suppression by turning on all QQ sidebands and a minor improvement after turning on the additional error correction drives because of the presence of residual  $ZZ$  coupling. The static  $ZZ$  is suppressed with the inductive coupler while engineering the cancellation of the dynamical  $ZZ$  arising in the presence of all sidebands remains a topic of future research (see Supplementary Note 6 for details). Our system is entirely constructed from scalable components and fundamentally avoids the need for fast and accurate error detection and feedback error correction pulses. The Star code can be a self-corrected building block for the surface code [46, 92] to further correct higher-order errors when scaled up, and can be a fault-tolerant qubit for the bosonic system.

In the future, engineering a  $ZZ$ -free coupler would remove the primary source of decoherence in this work. Error-transparent single-qubit and two-qubit gates have been proposed theoretically to extend the Star code beyond single qubits [40]. The Star code can also be implemented in other platforms with an anharmonic three-level structure.

# CHAPTER 7

## WIRINGS AND FAB RECIPE

### 7.1 Wiring Diagrams

Fig. 7.1 shows the room and cryogenic temperature measurement chain for the Star Code device. The device is mounted on the mixing chamber plate of the dilution fridge with a 15 mK base temperature. A Tektronix 5014C AWG (1.2 GSa/s) is the master trigger for all other equipment. The readout pulses are generated through two CW tones from RF sources (PSG-E8257D), and modulated by AWG 5014C. The qubit input pulses are generated through another 4-channel AWG (Keysight M8195 65 GSa/s, 16 GSa/s per channel). The qubit and readout signals are combined and sent into the dilution fridge through lines In<sub>1</sub> and In<sub>2</sub>. Three DC sources (Yokogawa GS200) are used to bias the DC flux of the coupler and two Josephson Parametric Amplifiers (JPA). The red and blue QQ RF flux drives and two direct QR charge drives are synthesized through the same 4-channel AWG. Inside the fridge, at the 4K plate, all input lines have 20-dB attenuators. At the base plate, In<sub>1</sub> and In<sub>2</sub> lines have 10-dB attenuators, followed by a strong Eccosorb<sup>®</sup> providing 20-dB attenuation at 4 GHz. Charge<sub>1</sub> and Charge<sub>2</sub> lines have 20-dB attenuators, followed by strong Eccosorb providing 20-dB attenuation at 4 GHz, and a bandpass filter with passband 3.9 – 4.8 GHz. The DC Flux line has a low pass filter (DC – 1.9 MHz) and a weak Eccosorb (1-dB attenuation at 4 GHz). The red-frequency RF flux line passes through a weak Eccosorb first, followed by a high pass filter (cut off at 200 MHz) and a low pass filter (cut off at 2 GHz). The blue-frequency RF flux line passes through a weak Eccosorb first, followed by a high pass filter (cut off at 6 GHz). The two RF flux lines and the DC flux line are combined and pass through a Step Impedance Purcell Filter (SIPF) with a stop band 2.5 – 5.5 GHz. The two output signals go through three circulators, then each amplified by a JPA with 15-dB gain, followed by a low pass filter (cut off at 8 GHz), two circulators, a DC block, and amplified

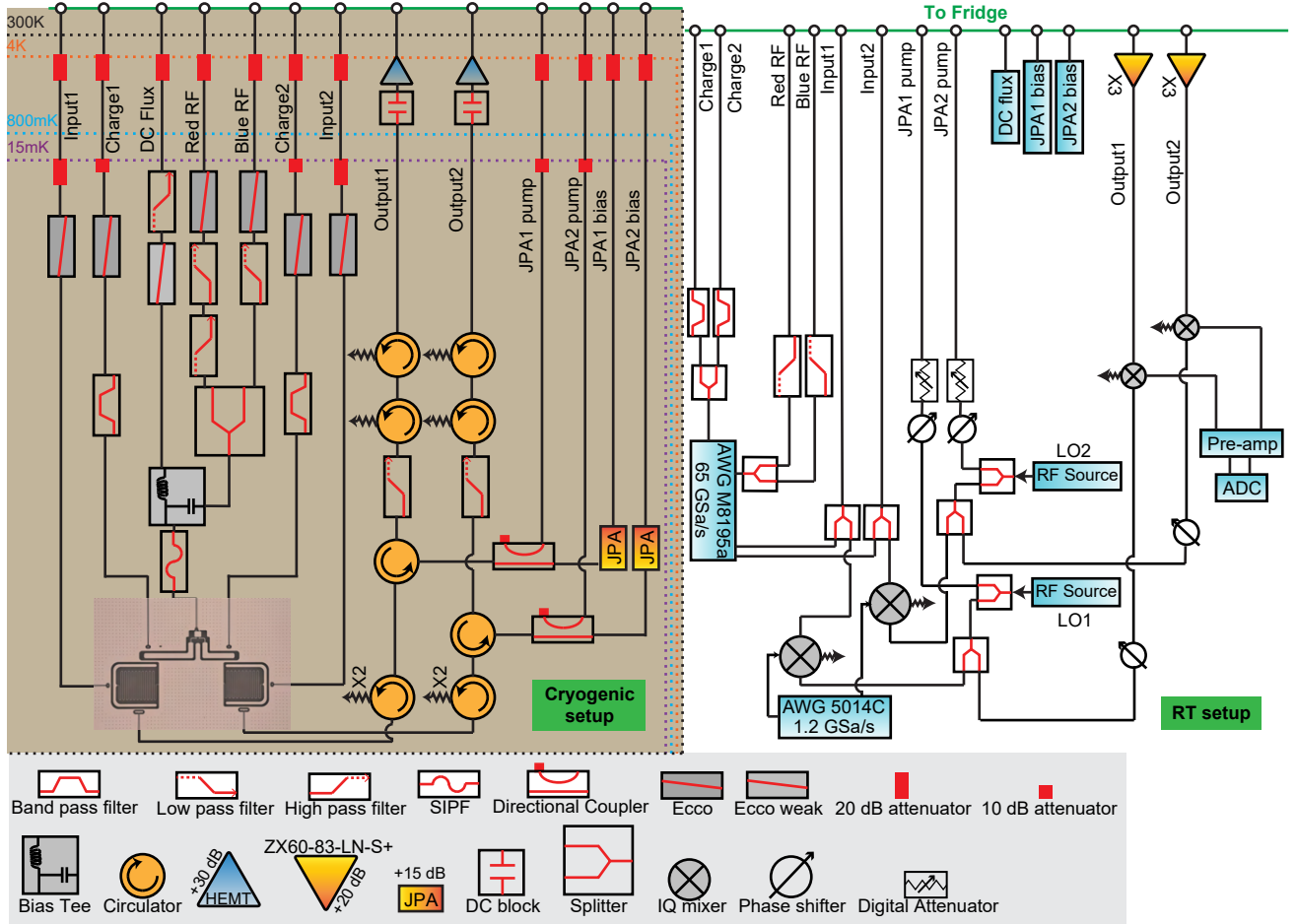


Figure 7.1: Detailed cryogenic and room temperature measurement setup.

with one LNF High-Electron-Mobility Transistor (HEMT) amplifier. The output signals are further amplified at room temperature, then demodulated, filtered with a low pass filter (DC –250 MHz), and amplified again using the SRS Preamplifier. The final signal is digitized with Alazar ATS 9870 (1 GSa/s) and analyzed in a computer.

The other projects use the same wiring diagrams.

## 7.2 Fab Recipe

1. Base layer metal deposition:

- (a) 2-inch 430  $\mu\text{m}$  thick C-plane sapphire EFG wafers from CrysTec<sup>®</sup>.

(b) Sapphire wafer annealing recipe: Starting with room temperature, ramp up to 700°C at a rate of 350°C/hr; Hold at 700°C for 15 min; Ramp up to 1000°C at a rate of 300°C/hr; Hold at 1000°C for 15 min; Ramp up to 1215°C at a rate of 100°C/hr; Hold at 1215°C for 3 hrs; Ramp down 1200°C at a rate of 100°C/hr; Hold at 1200°C for 1 hrs; Ramp up to 1215°C at a rate of 50°C/hr; Hold at 1215°C for 2 hrs; Ramp down to 30°C at a rate of 100°C/hr;

(c) TAMI cleaning the wafer: Toluene, Acetone, Methanol, and IPA sonication for 3 min per frequency. Rinse under DI water for 2 min, and spin dry.

(d) Acid cleaning the wafer: Dip in Nanostrip for 5 min, set the hot plate to 75°C ( 40°C), rinse under DI water for 2 min, dip in H<sub>2</sub>SO<sub>4</sub> for 5 min, spin dry.

(e) Load wafer into AJA ATC Orion 8 UHV Sputtering System, sputter 200 nm Tantalum at 800°C.

## 2. Base layer photolithography:

(a) TAMI clean for 5 min at different frequencies

(b) DI water rinse for 2 min, spin dry

(c) Bake at 115°C for 2 min

(d) Spin coat AZ1518 at 3000 rpm, ramp=1000 rpm/s, 45 sec

(e) Soft bake at 95°C for 1 min

(f) Heidelberg photolithography using 405 nm laser, dose= 190 mJ/cm<sup>2</sup>.

(g) Post bake at 115°C for 2 min

(h) Develop in AZ 300 MIF for 1 min, DI water quench, rinse for 2 min, spin dry

(i) Oven bake at 120°C for 10 min

(j) Put wafer in Oxygen Asher using recipe 7 for 11 min

(k) HF wet etch: use Teflon stubby, wafer feature side down; Dip in Transene Tantalum etchant 1:1:1 for 20 sec, no agitation; Transfer into 2 Teflon beaker with DI water; Rinse under DI water, transfer to glass DI water beaker' Rinse under water, spin dry.

(l) Leave wafer in 80°C Remover PG overnight

### 3. E-beam lithography

(a) Take out the wafer from Remover PG, sonicate in Acetone and IPA for 5 min at different frequencies; DI water rinse for 1 min, and spin dry.

(b) Vacuum bake without the wafer using recipe 10, vacuum bake with the wafer using recipe 4

(c) Spin coat MMA EL 11 at 4500 rpm, ramp=500 rpm/s, 45 sec, bake at 180°C for 5 min

(d) Spin coat PMMA A7 950 at 4500 rpm, ramp=500 rpm/s, 45 sec, bake at 180°C for 5 min

(e) Deposit 10nm gold at a rate of 0.5 Å/s

(f) E-beam lithography writing

(g) Gold etch for 35 sec, DI water quench, blow dry

(h) Develop in IPA:H<sub>2</sub>O solution=45:15 mL for 90 sec at 6°C

(i) Quench in pure IPA immediately, blow dry for 1 min, load into Plassys

### 4. Junction deposition

(a) Ar ion milling at 3 different angles ( $\pm 60^\circ$ ,  $0^\circ$ ), 70 sec each

(b) Ti gettering

(c) First Al layer, 45nm, 0.3nm/s, angle=23°

(d) Static Oxidation with O<sub>2</sub>-Ar mixture (15:85) for 30 min at 50 mbar.

(e) Ti gettering

(f) Second Al layer, 155nm, 0.3nm/s, angle=-23°

(g) Static Oxidation with O<sub>2</sub>-Ar mixture (15:85) for 10 min at 10 mbar (surface passivation).

(h) Purge the Plassys chamber with N<sub>2</sub>, leave for 10 mins before taking the sample out.

### 5. Dicing and liftoff

- (a) Spin coat AZ1518 at 3000 rpm, ramp=1000 rpm/s, 45 sec.
- (b) Soft bake at 95°C for 1 min.
- (c) Dice the wafer in Disco DAD 3240 dicing saw.
- (d) UV light for 90 sec, peel off the chips, leave chip in 80 C° Remover PG for 4 hr.
- (e) Acetone, IPA rinse for 5 min each, no sonication, N<sub>2</sub> blow dry.

## REFERENCES

- [1] M. H. Abobeih, Y. Wang, J. Randall, S. J. H. Loenen, C. E. Bradley, M. Markham, D. J. Twitchen, B. M. Terhal, and T. H. Taminiau. Fault-tolerant operation of a logical qubit in a diamond quantum processor. *Nature*, 606(7916):884–889, Jun 2022.
- [2] D. Aharonov and M. Ben-Or. Fault-tolerant quantum computation with constant error rate. *SIAM Journal on Computing*, 38(4):1207–1282, 2008.
- [3] P. W. Anderson and J. M. Rowell. Probable observation of the josephson superconducting tunneling effect. *Phys. Rev. Lett.*, 10:230–232, Mar 1963.
- [4] A. Aspuru-Guzik, A. D. Dutoi, P. J. Love, and M. Head-Gordon. Simulated quantum computation of molecular energies. *Science*, 309(5741):1704–1707, 2005.
- [5] R. Babbush, J. R. McClean, M. Newman, C. Gidney, S. Boixo, and H. Neven. Focus beyond quadratic speedups for error-corrected quantum advantage. *PRX Quantum*, 2:010103, Mar 2021.
- [6] E. Bernstein and U. Vazirani. Quantum complexity theory. *SIAM Journal on Computing*, 26(5):1411–1473, 1997.
- [7] R. Bianchetti, S. Filipp, M. Baur, J. M. Fink, C. Lang, L. Steffen, M. Boissonneault, A. Blais, and A. Wallraff. Control and tomography of a three level superconducting artificial atom. *Phys. Rev. Lett.*, 105:223601, Nov 2010.
- [8] L. S. Bishop. Circuit quantum electrodynamics, 2010.
- [9] A. Blais, A. L. Grimsmo, S. M. Girvin, and A. Wallraff. Circuit quantum electrodynamics. *Rev. Mod. Phys.*, 93:025005, May 2021.
- [10] D. Bluvstein, H. Levine, G. Semeghini, T. T. Wang, S. Ebadi, M. Kalinowski, A. Keesling, N. Maskara, H. Pichler, M. Greiner, V. Vuletić, and M. D. Lukin. A quantum processor based on coherent transport of entangled atom arrays. *Nature*, 604(7906):451–456, Apr 2022.
- [11] M. J. Bremner, C. M. Dawson, J. L. Dodd, A. Gilchrist, A. W. Harrow, D. Mortimer, M. A. Nielsen, and T. J. Osborne. Practical scheme for quantum computation with any two-qubit entangling gate. *Phys. Rev. Lett.*, 89:247902, Nov 2002.
- [12] T. Brown, E. Doucet, D. Ristè, G. Ribeill, K. Cicak, J. Aumentado, R. Simmonds, L. Govia, A. Kamal, and L. Ranzani. Trade off-free entanglement stabilization in a superconducting qutrit-qubit system. *Nature Communications*, 13(1):3994, Jul 2022.
- [13] S. A. Caldwell, N. Didier, C. A. Ryan, E. A. Sete, A. Hudson, P. Karalekas, R. Manenti, M. P. da Silva, R. Sinclair, E. Acala, N. Alidoust, J. Angeles, A. Bestwick, M. Block, B. Bloom, A. Bradley, C. Bui, L. Capelluto, R. Chilcott, J. Cordova, G. Crossman,

- M. Curtis, S. Deshpande, T. E. Bouayadi, D. Girshovich, S. Hong, K. Kuang, M. Lenihan, T. Manning, A. Marchenkov, J. Marshall, R. Maydra, Y. Mohan, W. O'Brien, C. Osborn, J. Otterbach, A. Papageorge, J.-P. Paquette, M. Pelstring, A. Polloreno, G. Prawiroatmodjo, V. Rawat, M. Reagor, R. Renzas, N. Rubin, D. Russell, M. Rust, D. Scarabelli, M. Scheer, M. Selvanayagam, R. Smith, A. Staley, M. Suska, N. Tezak, D. C. Thompson, T.-W. To, M. Vahidpour, N. Vodrahalli, T. Whyland, K. Yadav, W. Zeng, and C. Rigetti. Parametrically activated entangling gates using transmon qubits. *Phys. Rev. Appl.*, 10:034050, Sep 2018.
- [14] S. P. Chitta, T. Zhao, Z. Huang, I. Mondragon-Shem, and J. Koch. Computer-aided quantization and numerical analysis of superconducting circuits, 2022.
- [15] J. M. Chow, A. D. Córcoles, J. M. Gambetta, C. Rigetti, B. R. Johnson, J. A. Smolin, J. R. Rozen, G. A. Keefe, M. B. Rothwell, M. B. Ketchen, and M. Steffen. Simple all-microwave entangling gate for fixed-frequency superconducting qubits. *Phys. Rev. Lett.*, 107:080502, Aug 2011.
- [16] J. Chu, X. He, Y. Zhou, J. Yuan, L. Zhang, Q. Guo, Y. Hai, Z. Han, C.-K. Hu, W. Huang, et al. Scalable algorithm simplification using quantum and logic. *Nature Physics*, pages 1–6, 2022.
- [17] J. Chu, D. Li, X. Yang, S. Song, Z. Han, Z. Yang, Y. Dong, W. Zheng, Z. Wang, X. Yu, D. Lan, X. Tan, and Y. Yu. Realization of superadiabatic two-qubit gates using parametric modulation in superconducting circuits. *Phys. Rev. Applied*, 13:064012, Jun 2020.
- [18] J. Cramer, N. Kalb, M. A. Rol, B. Hensen, M. S. Blok, M. Markham, D. J. Twitchen, R. Hanson, and T. H. Taminiau. Repeated quantum error correction on a continuously encoded qubit by real-time feedback. *Nature Communications*, 7(1):11526, May 2016.
- [19] D. Deutsch and R. Jozsa. Rapid solution of problems by quantum computation. *Proceedings of the Royal Society of London A: Mathematical, Physical and Engineering Sciences*, 439(1907):553–558, 1992.
- [20] E. Dogan, D. Rosenstock, L. Le Guevel, H. Xiong, R. A. Mencia, A. Somoroff, K. N. Nesterov, M. G. Vavilov, V. E. Manucharyan, and C. Wang. Two-fluxonium cross-resonance gate. *Phys. Rev. Appl.*, 20:024011, Aug 2023.
- [21] B. Eastin and E. Knill. Restrictions on transversal encoded quantum gate sets. *Phys. Rev. Lett.*, 102:110502, Mar 2009.
- [22] L. Egan, D. M. Debroy, C. Noel, A. Risinger, D. Zhu, D. Biswas, M. Newman, M. Li, K. R. Brown, M. Cetina, and C. Monroe. Fault-tolerant control of an error-corrected qubit. *Nature*, 598(7880):281–286, Oct 2021.
- [23] A. Erhard, H. Poulsen Nautrup, M. Meth, L. Postler, R. Stricker, M. Stadler, V. Negnevitsky, M. Ringbauer, P. Schindler, H. J. Briegel, R. Blatt, N. Friis, and T. Monz. Entangling logical qubits with lattice surgery. *Nature*, 589(7841):220–224, Jan 2021.

- [24] P. Faist and R. Renner. Practical and reliable error bars in quantum tomography. *Phys. Rev. Lett.*, 117:010404, Jul 2016.
- [25] R. P. Feynman. Simulating physics with computers. *International Journal of Theoretical Physics*, 21(6):467–488, Jun 1982.
- [26] C. Figgatt, D. Maslov, K. A. Landsman, N. M. Linke, S. Debnath, and C. Monroe. Complete 3-qubit grover search on a programmable quantum computer. *Nature Communications*, 8(1):1918, Dec 2017.
- [27] A. G. Fowler, M. Mariantoni, J. M. Martinis, and A. N. Cleland. Surface codes: Towards practical large-scale quantum computation. *Phys. Rev. A*, 86:032324, Sep 2012.
- [28] J. C. Gallop and B. W. Petley. SQUIDS and their applications. *Journal of Physics E: Scientific Instruments*, 9(6):417–429, jun 1976.
- [29] M. Ganzhorn, G. Salis, D. J. Egger, A. Fuhrer, M. Mergenthaler, C. Müller, P. Müller, S. Paredes, M. Pechal, M. Werninghaus, and S. Filipp. Benchmarking the noise sensitivity of different parametric two-qubit gates in a single superconducting quantum computing platform. *Phys. Rev. Res.*, 2:033447, Sep 2020.
- [30] M. Ganzhorn, G. Salis, D. J. Egger, A. Fuhrer, M. Mergenthaler, C. Müller, P. Müller, S. Paredes, M. Pechal, M. Werninghaus, and S. Filipp. Benchmarking the noise sensitivity of different parametric two-qubit gates in a single superconducting quantum computing platform. *Phys. Rev. Research*, 2:033447, Sep 2020.
- [31] J. M. Gertler, B. Baker, J. Li, S. Shirol, J. Koch, and C. Wang. Protecting a bosonic qubit with autonomous quantum error correction. *Nature*, 590(7845):243–248, Feb 2021.
- [32] S. M. Girvin. 113Circuit QED: superconducting qubits coupled to microwave photons. In *Quantum Machines: Measurement and Control of Engineered Quantum Systems: Lecture Notes of the Les Houches Summer School: Volume 96, July 2011*. Oxford University Press, 06 2014.
- [33] L. K. Grover. Quantum mechanics helps in searching for a needle in a haystack. *Phys. Rev. Lett.*, 79:325–328, Jul 1997.
- [34] R. C. Jaklevic, J. Lambe, A. H. Silver, and J. E. Mercereau. Quantum interference effects in josephson tunneling. *Phys. Rev. Lett.*, 12:159–160, Feb 1964.
- [35] X. Y. Jin, K. Cicak, Z. Parrott, S. Kotler, F. Lecocq, J. Teufel, J. Aumentado, E. Kapit, and R. W. Simmonds. Versatile parametric coupling between two statically decoupled transmon qubits, 2023.
- [36] B. Josephson. Possible new effects in superconductive tunnelling. *Physics Letters*, 1(7):251–253, 1962.

- [37] E. Kapit. Hardware-efficient and fully autonomous quantum error correction in superconducting circuits. *Phys. Rev. Lett.*, 116:150501, Apr 2016.
- [38] E. Kapit. Hardware-efficient and fully autonomous quantum error correction in superconducting circuits. *Phys. Rev. Lett.*, 116:150501, Apr 2016.
- [39] E. Kapit. The upside of noise: engineered dissipation as a resource in superconducting circuits. *Quantum Science and Technology*, 2(3):033002, aug 2017.
- [40] E. Kapit. Error-transparent quantum gates for small logical qubit architectures. *Phys. Rev. Lett.*, 120:050503, Feb 2018.
- [41] E. Kapit, M. Hafezi, and S. H. Simon. Induced self-stabilization in fractional quantum hall states of light. *Phys. Rev. X*, 4:031039, Sep 2014.
- [42] J. Kelly, R. Barends, A. G. Fowler, A. Megrant, E. Jeffrey, T. C. White, D. Sank, J. Y. Mutus, B. Campbell, Y. Chen, Z. Chen, B. Chiaro, A. Dunsworth, I.-C. Hoi, C. Neill, P. J. J. O’Malley, C. Quintana, P. Roushan, A. Vainsencher, J. Wenner, A. N. Cleland, and J. M. Martinis. State preservation by repetitive error detection in a superconducting quantum circuit. *Nature*, 519(7541):66–69, Mar 2015.
- [43] A. Y. Kitaev. Quantum computations: algorithms and error correction. *Russian Mathematical Surveys*, 52(6):1191, dec 1997.
- [44] E. Knill. Fault-tolerant postselected quantum computation: Schemes, 2004.
- [45] J. Koch, T. M. Yu, J. Gambetta, A. A. Houck, D. I. Schuster, J. Majer, A. Blais, M. H. Devoret, S. M. Girvin, and R. J. Schoelkopf. Charge-insensitive qubit design derived from the cooper pair box. *Phys. Rev. A*, 76:042319, Oct 2007.
- [46] S. Krinner, N. Lacroix, A. Remm, A. Di Paolo, E. Genois, C. Leroux, C. Hellings, S. Lazar, F. Swiadek, J. Herrmann, G. J. Norris, C. K. Andersen, M. Müller, A. Blais, C. Eichler, and A. Wallraff. Realizing repeated quantum error correction in a distance-three surface code. *Nature*, 605(7911):669–674, May 2022.
- [47] Z. Li, P. Liu, P. Zhao, Z. Mi, H. Xu, X. Liang, T. Su, W. Sun, G. Xue, J.-N. Zhang, W. Liu, Y. Jin, and H. Yu. Error per single-qubit gate below  $10^{-4}$  in a superconducting qubit. *npj Quantum Information*, 9(1):111, 2023.
- [48] Z. Li, T. Roy, Y. Lu, E. Kapit, and D. I. Schuster. Autonomous stabilization with programmable stabilized state. *Nature Communications*, 15(1):6978, Aug. 2024.
- [49] Z. Li, T. Roy, D. R. Pérez, D. I. Schuster, and E. Kapit. Hardware-efficient autonomous error correction with linear couplers in superconducting circuits. *Phys. Rev. Res.*, 6:013171, Feb 2024.

- [50] Z. Li, T. Roy, D. Rodríguez Pérez, K.-H. Lee, E. Kapit, and D. I. Schuster. Autonomous error correction of a single logical qubit using two transmons. *Nature Communications*, 15(1):1681, Feb. 2024.
- [51] G. L. Long. Grover algorithm with zero theoretical failure rate. *Phys. Rev. A*, 64:022307, Jul 2001.
- [52] J. Long, T. Zhao, M. Bal, R. Zhao, G. S. Barron, H. sheng Ku, J. A. Howard, X. Wu, C. R. H. McRae, X.-H. Deng, G. J. Ribeill, M. Singh, T. A. Ohki, E. Barnes, S. E. Economou, and D. P. Pappas. A universal quantum gate set for transmon qubits with strong zz interactions, 2021.
- [53] Y. Lu. Parametric control of flux-tunable superconducting circuits, Aug 2019.
- [54] Y. Lu, S. Chakram, N. Leung, N. Earnest, R. K. Naik, Z. Huang, P. Groszkowski, E. Kapit, J. Koch, and D. I. Schuster. Universal stabilization of a parametrically coupled qubit. *Phys. Rev. Lett.*, 119:150502, Oct 2017.
- [55] Y. Lu, S. Chakram, N. Leung, N. Earnest, R. K. Naik, Z. Huang, P. Groszkowski, E. Kapit, J. Koch, and D. I. Schuster. Universal stabilization of a parametrically coupled qubit. *Phys. Rev. Lett.*, 119:150502, Oct 2017.
- [56] Y. Lu, A. Maiti, J. W. O. Garmon, S. Ganjam, Y. Zhang, J. Claes, L. Frunzio, S. M. Girvin, and R. J. Schoelkopf. High-fidelity parametric beamsplitting with a parity-protected converter. *Nature Communications*, 14(1):5767, Sept. 2023.
- [57] Y. Ma, Y. Xu, X. Mu, W. Cai, L. Hu, W. Wang, X. Pan, H. Wang, Y. P. Song, C.-L. Zou, and L. Sun. Error-transparent operations on a logical qubit protected by quantum error correction. *Nature Physics*, 16(8):827–831, Aug 2020.
- [58] E. Magesan and J. M. Gambetta. Effective hamiltonian models of the cross-resonance gate. *Phys. Rev. A*, 101:052308, May 2020.
- [59] M. Malekakhlagh, E. Magesan, and D. C. McKay. First-principles analysis of cross-resonance gate operation. *Phys. Rev. A*, 102:042605, Oct 2020.
- [60] A. Mandviwalla, K. Ohshiro, and B. Ji. Implementing grover’s algorithm on the ibm quantum computers. In *2018 IEEE International Conference on Big Data (Big Data)*, pages 2531–2537, Dec 2018.
- [61] M. H. Michael, M. Silveri, R. T. Brierley, V. V. Albert, J. Salmilehto, L. Jiang, and S. M. Girvin. New class of quantum error-correcting codes for a bosonic mode. *Phys. Rev. X*, 6:031006, Jul 2016.
- [62] B. K. Mitchell, R. K. Naik, A. Morvan, A. Hashim, J. M. Kreikebaum, B. Marinelli, W. Lavrijsen, K. Nowrouzi, D. I. Santiago, and I. Siddiqi. Hardware-efficient microwave-activated tunable coupling between superconducting qubits. *Phys. Rev. Lett.*, 127:200502, Nov 2021.

- [63] B. K. Mitchell, R. K. Naik, A. Morvan, A. Hashim, J. M. Kreikebaum, B. Marinelli, W. Lavrijsen, K. Nowrouzi, D. I. Santiago, and I. Siddiqi. Hardware-efficient microwave-activated tunable coupling between superconducting qubits. *Phys. Rev. Lett.*, 127:200502, Nov 2021.
- [64] F. Motzoi, J. M. Gambetta, P. Rebentrost, and F. K. Wilhelm. Simple pulses for elimination of leakage in weakly nonlinear qubits. *Phys. Rev. Lett.*, 103:110501, Sep 2009.
- [65] P. Mundada, G. Zhang, T. Hazard, and A. Houck. Suppression of qubit crosstalk in a tunable coupling superconducting circuit. *Phys. Rev. Appl.*, 12:054023, Nov 2019.
- [66] Z. Ni, S. Li, L. Zhang, J. Chu, J. Niu, T. Yan, X. Deng, L. Hu, J. Li, Y. Zhong, S. Liu, F. Yan, Y. Xu, and D. Yu. Scalable method for eliminating residual  $zz$  interaction between superconducting qubits. *Phys. Rev. Lett.*, 129:040502, Jul 2022.
- [67] M. A. Nielsen and I. L. Chuang. *Quantum Computation and Quantum Information*. Cambridge University Press, Cambridge, 10th anniversary edition edition, 2010.
- [68] C. Rigetti and M. Devoret. Fully microwave-tunable universal gates in superconducting qubits with linear couplings and fixed transition frequencies. *Phys. Rev. B*, 81:134507, Apr 2010.
- [69] D. Rodríguez Pérez. Quantum error mitigation and autonomous correction using dissipative engineering and coupling techniques. *ProQuest Dissertations and Theses*, page 147, 2021.
- [70] M. Roth, M. Ganzhorn, N. Moll, S. Filipp, G. Salis, and S. Schmidt. Analysis of a parametrically driven exchange-type gate and a two-photon excitation gate between superconducting qubits. *Phys. Rev. A*, 96:062323, Dec 2017.
- [71] M. Roth, M. Ganzhorn, N. Moll, S. Filipp, G. Salis, and S. Schmidt. Analysis of a parametrically driven exchange-type gate and a two-photon excitation gate between superconducting qubits. *Phys. Rev. A*, 96:062323, Dec 2017.
- [72] T. Roy, S. Hazra, S. Kundu, M. Chand, M. P. Patankar, and R. Vijay. Programmable superconducting processor with native three-qubit gates. *Phys. Rev. Applied*, 14:014072, Jul 2020.
- [73] T. Roy, L. Jiang, and D. I. Schuster. Deterministic grover search with a restricted oracle. *Phys. Rev. Research*, 4:L022013, Apr 2022.
- [74] T. Roy, Z. Li, E. Kapit, and D. Schuster. Two-qutrit quantum algorithms on a programmable superconducting processor. *Phys. Rev. Appl.*, 19:064024, Jun 2023.
- [75] T. Roy, Z. Li, E. Kapit, and D. I. Schuster. Tomography in the presence of stray inter-qubit coupling. *arXiv preprint arXiv:2103.13611*, 2021.

- [76] T. Roy, Z. Li, E. Kapit, and D. I. Schuster. Tomography in the presence of stray inter-qubit coupling, 2021.
- [77] C. Ryan-Anderson, J. G. Bohnet, K. Lee, D. Gresh, A. Hankin, J. P. Gaebler, D. Francois, A. Chernoguzov, D. Lucchetti, N. C. Brown, T. M. Gatterman, S. K. Halit, K. Gilmore, J. A. Gerber, B. Neyenhuis, D. Hayes, and R. P. Stutz. Realization of real-time fault-tolerant quantum error correction. *Phys. Rev. X*, 11:041058, Dec 2021.
- [78] P. Schindler, J. T. Barreiro, T. Monz, V. Nebendahl, D. Nigg, M. Chwalla, M. Hennrich, and R. Blatt. Experimental repetitive quantum error correction. *Science*, 332(6033):1059–1061, 2011.
- [79] D. I. Schuster. *Circuit quantum electrodynamics*. Yale University, 2007.
- [80] E. A. Sete, N. Didier, A. Q. Chen, S. Kulshreshtha, R. Manenti, and S. Poletto. Parametric-resonance entangling gates with a tunable coupler. *Phys. Rev. Applied*, 16:024050, Aug 2021.
- [81] P. W. Shor. Scheme for reducing decoherence in quantum computer memory. *Phys. Rev. A*, 52:R2493–R2496, Oct 1995.
- [82] P. W. Shor. Polynomial-time algorithms for prime factorization and discrete logarithms on a quantum computer. *SIAM Journal on Computing*, 26(5):1484–1509, 1997.
- [83] Y. Sung, L. Ding, J. Braumüller, A. Vepsäläinen, B. Kannan, M. Kjaergaard, A. Greene, G. O. Samach, C. McNally, D. Kim, A. Melville, B. M. Niedzielski, M. E. Schwartz, J. L. Yoder, T. P. Orlando, S. Gustavsson, and W. D. Oliver. Realization of high-fidelity  $cz$  and  $zz$ -free iswap gates with a tunable coupler. *Phys. Rev. X*, 11:021058, Jun 2021.
- [84] B. M. Terhal. Quantum error correction for quantum memories. *Rev. Mod. Phys.* **87**, 307, 2015.
- [85] V. Tripathi, M. Khezri, and A. N. Korotkov. Operation and intrinsic error budget of a two-qubit cross-resonance gate. *Phys. Rev. A*, 100:012301, Jul 2019.
- [86] F. Verstraete, M. M. Wolf, and J. Ignacio Cirac. Quantum computation and quantum-state engineering driven by dissipation. *Nature Physics*, 5(9):633–636, Sep 2009.
- [87] G. Waldherr, Y. Wang, S. Zaiser, M. Jamali, T. Schulte-Herbrüggen, H. Abe, T. Ohshima, J. Isoya, J. F. Du, P. Neumann, and J. Wrachtrup. Quantum error correction in a solid-state hybrid spin register. *Nature*, 506(7487):204–207, Feb 2014.
- [88] A. Wallraff, D. I. Schuster, A. Blais, J. M. Gambetta, J. Schreier, L. Frunzio, M. H. Devoret, S. M. Girvin, and R. J. Schoelkopf. Sideband transitions and two-tone spectroscopy of a superconducting qubit strongly coupled to an on-chip cavity. *Phys. Rev. Lett.*, 99:050501, Jul 2007.

- [89] Y. Wang, Z. Hu, B. C. Sanders, and S. Kais. Qudits and high-dimensional quantum computing. *Frontiers in Physics*, 8:589504, 2020.
- [90] F. Yan, P. Krantz, Y. Sung, M. Kjaergaard, D. L. Campbell, T. P. Orlando, S. Gustavsson, and W. D. Oliver. Tunable coupling scheme for implementing high-fidelity two-qubit gates. *Phys. Rev. Appl.*, 10:054062, Nov 2018.
- [91] K. Zhang, P. Rao, K. Yu, H. Lim, and V. Korepin. Implementation of efficient quantum search algorithms on nisq computers. *Quantum Information Processing*, 20(7):1–27, 2021.
- [92] Y. Zhao, Y. Ye, H.-L. Huang, Y. Zhang, D. Wu, H. Guan, Q. Zhu, Z. Wei, T. He, S. Cao, F. Chen, T.-H. Chung, H. Deng, D. Fan, M. Gong, C. Guo, S. Guo, L. Han, N. Li, S. Li, Y. Li, F. Liang, J. Lin, H. Qian, H. Rong, H. Su, L. Sun, S. Wang, Y. Wu, Y. Xu, C. Ying, J. Yu, C. Zha, K. Zhang, Y.-H. Huo, C.-Y. Lu, C.-Z. Peng, X. Zhu, and J.-W. Pan. Realization of an error-correcting surface code with superconducting qubits. *Phys. Rev. Lett.*, 129:030501, Jul 2022.